Numerical Study of High-Speed Transition due to Passive and Active Trips

A DISSERTATION
SUBMITTED TO THE FACULTY OF THE GRADUATE SCHOOL
OF THE UNIVERSITY OF MINNESOTA
BY

Prakash Shrestha

IN PARTIAL FULFILLMENT OF THE REQUIREMENTS
FOR THE DEGREE OF
DOCTOR OF PHILOSOPHY

Graham V. Candler

April, 2019

Acknowledgements

Many people have earned my gratitude for their contribution to my time in graduate school. First, I am grateful for having had an opportunity to work with my doctoral adviser, Graham Candler, who has been a tremendous mentor for me. I want to thank him for his constant support and motivation which played an instrumental role in keeping this study pleasurable and exciting. His comprehensive understanding and interests to discuss research updates always led to fruitful and motivating interactions. His suggestions for my personal and professional growth have been immense and invaluable.

I am also thankful to Dr. Scott Berry and Dr. Meelan Choudhari who were my great supervisors for the initiation of the second part of the current dissertation at NASA Langley Research Center and National Institute of Aerospace.

I would also like to show my gratitude towards Prof. Joseph Nichols, Prof. Ellen Longmire and Prof. Sean Garrick for serving as my committee members even at their busy schedules. My sincere thankfulness also goes to Dr. Mihailo Jovanović for his suggestions during the initial stage of the project.

I am grateful to Dr. Pramod Subbareddy for mentoring me during my early days in the group and setting up a few cases to get acquainted with US3D, an in-house Navier-Stokes solver. Similarly, I would like to thank Dr. Jeffery Komives and Dr. Ross Chaudhry for more in-depth guidance on the solver.

I am also indebted to numerous colleagues (former and current) in Prof. Candler's Group for their feedback and suggestions such as Dr. Derek Dinzl, Dr. Aaron Neville, Dr. Joseph Brock, Dr. Ioannis Nompelis, Dr. Heath Johnson, Dr. Erik Torres, Mr. John Reinert, Mr. John Thome, Mr. Anthony Knudsen, Mr. Tyler Hilderson, Ms. Olivia Schroeder, Mr. Charles Hollender, Mr. Honest Mrema, Ms. Durgesh Chandel, and Ms. Chiara Amato. Practice talks for AIAA and APS conferences have always been knowledgeable and

insightful with the group.

I would like to thank other colleagues from the AEM department such as Dr. Nathaniel Hildebrand and Mr. Ariel Pino, who have been great friends throughout graduate school.

I am much indebted to my parents Mr. Ashok Kumar Shrestha and Mrs. Uttara Shrestha for their constant motivation and support during my entire doctoral education. I am also grateful to my wife Regina Maharjan, sister Preeti Shrestha, and brothers-in-law Arbin Shrestha and Rajan Maharjan for being a part of this fantastic journey.

Lastly, I would like to thank Dr. Rodney Bowersox and Dr. Michael Semper for providing experimental data used in the current work. I acknowledge financial support from the Office of Naval Research through grant number N00014-15-1-2522 and NASA Hypersonic Technology (HT) Project for the support of this research.

Dedication

To my family.

Abstract

Transitional hypersonic boundary layers due to passive and active trips on a flat plate are studied using direct numerical simulations (DNS). In the case of passive trips (diamond-shaped and cylindrical), three dynamically prominent flow structures are consistently observed in both their isolated and distributed configurations. These flow structures are the upstream vortex system, the shock system, and the shear layers and the counter-rotating streamwise vortices from the wake of the trips. Analysis of the power spectral density (PSD) reveals the dominant source of instability due to the diamond-shaped trips as a coupled system of the shear layers and the counter-rotating streamwise vortices irrespective of spanwise trip-spacing. However, the dominant source of instability due to an array of cylindrical trips (Williams et al. 2018) is observed to be the upstream vortex system similar to Subbareddy et al. 2014 who used an isolated cylindrical trip. Therefore, the shape of a roughness element plays an essential role in the instability mechanism. Furthermore, dynamic mode decomposition (DMD) of three-dimensional snapshots of pressure fluctuations unveil globally dominant modes consistent with the PSD analysis in all the trip configurations. Higher peak-amplitude frequencies and amplitudes characterize dominant instabilities in higher freestream Reynolds number flows. When the trip heights are reduced, the source of instability has been observed to be unchanged, while peak-amplitude frequencies, the mean upstream recirculation zone, the mean instability-onset location, and the maximum turbulent kinetic energy is found to be reduced. When the trip spacing is greater than three times the trip width, each trip of the trip array becomes isolated.

In the case of active trips, a two-dimensional (2-D) sonic jet from a straight slot is injected into Mach-10 three-dimensional (3-D) laminar boundary layers (Berry et al. 2004). The dynamically dominant flow structures observed in the vicinity of the jet correspond to upstream and downstream separation bubbles, where the number and the size of these bubbles vary with the injector pressure. A higher injector pressure leads to the formation of larger bubbles that cause the flow to become more unstable, resulting in a sequence of three successive bifurcations: (1) steady 2-D bubble formation, (2) transition from 2-D steady to 3-D quasi-unsteady bubble, and (3) transition from 3-D quasi-unsteady to 3-D unsteady bubble. This finding indicates that specific injector pressures are required to control the

onset of transition in the laminar boundary layers. Streamwise streaks with a dominant spanwise wavelength are observed in both 3-D quasi-steady and 3-D unsteady flows. DMD of spanwise velocity reveals that the streamwise streaks originate from the upstream bubbles. In particular, the streaks arise from the coupled undulation of a primary upstream bubble and the upstream secondary bubble, which causes the flow to bifurcate from 2-D steady to 3-D quasi-unsteady. It is proposed that the source of the unsteadiness observed is generated by high-pressure fluctuations present between the secondary bubble and the jet. The unsteady interaction between the secondary bubble and the jet selects a specific wavelength of the spanwise undulation of the secondary bubble, which then modulates the primary bubble across span with the same wavelength. These two bubbles emanate two flow structures that have opposite spanwise velocities. These flow structures then travel to the top of the downstream bubbles to form a streamwise streak. The spanwise wavelength of the dominant DMD mode agrees with that of the streaks observed in the DNS. The simulation data in all cases agree well with their corresponding experiment. No effect of real gas has been found in this current study. The source of instability is observed to be independent of the thermal nature of the wall (isothermal or adiabatic). The angle of injection is observed to play a significant role in flow unsteadiness downstream of the jet. The mean Mach-disk height and the mean upstream recirculation length are compared to existing models in order to access their accuracy under the present flow and jet configurations.

Contents

List of Tables

List of Figures

Chapter 1

Introduction

Hypersonic vehicles such as space shuttles and scramjets are specifically designed for high altitudes, where Mach number is high, and Reynolds number is low due to thin atmosphere. Such low-Reynolds number flows, associated with large areas of laminar boundary layers, are desirable for low-drag flights. However, these flows lead to inefficient mixing of fuel and air in the combustor (engine) of high-speed vehicles. Since the natural transition is highly unlikely under this flow regime before the combustion chamber, tripping elements are set-up at the optimal distance from the leading edge. These tripping elements lead to a laminar hypersonic boundary layer to transition to turbulence that greatly enhances mixing with fuel downstream. Therefore, controlling and prediction of this effect of the low-Reynolds number flow using the tripping elements require high attention from the designers for reliable, efficient, and safe flights. Based on the capability to control the transition onset, there are active and passive tripping elements.

1.1 Passive tripping

First, we review the technical history of passive tripping in this section. Passive trips are the tripping elements whose geometric configurations such as trip height cannot be altered. An example of passive trips is an array of diamond-shaped trips used on a Hyper-X forebody model (Berry et al. 2004). The array is shown in Figure1.1, and the streak formation downstream leads to the transition to turbulence process before the combustor.

On the other hand, roughness elements such as protruding gap-fillers present on the

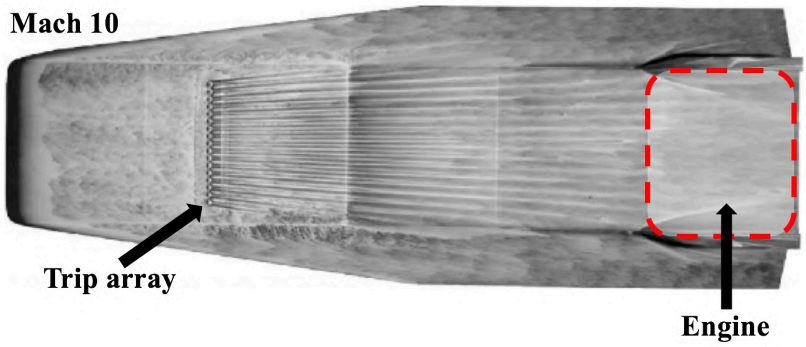

Figure 1.1: Oil-flow image showing streaks of a Mach-10 transitional hypersonic boundary layer due to a spanwise array of diamond-shaped trips ahead of the engine (combustor). Adopted from Berry et al. (2001).

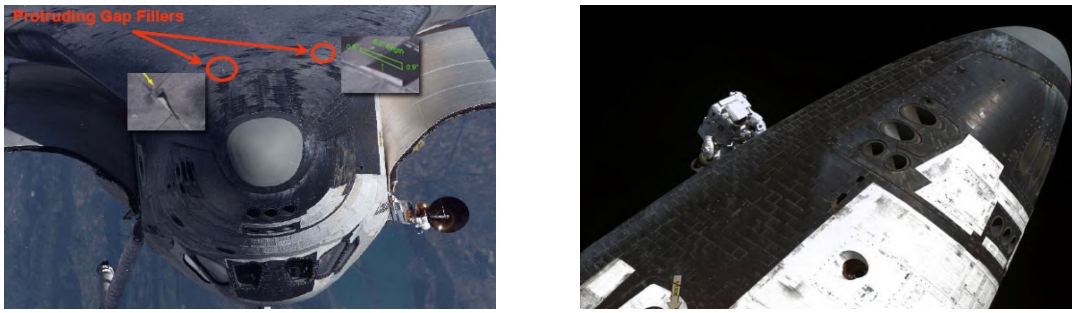

(a) (b)

Figure 1.2: (a) Protruding gap-fillers on the thermal protection system of the space shuttle and (b) an astronaut removing the protruding gap-fillers during a space walk. NASA.gov

thermal protection system (TPS) of a space shuttle are detrimental (see Figure 1.2). Skin friction and heat flux can rise by order of magnitude if a hypersonic boundary layer becomes turbulent. Compared to the increment in skin-friction coefficients, heat flux can be highly detrimental to the safety of the high-speed vehicle. Generally, the TPS system of such vehicles is thickened by an optimal addition of layers of high-heat resistive materials. Therefore, prediction and resistance of this optimally designed TPS system require a detailed understanding of the physical mechanism by which these surface irregularities trip the boundary layers.

Generally, roughness elements can be distributed such as an unpolished surface similar to sandpaper, or a single trip, such as a bolt used for providing mechanical or structural

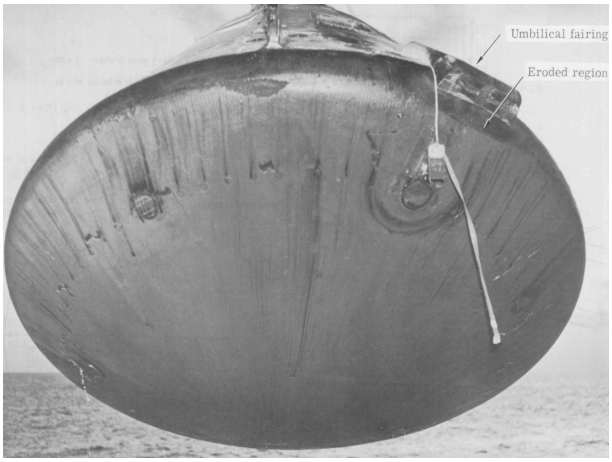

Figure 1.3: Apollo heat shield immediately after qualification flight test in Feb. 1966. Hunt and Jones (1968).

supports to flow-exposed components of a high-speed vehicle. These roughness elements perturb the mean flow of the incoming laminar boundary layer. This perturbation can decay (weak) or amplify (strong) downstream of the elements. If it significantly amplifies, flow breaks down from laminar to turbulent boundary layers. Therefore, the flow system becomes unstable and becomes turbulent. An example of structural damages due to isolated roughness elements on the Apollo heat shield is shown in Figure 1.3.

Furthermore, different shapes of roughness elements can lead to different transition mechanisms. For example, flow behaviors around isolated cylinder, triangular and pinhead roughness elements are different as shown by Figure 1.4.

To delve deeper to understand the process of boundary layer transition, and eventually be able to predict accurately and reliably whether a given hypersonic boundary layer will remain laminar or become turbulent, both experiments and numerical simulations should be simultaneously campaigned.

There is no universal mechanism-based theory to determine the exact conditions under which roughness can lead to transition. Based on Schneider (2007), there are fundamentally at least three different modes of roughness-induced transition.

1. A coupled system of a wake with streamwise vorticity and a possibly unstable shear layer generated by roughness may cause transition to turbulence. This transition can occur either just behind roughness or far downstream. The instabilities in the wake of the roughness may

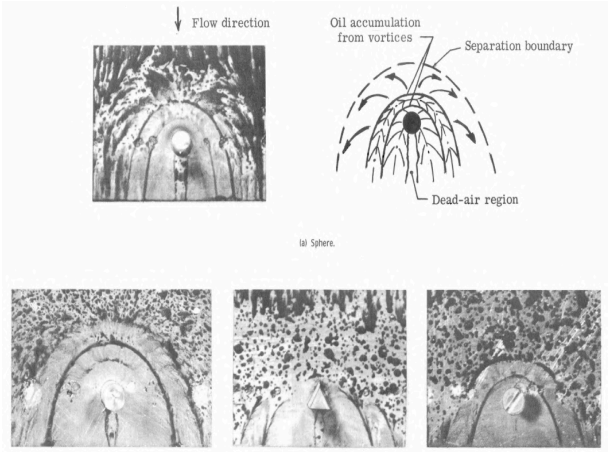

Figure 1.4: Flow dynamics around isolated roughness elements. Whitehead(1969).

depend on the nature of roughness and the related flowfield (2D or 3D, shape, height, Mach number, freestream Reynolds number, freestream disturbance, etc.). It is to be noted that a high Mach number shear layer is less unstable, and therefore, high Mach number flows are insensitive to roughness. Mostly, tall roughness elements are dominant in triggering transition. Also, the roughness elements start to interact with one another unless they are brought too close to each other.

2. Roughness elements with small height can emanate instabilities in the form of stationary crossflow (Radeztsky et al. 1999), Gortler (Luca et al. 1995), or transient growth (Reshotko and Tumin 2004). These instabilities can then lead to transition. Under these situations, the spanwise configuration of the roughness elements is critically essential, along with their height and streamwise location.

3. Acoustic waves or other freestream disturbances or perturbations can interact roughness to generate instabilities via a receptivity process (Liepmann 1943, King and Breuer 2001, and Wlezien 1994). Distribution of roughness elements along spanwise and streamwise also plays an essential role in the cases.

Let us now discuss past research on different instability mechanisms due to specific trip and flow configurations. Acarlar and Smith (1987) and Klebanoff, Cleveland and Tidstrom (1992) studied hairpin vortices in a laminar boundary layer induced by a hemispherical roughness element. They suggested that these vortices, dominant in the transition mechanism, originate in the wake of the roughness element. Danehy et al. (2010) studied the

size, shape, and speed of flow structures in transitional hypersonic boundary-layer flows due to a cylindrical roughness element. Choudhari et al. (2010) suggested that a possible absolute instability in the upstream separation region was closely related to downstream unsteadiness. Using cylindrical roughness elements, they observed steady flow with k/δ (k is the roughness height, and δ is the untripped boundary-layer thickness at the trip location) less than 1 and unsteadiness with k/δ equal to 1.3 and 2.5. Redford, Sandham & Roberts (2010) studied the flow past a smoothly shaped roughness element at Mach 3 and 6 with freestream acoustic forcing to ensure transition. They proposed a correlation for predicting transition induced by a three-dimensional roughness element at high speeds for roughness heights smaller than the boundary-layer thickness. Similarly, Tullio et al. (2013) studied a laminar-turbulent transition process induced by an isolated rectangular roughness element in a supersonic boundary layer at Mach 2.5 using direct numerical simulations (DNS). Their results indicate that the roughness element ($k/\delta = 1$) generates an unstable wake surrounded by a three-dimensional high-shear region. This wake can sustain rapid growth of instability modes. Unstable modes are related to the three-dimensional shear layer (varicose mode) or lateral shear layer (sinuous mode). The most unstable wake is observed to be the varicose type and grows much faster than the sinuous and boundary layer modes. Iyer and Mahesh (2013) performed DNS to study laminar to turbulent transition induced by a hemispherical roughness element (Danehy et al. 2009). They found that roughness height and freestream Mach number have a strong influence on transition.

Subbareddy, Bartkowicz, and Candler (2014) conducted DNS of an isolated cylindrical trip at Mach 6. We compare their findings with our data later in this paper, and therefore, their work is discussed in detail. DNS is carried out at three different Reynolds numbers (Re). We focus mainly on the high Reynolds number case in which transition to turbulence occurs just downstream of the trip. To understand the transition mechanism in the high Reynolds number case, the authors used dynamic mode decomposition (DMD) to identify dominant modes using snapshots of pressure as shown by Figures 1.5(a) and 1.5(b). For detailed information on DMD, readers are referred to Schmid (2010) and Rowley et al. (2009). Three dominant DMD modes were studied. The first two modes (harmonic and subharmonic) were related to the horseshoe vortices, indicating that the dominant transition mechanism is due to the upstream vortex system. The third mode appeared to be associated with the shear layers, emanating from the top and sides of the trip, as the second dominant mode of transition. A considerable stand-off distance between the bow shock formed ahead of the

trip, and its stagnation region leads to the formation of highly unsteady upstream vortices in the high Re case. The upstream vortices then oscillate the bow shock via compression waves, producing periodic disturbances and causing breakdown. The oscillation of the bow shock is also influenced by pressure perturbations traveling upstream from the wake. Therefore, the unsteady shock-system ahead of the trip is present in all three dominant modes. Recently, Duan & Xiao (2017) studied effects of roughness shape of isolated trips (cylinder, diamond, ramp at $k/\delta = 1$) on the transition mechanism of a Mach 6 transitional boundary layer using DNS. They found that a three-dimensional shear layer instability leads to transition in all cases except in the cylindrical case where the horseshoe vortices are more dominant. The latter conclusion is consistent with Subbareddy et al. (2014).

While discrete trips support multiple instabilities, an array of trips complicates the dynamics further by providing additional pathways due to inter-trip couplings. Whitehead (1969) studied flowfield and drag characteristics of several trip shapes under laminar boundary layer conditions at a free-stream Mach number of 6.8. Relevant to the current study, he presented the effects of trip spacing as shown in Figure 1.6. The edge Mach number was 5.5, and $k/\delta = 2$ ($k = 0.238$ cm). An array of spherical trips was mounted near the trailing edge of a 7.7-degree wedge. He observed that the trips appeared to act independently of the trip spacing, when s/D (s is the center-to-center trip spacing, and D is the spanwise trip width), was greater than 2. However, transition was delayed if the ratio of s/D was equal to 2. Smaller s/D spacings also led delayed transition, and therefore, were less effective. A possible reason could be that this trip array acts more as a barrier than like individual vortex generators (Schneider 2008a). However, the source of instability in any of these trip arrays was not discussed. Muppidi and Mahesh (2012) studied the transition mechanism of a Mach 2.9 supersonic flat plate boundary layer due to distributed surface roughness. They observed that the interaction between a strong shear layer, generated over the roughness elements, and the counter-rotating pairs of streamwise vortices, formed underneath the shear layer, causes the shear layer to break down. Ergin and White (2006) studied flow fields around an array of cylindrical roughness elements near the critical Reynolds number under a subsonic flow configuration. They observed that the locations of the maximum fluctuation intensity coincide with inflectional points in steady streamwise velocity profiles and suggest that a Kelvin-Helmholtz type instability leads to transition.

Recently, Semper & Bowersox (2017) extended the experiments, Berry et al. (2001), to

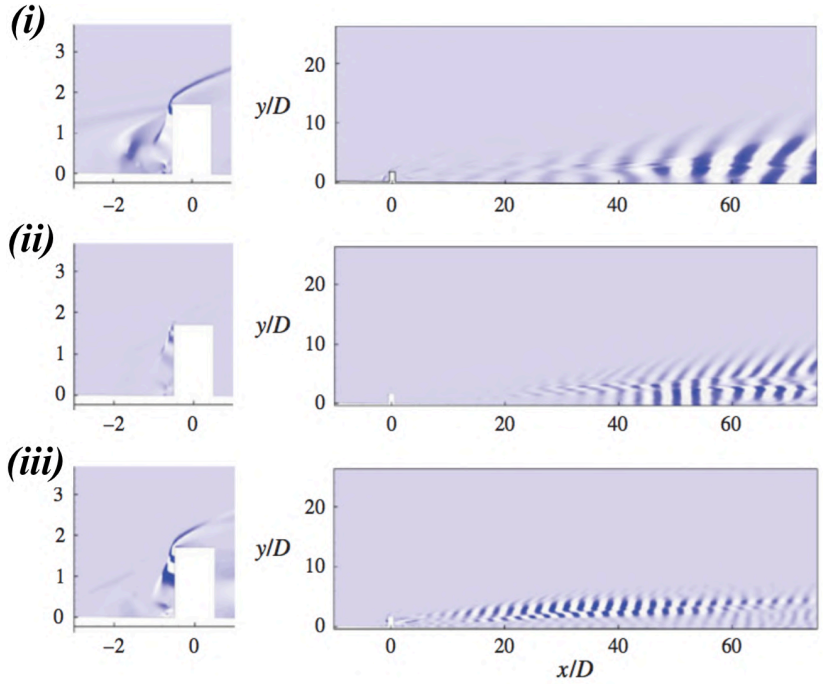

(a)

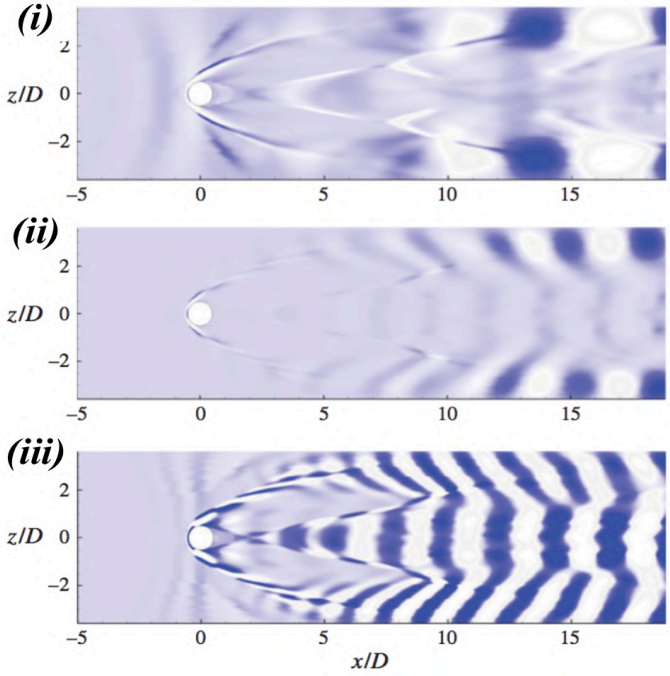

(b)

Figure 1.5: (a) Side and (b) top views of the three dominant DMD modes on a symmetry plane and a wall-parallel plane, respectively. Mode shapes represent pressure perturbations at three different temporal frequencies. Adopted from Subbareddy et al. (2014).

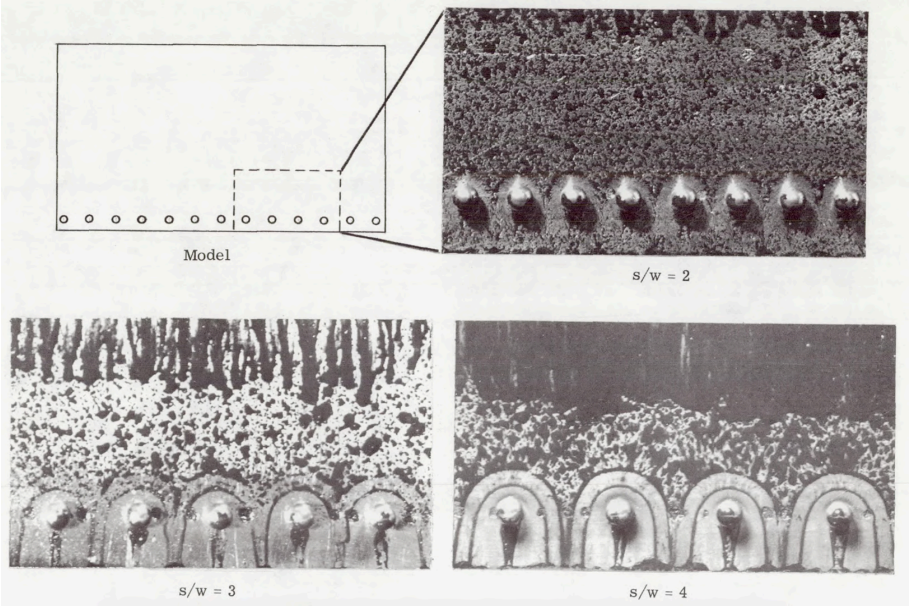

Figure 1.6: Effect of spacing on surface-flow patterns around spherical elements at $M = 5.5$, $k/\delta = 2$, and $k = 0.238$ cm. Whitehead (1969).

quantify flow structures in a Mach 5.65 low-Reynolds-number (Re_θ= 3600 based on momentum thickness θ) boundary layer with a spanwise array of three-dimensional diamond-shaped trips with $s/D = 2$ (blockage ratio = 50%) and $k/\delta = 1.48$. They observed that a Kelvin-Helmholtz type instability could be a source of flow breakdown downstream. Following this experimental campaign, Shrestha & Candler (2016) and Shrestha et al. (2017) performed DNS of the experiments to study instability mechanisms for this case. They obtained dominant frequencies that were associated with flow breakdown using power spectral density (PSD) and DMD. However, the instability mechanisms along with the effects of trip spacing and trip shape on these mechanisms were not clearly identified. Therefore, as the first part of the current dissertation, the main objective is to understand differences of the instability mechanisms between (a) the isolated cylindrical trip (Subbareddy et al. 2014) and the isolated diamond-shaped trip, and (b) the isolated diamond-shaped trip and an array of diamond-shaped trips using DNS, DMD, and PSD. Next, we study the technical background of active trips.

1.2 Active tripping

An example of an active trip is a sonic jet that is injected into a three-dimensional laminar boundary layer through a small orifice in the wall. In comparison to passive tripping, active trips have been less studied regarding the instability mechanisms. Such an active tripping method has the advantage of being able to manipulate the incoming boundary layers according to the environment such as keeping the tripping system switched on only if required. However, there is a weight penalty associated with the additional system requirements such as the gas reservoir and its manifold.

The jet injection is attributed with jet-in-supersonic-crossflow (JISC) configuration. This configuration is characterized by an expansion of the barrel shock which ends with a Mach disk. A bow shock is formed in the supersonic freestream, and a separation zone, that is present ahead of the jet, generates horseshoe vortices (HSV). A pair of counter-rotaing vortex pair (CVP) is formed downstream of the jet. A schematic of the JISC configuration is shown in Figure 1.7.

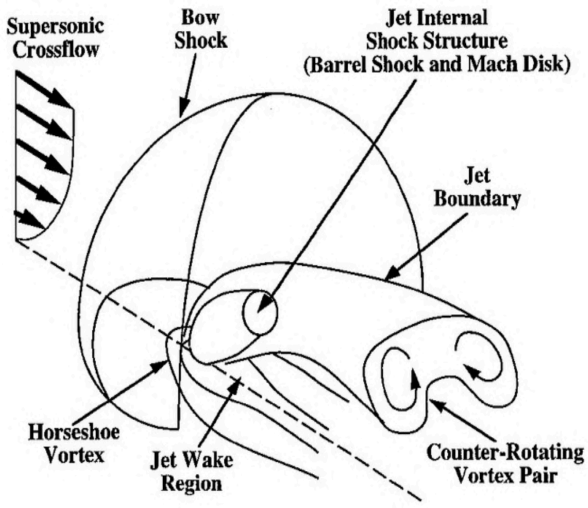

Figure 1.7: Schematic of a three-dimensional isolated circular sonic jet. Vanlerberghe et al. (2000).

Different numerical and experimental campaigns have been carried out in JISC configurations. One of the earliest experiments on promoting transition due to discrete sonic jets

was conducted by Stone and Cary (1972) at Mach 6 and 8.5. They found that the tripping capability of active blowing is similar to that by passive spheres. Recently, a detailed investigation of the instability mechanism due to a three-dimensional (3-D) isolated jet is carried out by Andre et al. (2017) using implicit large-eddy simulation (ILES), Fourier analysis, and DMD on an academic Mach 4.2 flat-plate configuration. Depending upon the injection pressure, the source of instability is observed to be different. For low PR cases, the dominant source of instability is the upstream vortex system, while for high PR cases, the source is a coupled system of shear layers from the sides of the jet and a counter-rotating vortex pair from its wake. Similarly, Génin and Menon (2010) studied interactions between a sonic air jet and a supersonic air crossflow using large eddy simulations (LES). They found that similar vortical structures in the vicinity of subsonic and supersonic jets. However, the dominant source of instability was observed to change based on the jet to free-stream momentum ratios. A lower-momentum ratio case has the CVP to be the dominant source of instability, while the horseshoe vortices have been observed to be dominant in the case of a higher-momentum ratio. Similarly, Everett and Morris (1998) studied the flowfield related to interactions of a sonic jet injected transversely into a supersonic stream. They observed that, in the region between a bow shock, that is formed ahead of the jet, and the leading edge of the injector port, the static pressure on the surface was dependent upon the jet-to-crossflow momentum flux ratio. However, no such trend was found in the other portions (sides and back) of the jet periphery.

Similarly, Brieschenk et al. 2012 compared their computational simulation and experimental data of an interaction between a sonic H_2 jet (an isolated 3-D circular jet) and hypersonic laminar boundary layers. The computational simulation was carried out using a Reynolds-Averaged Navier-Stokes (RANS) equation, while the experiment was conducted using planar laser-induced fluorescence (PLIF) technique. Their main finding was higher-fidelity simulations such as LES or direct numerical simulations (DNS) were required to more accurately capture unsteady flow structures upstream and downstream of the jet. Chai et al. 2015 studied an underexpanded sonic jet injected into a supersonic crossflow, and an overexpanded supersonic jet injected into a subsonic crossflow using LES and dynamic mode decomposition (DMD). Their DMD results indicate that the dominant mode is present between the upstream barrel shock and the bow shock for the sonic jet, while the roll-up of the upstream shear layer is dominant for the supersonic jet.

Berry et al. (2004) also examined active methods for tripping a Mach-10 hypersonic

boundary layer using a Hyper-X forebody model. All the blowing concepts tested, which included various rows of sonic orifices (holes), two- and three-dimensional slots, and random porosity. Their results indicate that the jet penetration height for blowing was roughly half the height required with passive trips for an equivalent amount of the movement of transition-onset locations. Figure 1.8 shows that higher injector pressures lead to earlier transition-onsets based on phosphor images in the setup consisting of an array of 3-D circular jet injectors. As the second part of the dissertation and similar to its first part, the primary objective is to understand instabilities generated by the two-dimensional sonic jet investigated by Berry et al. (2004) using DNS, DMD, and PSD.

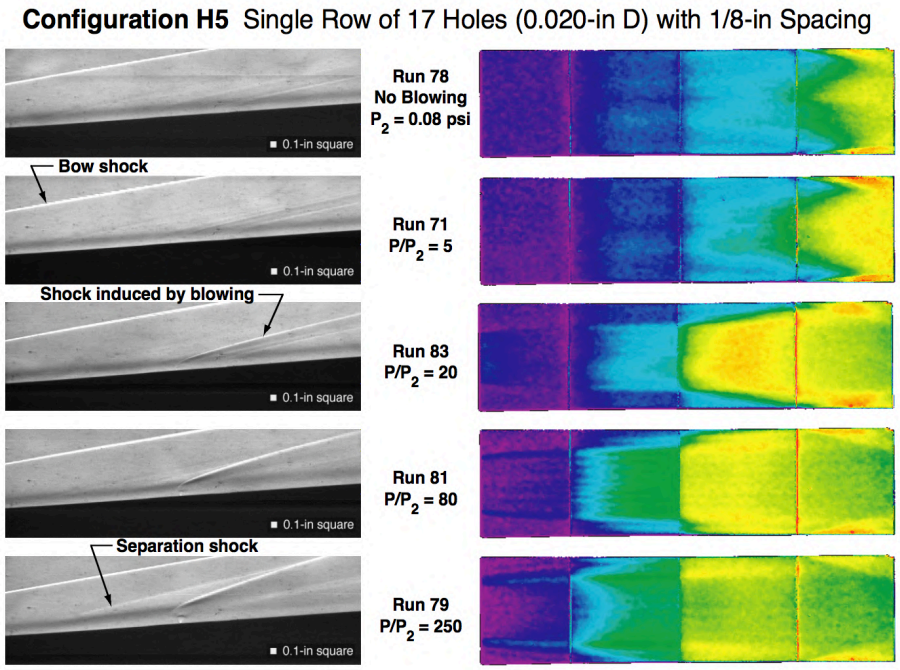

Figure 1.8: Comparison of active trip results from the Mach 10 tunnel. Berry et al. (2004). P is the stagnation pressure of the sonic jet and P_2 is the edge pressure at the jet location.

- Chapter 2 presents the basic equations and numerical methods.
- Chapter 3 describes instabilities generated by the isolated and distributed diamond-shaped trip configurations. The experiments were carried out at Actively Controlled Expansion (ACE) facility at Texas A & M University.

- Chapter 4 presents parametric studies carried out in the isolated diamond-shaped trip and the array of diamond-shaped trips.
- Chapter 5 discusses instabilities generated by the two-dimensional sonic jet. The experiments were carried out at a 31-Inch-Mach-10 wind tunnel, NASA Langley Research Center (LaRC).
- Chapter 6 investigates parameters affecting the instabilities generated by the sonic jet.
- Chapter 7 briefly discusses the overall conclusion of all the aforementioned chapters.

Chapter 2

The Governing Equations and the Numerical Methods

2.1 The Governing Equations

This section introduces the governing equations of fluid dynamics used in the present study.

2.1.1 The Conservation Equations

In the current study, the air considered for simulation is a continuum that obeys the conservation laws of mass, momentum, and energy.

For the present study, assumptions are made to simplify the form of the conservation equations. First of all, we assume that the fluid (air) acts as an ideal gas, which means that molecules are non-reacting point particles. The next assumption is that the fluid is calorically perfect. This assumption implies that the fluid considered has a constant specific heat because all the internal energy of the molecules stays in the kinetic and rotational modes. Technically, these assumptions are valid when the fluid temperature is lower than 1200 K. The final assumption is that body forces are negligible.

The conservation equations for a perfect gas are

$$\frac{\partial U}{\partial t} + \frac{\partial F_j}{\partial x_j} = \frac{\partial {F_j}^{\mathrm{v}}}{\partial x_j}, \tag{2.1}$$

where the vector of conserved variables U is

$$U = \begin{bmatrix} \rho \\ \rho u_i \\ E \end{bmatrix}, (i = 1, 2, 3). \tag{2.2}$$

The convective F_j and viscous ${F_j}^{\mathrm{v}}$ fluxes are

$$F_j = \begin{bmatrix} \rho u_j \\ \rho u_i u_j + p\delta_{ij} \\ (E + p)u_j \end{bmatrix} \text{and} \tag{2.3}$$

$${F_j}^{\mathrm{v}} = \begin{bmatrix} 0 \\ \sigma_{ij} \\ \sigma_{ij} u_i - q_j \end{bmatrix}, (i, j = 1, 2, 3). \tag{2.4}$$

The set of Equations 2.2—2.4 is referred to as the Navier-Stokes equations. In these equations, ρ is the fluid density, u_i is the i^{th} component of bulk velocity, p is the pressure, and $E = \rho c_v T + \frac{1}{2}\rho u_i u_i$ is the total energy per unit volume. T is the temperature and c_v is the specific heat capacity at constant volume.

2.1.2 Constitutive Relations

The Navier-Stokes equations are solved simultaneously with an equation of state, which in the present study is the ideal gas law.

$$p = \rho R T \tag{2.5}$$

where R is the specific gas constant. For an example, $R = 287.058$ J/Kg-K. For a Newtonian fluid, the shear stress is defined as

$$\sigma_{ij} = \mu\Big(\frac{\partial u_i}{\partial x_j} + \frac{\partial u_j}{\partial x_i}\Big) + \lambda \frac{\partial u_k}{\partial x_k} \tag{2.6}$$

where μ is the dynamic viscosity and λ is the second viscosity, typically given a value of -2/3μ. The heat flux vector q_j is defined using Fourier's law of heat conduction,

$$q_j = -k\frac{\partial T}{\partial x_j} \tag{2.7}$$

where k is the thermal conductivity of the fluid. k can be related to the viscosity by the Prandtl number, $Pr = C_p\mu/k$. The dynamic viscosity μ is a function of temperature T formulated by Sutherland's law of viscosity,

$$\mu = \frac{AT^{1.5}}{B+T} \tag{2.8}$$

where B is the Sutherland temperature and A is a property of the gas,

$$A = \frac{\mu_{ref}}{T_{ref}^{1.5}}(T_{ref} + B) \tag{2.9}$$

where μ_{ref} and T_{ref} are the reference dynamics viscosity and temperature respectively.

2.1.3 The Finite Volume Formulation

In the vector notation, the Navier Stokes equations (2.2—2.4) can be expressed as

$$\frac{\partial U}{\partial t} + \nabla.\vec{F} = 0 \tag{2.10}$$

where U is the vector of conserved variables.

$$U = [\rho, \rho u, \rho v, \rho w, E]^T \tag{2.11}$$

and $\vec{F}$ is the flux vector. Integrating the Equation 2.10 over a given volume V, we have

$$\int_V \frac{\partial U}{\partial t} dv = -\int_V \nabla.\vec{F} dv \tag{2.12}$$

Using the Divergence Theorem, we obtain

$$\frac{\partial \vec{U}}{\partial t} = -\frac{1}{V}\oint\!\!\!\!\int_S \vec{F}.\hat{n} ds \tag{2.13}$$

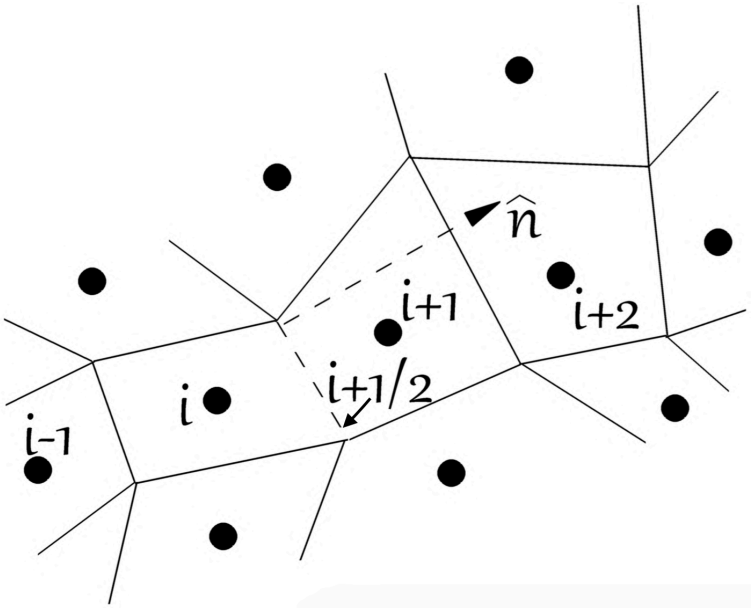

Figure 2.1: A schematic of mesh with cells $i-1, i, i+1, and i+2$.

where $\vec{U}$ is the volume-averaged state vector. For a finite volume cell made up of faces, Equation 2.13 can be written in the partially discrete form:

$$\frac{\partial \vec{U}}{\partial t} = -\frac{1}{V} \sum_{faces} (\vec{F}.\hat{n})S \tag{2.14}$$

where $\hat{n}$ is the outward-pointing unit normal vector related to each face and S is the area of the related face.

2.2 Numerical Methods

This section focuses the numerical methods applied in the present study to solve the governing equations. If $\vec{F}$ and a time-integration scheme are known, one can formulate the conservation equations in the form of Equation 2.12. Let us first discuss the methods to calculate the spatial fluxes. $\vec{F}$ can be decomposed into an inviscid and a viscous components:

$$\vec{F} = \vec{F_{inv}} + \vec{F_{visc}} \tag{2.15}$$

The inviscid component of the flux in the cartesian coordinates is

$$\vec{F_{inv}} = \vec{F_{inv}}\hat{i} + \vec{G_{inv}}\hat{j} + \vec{H_{inv}}\hat{k} \tag{2.16}$$

$$F_{inv} = \begin{bmatrix} \rho u \\ \rho uu + p \\ \rho uv \\ \rho uw \\ (E+p)u \end{bmatrix} \tag{2.17}$$

$$, G_{inv} = \begin{bmatrix} \rho v \\ \rho uv \\ \rho vv + p \\ \rho uw \\ (E+p)v \end{bmatrix} \tag{2.18}$$

$$, H_{inv} = \begin{bmatrix} \rho w \\ \rho uw \\ \rho vw \\ \rho ww + p \\ (E+p)w \end{bmatrix} \tag{2.19}$$

Similarly, the viscous component of the flux in the cartesian coordinates is

$$\vec{F_{visc}} = F_{visc}\hat{i} + G_{visc}\hat{j} + H_{visc}\hat{k} \tag{2.20}$$

$$F_{visc} = \begin{bmatrix} 0 \\ \tau_{xx} \\ \tau_{xy} \\ \tau_{xz} \\ \tau_{xx}u + \tau_{xy}v + \tau_{xz}w + q_x \end{bmatrix} \tag{2.21}$$

$$, G_{visc} = \begin{bmatrix} 0 \\ \tau_{xy} \\ \tau_{yy} \\ \tau_{yz} \\ \tau_{yx}u + \tau_{yy}v + \tau_{yz}w + q_y \end{bmatrix} \tag{2.22}$$

$$, H_{visc} = \begin{bmatrix} 0 \\ \tau_{xz} \\ \tau_{yz} \\ \tau_{zz} \\ \tau_{xz}u + \tau_{yz}v + \tau_{zz}w + q_z \end{bmatrix} \tag{2.23}$$

We compute the inviscid and the viscous components as mentioned in Equations 2.16—2.23 separately using different numerical methods.

2.2.1 Inviscid Fluxes

The inviscid flux is hyperbolic in nature as it propagates information along characteristics. To ensure numerical stability, a characteristic-based flux scheme by Steger and Warming (1981) is used. Let us consider $\vec{F}$ as the inviscid component instead of $\vec{F_{inv}}$ for the sake of presentation.

2.2.1.1 Steger-Warming Fluxes

$\vec{F}$ is homogeneous with respect to the state vector, i.e.

$$\vec{F}(\lambda U) = \lambda(\vec{F}U) \tag{2.24}$$

This homogeneity allows the flux to be defined exactly using a Jacobian with respect to the state vector:

$$\vec{F} = \frac{\partial \vec{F}}{\partial U}U = AU \tag{2.25}$$

where A is the flux Jacobian, and the eigenvalues of A are the characteristics of the inviscid flux. First, the inner product of $\vec{F}$ with the unit normal vector of the face is computed as

$$\vec{F}.\hat{n} = \begin{bmatrix} \rho u' & \rho u u' + p s'_x \\ \rho v u' & \rho u u' + p s'_y \\ \rho v u' & \rho w u' + p s'_z \\ & (E+p)u' \end{bmatrix} \tag{2.26}$$

Here, $u' = u s'_x + v s'_y + w s'_z$ and the orthonormal face vector is $\hat{n} = s'_x \hat{i} + s'_y \hat{j} + s'_z \hat{k}$. The flux Jacobian for this flux is now A', and therefore, $F' = A'U$. Since it is directly difficult to diagonalize A', we use a change of variables to diagonalization and then transform them back. Let us first define the set of primitive variables

$$V = [\rho, u, v, w, T]^T \tag{2.27}$$

A' is decomposed into $\frac{\partial F'}{\partial V}\frac{\partial V}{\partial U}$ and pre-multiplied by $\frac{\partial U}{\partial V}\frac{\partial V}{\partial U}$, yielding

$$A' = \frac{\partial U}{\partial V}\frac{\partial V}{\partial U}\frac{\partial F'}{\partial V}\frac{\partial V}{\partial U} \tag{2.28}$$

This operation is called a similarity transformation of A', and the similar matrix $\frac{\partial V}{\partial V}\frac{\partial F'}{\partial U}$ has the same eigenvalues shared by A'. The eigenvalue decomposition is

$$\frac{\partial V}{\partial U}\frac{\partial F'}{\partial V} = C\Lambda C^{-1} \tag{2.29}$$

where Λ is a diagonal matrix that corresponds to the eigenvalues, and C is the related matrix which contains the corresponding eigenvectors as its columns. Here u' is the characteristic propagation speed due to the bulk velocity, while $u' \pm a$ represent the characteristic propagation speeds due to the acoutic waves.

From Equations 2.25, 2.28 and 2.29, the inviscid flux can now be represented as

$$F' = \frac{\partial U}{\partial V} C\Lambda C^{-1} \frac{\partial V}{\partial U} U \tag{2.30}$$

Now we split F' into forward-moving and backward-moving components as

$$F' = F'_+ + F'_- \tag{2.31}$$

From Equations 2.30 and 2.31, we have

$$F'_\pm = \frac{\partial U}{\partial V} C \Lambda_\pm C^{-1} \frac{\partial V}{\partial U} U \tag{2.32}$$

where Λ_+ is the matrix related to only positive eigenvalues, $\frac{1}{2}(u'+|u'|)$ and $\frac{1}{2}(u'\pm a+|u'\pm a|)$. Let us consider the flux across a face between two elements designated by i and $i+1$, with the face designated by $i+1/2$. The flux across the face is computed as

$$F'_{i+1/2} = A_{+,i} U_i + A_{-,i+1} U_{i+1} \tag{2.33}$$

This is the flux vector-splitting scheme employed by Steger and Warming. This scheme is first-order accurate and is highly dissipative due to its upwind nature. Furthermore, Equation 2.33 indicates that forward moving information is computed using cells forward and behind the face where the scheme is operated. A simple modification that reduces the numerical dissipation is to evaluate the flux Jacobians at the face. This is accomplished by averaging the state vector of the cells on the either sides of the face. The resultant scheme named as Modified Steger-Warming scheme is

$$F'_{i+1/2} = A_{+,i+1/2} U_i + A_{-,i+1/2} U_{i+1} \tag{2.34}$$

$$A_{i+1/2} = A\Big(\frac{1}{2}(U_i + U_{i+1})\Big) \tag{2.35}$$

Whenever the eigenvalues are very nearly zero, particularly at the sonic line and in stagnation regions where numerical error can accummulate, this flux scheme can have issues. So to resolve these issues, we implement a correction named "sonic glitch correction" as

$$\lambda'_\pm = \frac{1}{2}\Big(\lambda_\pm \pm \sqrt{\lambda_\pm^2 + \epsilon^2}\Big) \tag{2.36}$$

where ϵ is a small fraction of the local speed of sound.

2.2.1.2 Higher-order spatial accuracy

To more accurately capture smaller scales of flow physics, particularly in the current study where flow transition is involved, higher-order spatial discretizations are needed. However, for fluxes that are upwinded, such as the Steger-Warming fluxes mentioned earlier, the added artificial viscosity damps out the small scales. The artifical viscosity is much higher than the physical viscosity, and therefore, for high Reynolds number flows, such high numerical damping can alter the actual Reynolds number of the flow. So, we split the flux into a central part, which contains no numerical dissipation, and the dissipative part resulting from the upwinding as shown below.

$$F'_{i+1/2} = (C^{-1}S^{-1}\Lambda^{+}SC)_{i+1/2}.U_L + (C^{-1}S^{-1}\Lambda^{-}SC)_{i+1/2}.U_R \tag{2.37}$$

where S and S^{-1} are transformation matrices defined as $\frac{\partial V}{\partial U}$ and $\frac{\partial U}{\partial V}$ respectively. The Equation 2.37 becomes

$$\begin{aligned} F'_{i+1/2} &= A.\Big(\frac{U_i + U_{i+1}}{2}\Big) - \frac{1}{2}|A|.(U_{i+1} - U_i) \\ F'_{i+1/2} &= A.\Big(\frac{U_i + U_{i+1}}{2}\Big) - \frac{1}{2}|A|.(\Delta U) \\ F'_{i+1/2} &= F_C + F_D \end{aligned} \tag{2.38}$$

In the Equation 2.38, the first part is central, while the second part is upwinded or dissipative. The second part makes apparent the reason why upwinding add artificial viscosity. Furthermore, the second part is the difference of states between i and i+1 cells across the i+1/2 face. Moreover, we know that the viscous fluxes are proportional to first derivatives of the primitive variables. So, the upwinding operation creates terms that numerically appear as viscosity. In the dissipative term, only (ΔU) changes with different reconstructions. The difference across the face at i+1/2 due to the first-order upwind, second-order upwind and third-order upwind biased reconstructions is the following respectively:

$$\begin{aligned} \Delta U_{1^{st}} &= U_{i+1} - U_i \\ \Delta U_{2^{nd}} &= \frac{1}{2}(U_{i-1} - 3U_i + 3U_{i+1} - U_{i+2}) \\ \Delta U_{3^{rd}} &= \frac{1}{8}(U_{i-1} - 3U_i + 3U_{i+1} - U_{i+2}) \end{aligned} \tag{2.39}$$

It is to be noted that the first-order extrapolation gives a difference proportional to the first derivative times the grid spacing, while the second-order and third-order extrapolations give a difference proportional to the third derivative times the grid spacing cubed. Furthermore, the second-order and third-order schemes yield identical results except for the factor of four. Therefore, increasing the order of accuracy in this dissipative term reduces artifical dissipation and improves the flow resolution significantly. To reduce the dissipation completely in regions where it is needed, dissipative flux component is multiplied by a factor α as shown below.

$$F = F_C + \alpha F_D \tag{2.40}$$

α is a numerical switch that must be able to detect regions of the flow where dissipation is required. One of the useful switches was developed by Ducros (1999) who used the ratio of the dilatation and the vorticity. So, this switch is physics based, and is shown in Equation 2.41.

$$\alpha = \frac{\theta^2}{\theta^2 + \omega^2 + \epsilon} \tag{2.41}$$

The divergence and vorticity are θ and ω, respectively, and ϵ is a small number. Let us now discuss the central portion of the flux. In terms to get a higher-order accuracy, the Jacobians are no longer used as they are inherently second order. Instead the flux is computed from a weighted average of data of i and i+1 sides of the face (i+1/2). We use gradients to expolate from the (i) and the (i+1) cells to the face (i+1/2). For an instance, $\phi_{i+1/2} = \phi_i + \nabla\phi_i.\Delta x$ leads to an extrapolation from the i cell. A similar extrapolation from the $i+1$ cell and then taking the mean value of the two extrapolations yield a larger stencil. We will show later that we use the known result of the gradient calculation in the i and the i+1 cells to optimally find the coefficients to put in front of the gradient term to obtain the accurate stencil weights.

$$\phi_f = \frac{\phi_i + \phi_{i+1}}{2} + \beta\Big(\frac{df}{dx}\Big|_i \Delta x_i + \frac{df}{dx}\Big|_{i+1} \Delta_{x_{i+1}}\Big) \tag{2.42}$$

Here, $\beta = 1/4$ and $1/3$ obtain a fourth-order interpolation at the face and a fourth-order gradient of the flux at the cell center after integrating over the cell surface. It is to be noted that Δx terms have respective signs from the cell center to the face center. The coefficients multiplying the gradient terms form a simple series that is only a function of the iteration number and the total number of iterations to be done. Given below are the series for both high order interpolations as well as the interpolations which give high-order gradients in

the cell center. Note that the latter is correct for the inviscid fluxes, in which the quantity of interest is the gradient of the flux.

$$\begin{aligned} \beta(j,n) &= \frac{2(n-j)+1}{4(n-j)+4) } - - - n^{th}\ order\ interpolation \\ \beta(j,n) &= \frac{(n-j)+1}{2(n-j)+3)} - - - n^{th}\ order\ gradient \end{aligned} \tag{2.43}$$

Here n is the total number of iterations to compute and j is the current iteration number. If a hexahedral grid is assumed (which can still be unstructured), it is possible to have a linear combination of extrapolations from a larger stencil. What is meant by this is the following:

$$\phi_{i+1/2} = \frac{\phi_i + \phi_{i+1}}{2} + \beta\Big(\frac{df}{dx}\Big|_i \Delta x_i + \frac{df}{dx}\Big)\Big|_{i+1} \Delta x_{i+1}\Big) + \gamma\Big(\frac{df}{dx}\Big|_{i-1} \Delta x_{i-1} + \frac{df}{dx}\Big)\Big|_{i+2} \Delta x_{i+2}\Big) \tag{2.44}$$

To obtain a sixth-order stencil, the weights to be chosen are β = 8/15 and γ = -1/45. The present study uses gradients from nearby neighbors and the sixth-order inviscid fluxes computed through gradient reconstruction. These fluxes obey a secondary conservatio of kinetic energy and are referred to in this document as Kinetic Energy Consistent (KEC) fluxes. As mentioned earlier, these fluxes are less dissipative than the MSW fluxes and allow more accurate representation of flow physics by capturing small-scale structures and a broader energy spectrum.

2.2.2 Viscous Fluxes

The viscous fluxes are relatively simpler to compute than the inviscid fluxes. But, it does need computation of gradients as all the fluxes are proportional to first derivatives of the primitive variables. Gradients are calculated at the cell center, while the fluxes are obtained at the face. First, we compute cell-centered gradients. Second, we compute face-centered gradients using the cell-centered gradients. Third, the calculation of viscous fluxes from face gradients is performed. One of the methods for computing cell centered gradients on an unstructured grid is Gauss' theorem. This theorem relates the average gradient in the cell to an integral over the surfaces of the cell.

$$\frac{\partial \phi}{\partial x_i} = \frac{1}{V} \sum_f \phi . \hat{n_i} S_f \tag{2.45}$$

Here, ϕ is any variable for which a gradient is desired at face f or $(i+1/2)$, V is the cell volume, $\hat{n}_i$ is the component of the unit surface normal in the direction of the gradient being computed, and S_f is the face area. This method works accurately for isotropic cells, but it is less accurate in cells with high aspect ratio. Particularly, in high-speed flows studied in the current work, the cells near walls have shorter length scales in the wall-normal direction in order to fully resolve the boundary layer. Due to this large aspect ratio of the near-wall cells, another method named weighted least square method is applied. In this method, the value at cell k is obtained by taking a Taylor expansion about cell i. Let us consider subscripts x and y as partial derivatives. For the sake of brevity, this method is explained in two dimensions. An extension to three dimensions is straight forward. A detailed derivation to express the spatial gradients of a required variable ϕ using this method is carried out elsewhere. So, the gradients obtained are shown below.

$$\begin{bmatrix} \phi_x \\ \phi_y \end{bmatrix} = \frac{1}{ac - b^2} \begin{bmatrix} c & -b \\ -b & a \end{bmatrix} \begin{bmatrix} d \\ e \end{bmatrix} \tag{2.46}$$

Here $a = \sum_k w_{ik}^2 \Delta x_{ik}^2$, $b = \sum_k w_{ik}^2 \Delta x_{ik} y_{ik}$, $c = \sum_k w_{ik}^2 \Delta y_{ik}^2$, $d = \sum_k w_{ik}^2 \Delta x_{ik} d\phi_{i,k}$, and $e = \sum_k w_{ik}^2 \Delta y_{ik} d\phi_{i,k}$. Also, $d\phi_{ik} = \phi_k - \phi_i = \phi_{x,i} \Delta x_{ik} + \phi_{y,i} \Delta y_{ik} + \mathcal{O}(\Delta x^2, \Delta y^2, \Delta x \Delta y)$. In the equation 2.46, the factor $(\frac{1}{ac-b^2})$ and the first matrix in the right-hand side depend only on the geometry of the grid and the weights. So, for a static mesh, these quantities can be computed once and stored while computing. The vector in the right-hand side is the one which changes with time and, therefore, is recomputed. Furthermore, based on the factor, if the weights are considered to be one, then, this factor will be in the $\mathcal{O}(\Delta x^4)$. If the Δx is small as in very small grid spacings, the system of equations will be ill-conditioned. So, the weights are selected as $1/\Delta x$ to make the factor in the $\mathcal{O}(1)$. Furthermore, it can be shown that the weights, in general, can be written as

$$w_{ki} = \frac{1}{\sqrt{\Delta x_{ki}^2 + \Delta y_{ki}^2}} \tag{2.47}$$

This approximation of weights is also second-order accurate. Once the gradients are constructed at all the cell centers, they must be interpolated to the face. A simple averaging between the two neighboring cells is inaccurate and leads to other numerical issues. So, the flux is rather calculated using a deferred correction method. In this method, the viscous flux

at the face is decomposed into a component normal to the face and a component tangential to the face:

$$\nabla\phi_{i+1/2} = (\nabla\phi_{i+1/2})_N + (\nabla\phi_{i+1/2})_T \tag{2.48}$$

$$\nabla\phi_{i+1/2} = (\nabla\phi_{i+1/2}.\hat{n})\hat{n} + (\nabla\phi_{i+1/2} - (\nabla\phi_{i+1/2}.\hat{n})\hat{n}) \tag{2.49}$$

The normal component is calculated as

$$(\nabla\phi_{i+1/2})_N \approx \Big(\frac{\phi_{i+1} - \phi i}{\mathbf{\Delta x}}\hat{e}.\hat{n}\Big)\hat{n} \tag{2.50}$$

where $\hat{e}$ is the unit vector pointing from the cell centroid at i to the cell centroid at i+1, and $\mathbf{\Delta x}$ is the distance between the two cell centroids. The tangential component is computed by simply averaging the cell-centered gradients as shown below.

$$(\nabla\phi_f)_T \approx \Big(\frac{\nabla\phi_i + \nabla\phi_{i+1}}{2}\Big) + \Big(\frac{\nabla\phi_i + \nabla\phi_{i+1}}{2}.\hat{h}\Big)\hat{n} \tag{2.51}$$

So, the deferred correction gradient at the face f,

$$\nabla\phi_f = \frac{\nabla\phi_i + \nabla\phi_{i+1}}{2} + \Big(\frac{\phi_{i+1} - \phi_i}{\mathbf{\Delta x}} - \frac{\nabla\phi_i + \nabla\phi_{i+1}}{2}.\hat{e}\Big)\hat{e} \tag{2.52}$$

2.2.3 Time Integration

2.2.3.1 Explicit Time Integration

In the earlier subsection, we computed the surface integral (the right hand side) of the governing equations. Now let us march the solution in time. One of the simpliest methods to time-march the solution is a first-order Explicit method. If a superscript n corresponds to the time level of the solution, explicit Euler uses data at the n level to update the solution at the n+1 level.

$$U_i^{n+1} = U_i^n - \frac{\Delta t}{V_i}\sum_f (F_f^n S_f) \tag{2.53}$$

This scheme is conditionally stable and the condition is given by:

$$\Delta t \leq \frac{\Delta x}{|u'| + c} \tag{2.54}$$

where c is the local sound speed. In another way, we define the numerical stability of the scheme using a number called Courant number (or Courant-Fredericks-Lewy or CFL).

$$CFL = \frac{\Delta t(|u'| + c)}{\Delta x} \tag{2.55}$$

For this scheme to be numerically stable, $CFL \leq 1.0$. Defining an operator, $SS^{(n)}$, that is the surface integral of the fluxes at stage n as

$$SS_i^n = -\frac{\Delta t}{V_i} \sum_f (F_f^n S_f) \tag{2.56}$$

then the explicit Euler method can more accurately written as

$$U_i^{n+1} = U_i^n + L_i^n \tag{2.57}$$

L_i^n is defined as

$$L_i^n = -\frac{\Delta t}{V_i} \sum_f (F_f^n S_f) \tag{2.58}$$

2.2.3.2 Implicit Time Integration

In the present study, the size of domain is large $\mathcal{O}(6)$. So, to be able to take large time steps ($CFL \geq 1.0$) and maintain numerical stability at the same, an implicit method is implemented. For this purpose, the fluxes are evaluated at the n+1 time level, and therefore, must be linearized and a coupled system solved. The linearized flux is split using the split Jacobians. The viscous fluxes is also linearized, but illustrated else where.

$$\begin{aligned} F_f^{n+1} &= F_f^n + \frac{\partial F}{\partial U}\Big|_f^n (U_f^{n+1} - U_f^n) + \mathcal{O}(\Delta t)^2 \\ F_f^{n+1} &= F_f^n + A_f^n \delta U_f^n \\ F_f^{n+1} &= F_f^n + A_f^{+n} \delta U_i^n + A_f^{-n} \delta U_{i+1}^n \\ F_f^{n+1} &= F_x^n f + \delta F_f^{+n} + \delta F_f^{-n} \end{aligned} \tag{2.59}$$

So, the equation to be solved using the linearized flux is shown below.

$$\delta U_i^n = L_i^n - \frac{\Delta t}{V_i} \sum_f (A_f^{+n} \delta U_i^n + A_f^{-n} \delta U_{i+1}^n) S_f \tag{2.60}$$

It is to be noted that f is the face $(i+1/2)$ shared by cells i and $i+1$. To computationally solve this system, which is fully coupled, we implement relaxation steps. Since there are mesh singularities in the domain, point-relaxation method is preferred over line-relaxation method. Furthermore, this method uses a block-diagonal matrix to solve while maintaining tight coupling for all degrees of freedom within a computational cost. This method has no bias in how the implicit linear system of equations is relaxed to convergence, it is suitable for unsteady, time-accurate simulations like the present study. Writing the system as

$$\Big(I + \frac{\Delta t}{V_i}\sum_f A_f^{+n} S_f\Big)\delta U_i^n + \frac{\Delta t}{V_i}\sum_f A_f^{-n} S_f \delta U_{i+1}^n = L_i^n \tag{2.61}$$

Rearranging the Equation 2.61,

$$\delta U_i^k = \Big(I + \frac{\Delta t}{V_i}\sum_f A_f^{+n} S_f\Big)^{-1}(L_i^n - \frac{\Delta t}{V_i}\sum_f A_f^{-n} S_f \delta U_{i+1}^{k-1}) \tag{2.62}$$

where $k = 1 \rightarrow k_{max}$. k_{max} is a specified number of iterations. Typically, $k_{max} = 4$ is sufficient to relax the system in a given time step. To obtain a higher order of temporal accuracy, one of the methods is second-order backward difference for the discretization of the time derivative. If the time step is constant, it takes the following form.

$$\frac{\partial U}{\partial t}\Big|_i = \frac{3U_i^{n+1} - 4U_i^n + U_i^{n-1}}{2\Delta t} \tag{2.63}$$

After rearranging the equation, we obtain the final equation:

$$\delta U_i^n = -\frac{2\Delta t}{3V_i}\sum_f F_f^{n+1}.S_f + \frac{1}{3}\delta U_i^{n+1} \tag{2.64}$$

It is observed to see some dispersion into the solution. But, if the mesh resolution is sufficient, the dispersion is observed to be negligeable in most cases including high-speed flows.

2.2.4 Boundary Conditions

The governing equations need boundary conditions to time-march the solution. To do so, suitable boundary conditions have to be implemented. This measure is accomplished by adding a layer of cells around the interior cells. These added cells are called boundary or

ghost cells. Since the governing equations are based on finite-volume approach, these cells are assigned boundary values in terms of conservative variables. Let us first discuss the explicit boundary conditions followed by implicit boundaries.

2.2.4.1 Explicit Boundary Conditions

Explicit boundary conditions are relatively more straightforward to execute as compared to implicit boundary conditions. The values in the ghost cells must be assigned based on the desired values of corresponding interior cells. This assignment is critical to ensure that the boundary conditions are correct, and therefore, the solution.

No-Slip Wall: A real wall surface obeys the no-slip condition and is solid (impermeable). This condition means the velocity of fluid is zero at the wall. If the flow velocity is decomposed in to tangential (u_t) and normal (u_n) components, then, the following relations hold.

$$\begin{aligned} u_{t,ghost} &= -u_{t,interior} \\ u_{n,ghost} &= -u_{n,interior} \end{aligned} \tag{2.65}$$

Symmetry: A symmetry (or slip wall) boundary condition which is impermeable only requires that fluid does not penetrate the surface, i.e. u_n at the face is equal to zero, giving

$$\begin{aligned} u_{t,ghost} &= u_{t,interior} \\ u_{n,ghost} &= -u_{n,interior} \end{aligned} \tag{2.66}$$

Pressure: Pressure boundary condition at either wall or symmetry is shown below

$$p_{ghost} = p_{interior} \tag{2.67}$$

Adiabatic Wall: An adiabatic wall has the wall normal component of the temperature gradient at wall equal to zero, which is actually a Neumann boundary condition shown as

$$\frac{\partial T}{\partial \eta}\Big|_{wall} = 0 \tag{2.68}$$

where η is the wall-normal ordinate.

Isothermal Wall: An isothermal wall has the constant temperature (T_w), which is

actually a Dirichlet boundary condition shown in Equation 2.69.

$$T = T_w \tag{2.69}$$

Supersonic Inflow No characteristics travel out of the inflow boundary condition. This setup means the inflow boundary condition drives the interior cells. Freestream conditions are set-up in the cells carrying this inflow boundary condition.

Supersonic Outflow Similar to the supersonic inflow, supersonic outflow boundary condition has no flow characteristics traveling back to the domain which means the interior cells are not dependent on the ghost cells. This independence of the interior cells means the ghost cells are set same as the interior cells.

2.2.4.2 Implicit Boundary Conditions

While using an implicit time-marching scheme, updating explicitly boundary values or values of the ghost cells after implicitly updating the interior cells can cause numerical instability. Therefore, these ghost cells must be implicitly updated along with the interior cells to maintain numerical stability. The ghost cells are related to the interior cells as

$$U_{ghost} = GU_{interior} \tag{2.70}$$

The matrix G is determined for each ghost cell. Based on the explicit boundary conditions, where primitive variables are imposed, we can write

$$\delta V_{ghost} = R\delta V_{interior} \tag{2.71}$$

where R is known.

Tranforming this equation using $\delta U = \frac{\partial U}{\partial V}\delta V$, we obtain the following equation as

$$\delta U_{ghost} = \frac{\partial U}{\partial V} R \frac{\partial V}{\partial U} \delta U_{interior} \tag{2.72}$$

$$\delta U_{ghost} = E\delta U_{interior} \tag{2.73}$$

where $E = \frac{\partial U}{\partial V} R \frac{\partial V}{\partial U}$.

The implicit part of the flux for a boundary face then changes as

$$A_f^+ S_f \delta U_i + A_f^- S_f \delta U_{i+1} = \left(A_f^+ + A_f^- S_{ghost}^{-1} G S_{interior} \right) S_f \delta U_i \tag{2.74}$$

Chapter 3

Passive Tripping

In this chapter, we investigate the instability mechanisms of transitional hypersonic boundary layers due to an isolated diamond-shaped trip and an array of diamond-shaped trips (Semper and Bowersox 2017) using a combination of DNS, DMD, and PSD. First, we qualitatively compare instability mechanisms between the isolated cylindrical trip (Subbareddy et al. 2014) and the isolated diamond-shaped trip. Second, we compare the mechanisms between the isolated diamond-shaped trip and the array of diamond-shaped trips. A schematic of the overall objective of this chapter is shown in Figure 3.1. To build confidence in our simulations, we compare DNS data with the available experimental data.

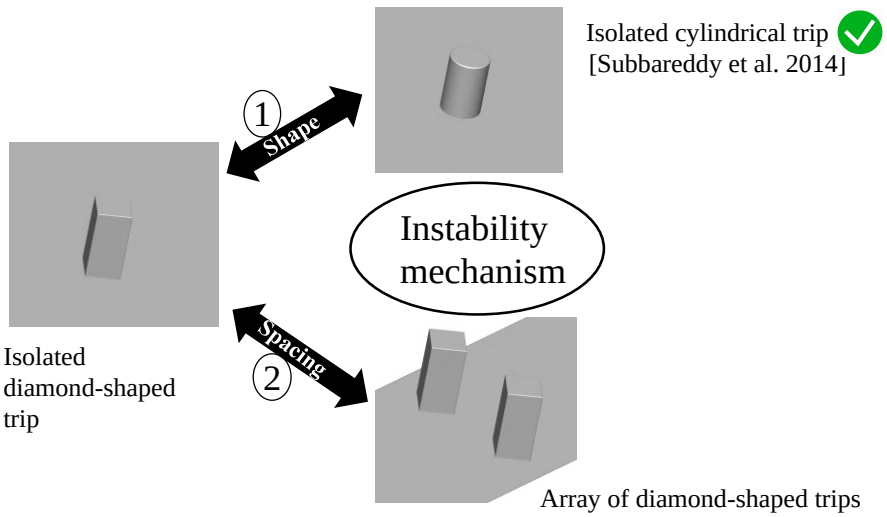

Figure 3.1: A schematic of the comparison among present trip configurations.

3.1 ACE wind tunnel facility

Numerical simulations, consisting of the trip array, were performed in conjunction with an experimental campaign (Semper and Bowersox 2017) carried out in the Actively Controlled Expansion (ACE) high-speed wind tunnel. This facility is a hypersonic blow-down wind tunnel located at Texas A & M University. Uniform Mach numbers (to within 1%) over a range of 5-7 are produced using a variable Mach number mechanism along with a range of Re/m from 0.7-7.0 million/meter. The runtime of the facility is 40 sec. The experiment is conducted on a 7.62-mm thick flat plate (508-mm long and 356-mm wide) with a 1.59 mm radius blunt leading edge. The leading edge of the model is positioned along the vertical centerline of the tunnel. The plate is aligned at an angle of attack of -2 degrees to promote a favorable pressure gradient near its leading edge on the top surface. Trips are located at 95.2 mm (x_{trip}) from the leading edge of the flat plate. Trip height (k) is 4.76 mm and spanwise spacing between two trip centers (s) is 6.36 mm ($s/D = 2$).

Freestream conditions of the experimental campaign are shown in Table 3.1.

Table 3.1: Freestream conditions: ACE facility at Texas A & M University.

SN	Mach number (M_∞)	Temperature (T_∞)	Pressure (P_∞)	Unit Re_∞/m
1	5.92	53.04 K	308 Pa	4.6×10^6/m

The post-shock Mach number (M_2) is 5.65. For more details about the experimental facility and the campaign, the reader is referred to Semper and Bowersox (2017) and references therein. A schematic of the ACE wind tunnel flow path is shown in Figure 3.2. Schematics of the trip geometry and the flat plate used in the experiment are shown in Figures 3.3 and 3.4.

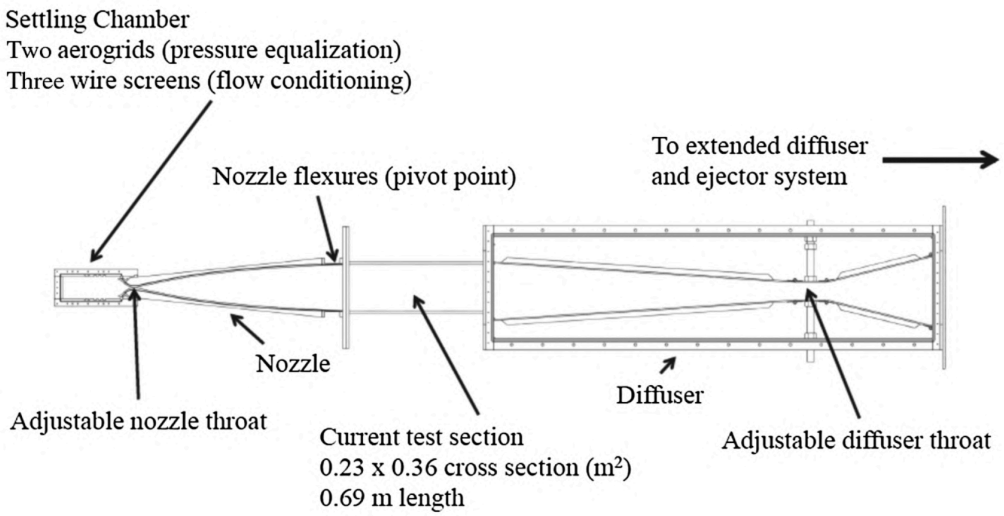

Figure 3.2: A schematic of the ACE wind tunnel flow path. Reproduced from Semper & Bowersox (2017).

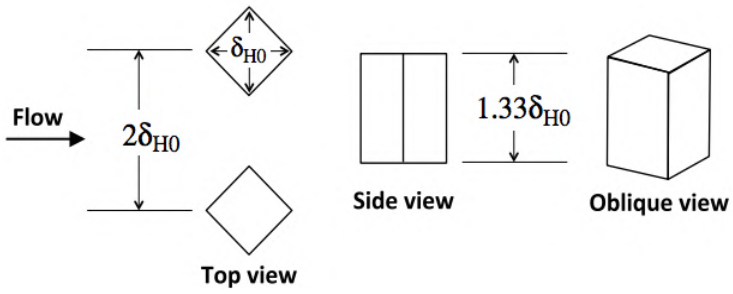

Figure 3.3: A schematic of the trip geometry. Reproduced from Semper & Bowersox (2017). δ_{H0} (=3.18 mm) is the laminar boundary-layer height at which the value of enthalpy is 99.5% of the freestream enthalpy.

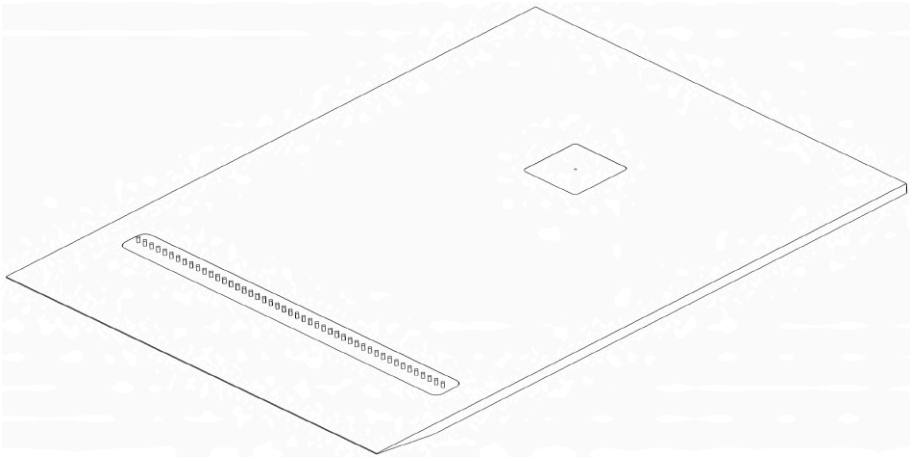

Figure 3.4: A schematic of an array of diamond-shaped trips on a flat plate. Reproduced from a draft of Semper & Bowersox (2017).

3.2 Computational setup

The present study utilizes an unstructured-grid finite-volume Navier-Stokes solver, US3D (Candler et al. 2015), to simulate these flows. The solver has been extensively validated for numerous unsteady and compressible flow configurations including compressible boundary layers and strong shock waves.

As discussed in chapter 2, the inviscid flux is split into symmetric (non-dissipative) and upwind (dissipative) portions. The sixth-order accurate central KEC scheme is used to calculate the symmetric portion, and the viscous fluxes are computed using second-order centered differences. Time integration is achieved using a second-order, implicit Euler method with point relaxation to maintain numerical stability and accuracy. The implicit system is solved with the full matrix data-parallel method (Wright, Candler & Prampolini 1996).

We model the flow in the ACE wind tunnel starting at the leading edge of the plate. For computational efficiency, we first perform a two-dimensional simulation over a flat plate that extends 70 mm from its leading edge. Boundary conditions of the two-dimensional domain are: the inflow is supersonic, the wall is adiabatic (the runtime of the facility is sufficient to equilibrate the wall temperature), and the outflow is supersonic. We extract wall-normal profiles of flow data at 30 mm (from the leading edge) of the two-dimensional domain. Second, we perform separate three-dimensional simulations using an isolated diamond-shaped

trip and an array of diamond-shaped trips. We impose the extracted wall-normal profiles as the inflow boundary conditions of the three-dimensional simulations across the span. The streamwise location of the wall-profile extraction at 30 mm is selected to minimize the effects of the upstream region of the trips on the inflow boundary of the three-dimensional simulations and maintain their computational efficiency. In the experiment, there are forty-seven trip elements. We use an array of two trips with periodic boundary conditions in the spanwise direction for computational efficiency. The use of the two trips also captures a fundamental and its subharmonic spanwise modes. Three-dimensional domains of both trip configurations extend (streamwise) from 30 mm to 604 mm relative to the leading edge of the flat plate. Similar to the two-dimensional domain, the wall and the outflow boundary conditions are adiabatic and supersonic respectively. A schematic of the boundary conditions for the three-dimensional domain of the trip array is shown in Figure 3.5. The wall is curved at the end of the three-dimensional domain to minimize noises propagating upstream from the outflow boundary. The two trips are centered at $x/D = 0$, $z/D =$ -1 and $x/D = 0$, $z/D = 1$. The spanwise extent of the domain with the isolated diamond-shaped trip is $20D$ (-10 $\leq z/D \leq$ 10). The isolated trip is centered at ($x/D = 0$, $z/D = 0$). In both three-dimensional domains, the upper edges of the trips are filleted with a radius of 10 micrometers to generate smooth grids near the edges. A constant time step (Δt) of 20 ns is used in all the present simulations. We obtain a statistically-converged solution after approximately 50 flow times (X_{trip}/U_∞) in both trip configurations.

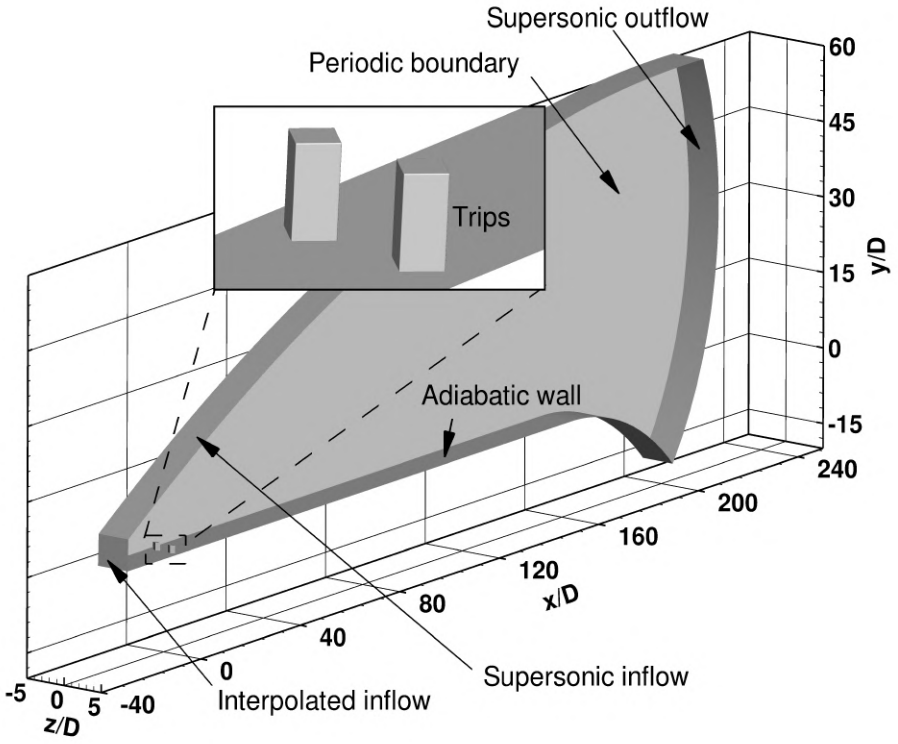

Figure 3.5: A schematic of boundary conditions of the three-dimensional domain using the trip array. Flow direction: left to right.

Freestream disturbances are imposed in our calculation to both two- and three-dimensional domains in order to replicate ambient experimental conditions. These disturbances have a substantial effect on roughness-induced transition (Borg, Schneider & Juliano 2008). Of the three possible disturbance modes (acoustic, entropy and vorticity), the acoustic mode, which originates from the turbulent boundary layer on the nozzle wall, is dominant (Laufer 2012). The freestream disturbances are thus approximated as acoustic. We impose the disturbances as flow-parallel for simplicity. The pressure is assumed to have the following spectral form to satisfy the dispersion relation,

$$p'(t) = \sum_{k=-N}^{k=N} p'_k e^{i(\alpha_k^{\pm})x - w_k t} \tag{3.1}$$

$$\alpha_k^{\pm} = \frac{w_k}{U_\infty \pm c_\infty} \tag{3.2}$$

where, p' is the time-dependent pressure fluctuation, p'_k is the complex frequency content of the k^{th} frequency, $\alpha_k^{\pm}$ are the fast- and slow-moving wavenumbers, w_k is the angular frequency, x is the direction of the disturbance, t is time, U_∞ is the freestream velocity, and c_∞ is the freestream speed of sound. In our case, only fast-moving waves are considered because the inflow boundary condition of the two-dimensional domain is supersonic. Using the linearized Euler equations, we obtain the following relations:

$$\begin{bmatrix} \rho'_k \\ u'_k \\ T'_k \end{bmatrix} = \begin{bmatrix} \frac{1}{c_\infty^2} \\ -\frac{\alpha^{\pm}}{\rho_\infty(\alpha^{\pm}U_\infty - w_k)} \\ \frac{(\gamma-1)T_\infty}{\rho_\infty c_\infty^2} \end{bmatrix} p'_k \tag{3.3}$$

We can represent the pressure fluctuations in Fourier coefficients as:

$$p'(t) = \sum_{k=1}^{k=N} 2|p'_k| cos(\alpha_k^{\pm} x - w_k t + \phi_{p,k}) \tag{3.4}$$

$$|p'_k| = \sqrt{\text{Real}(p'_k)^2 + \text{Imaginary}(p'_k)^2} \tag{3.5}$$

$$\phi_{p,k} = \tan^{-1}\left(\frac{\text{Imaginary}(p'_k)}{\text{Real}(p'_k)}\right) \tag{3.6}$$

In the above equations, $|p'_k|$ is the amplitude and $\phi_{p,k}$ is the phase of the k^{th} frequency component of pressure. Thus, the inflow profile is characterized using the pressure amplitude spectrum. $\phi_{p,k}$ is random between 0 and 2π to prevent superposition of peaks of different frequency modes. Furthermore, we filter the given PSD data from the facility using an interval of 2 kHz to accurately resolve the frequencies of interest. Therefore, a filtered set of frequencies considered ranges from 2 kHz to 250 kHz in the present study. The inflow freestream disturbances with and without filtering are shown in Figure 3.6. Local spikes observed in the experimental spectrum could be due to Mach waves generated by static ports drilled into the nozzle side walls, inconsistent machining at the throat of the nozzle, or disturbances created by leaks at the settling chamber-nozzle interface (Semper, Pruski and Bowersox 2012). We assume frequencies above 80 kHz do not play significant roles in

flow dynamics in our case and, therefore, spikes above 80 kHz are filtered out.

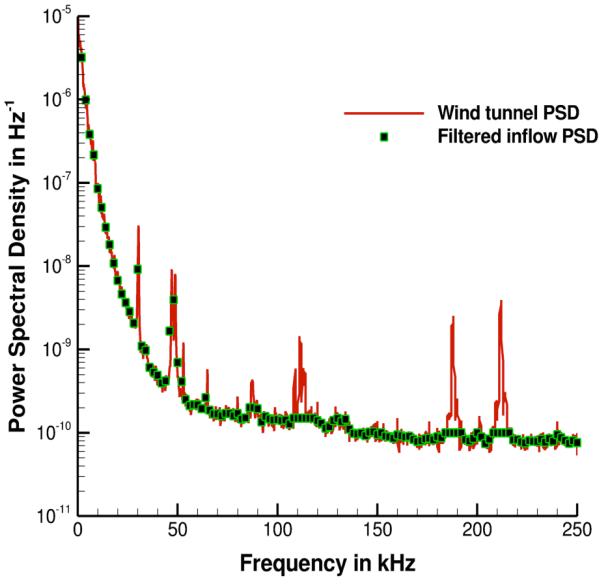

Figure 3.6: Filtering of the experimental freestream disturbances.

3.2.1 Grid convergence study

Unstructured grids are generated using LINK3D, a grid generator with a built-in parallel smoother. More information about LINK3D can be found in Drayna et al. (2016). The unstructured grids contain hexahedral cells clustered into a large number of three-dimensional i, j, k-ordered blocks. The grid generator allows a nested-refinement of the block topology which makes it possible to construct a high-resolution corridor around the roughness element. Away from this corridor, the grid is coarsened to keep the total grid size computationally efficient. Figure 3.7(a) shows the grid topology around a single diamond-shaped trip. Figures 3.7(b) and 3.7(c) show the grid in the vicinity of the trip from the top and the isometric views respectively.

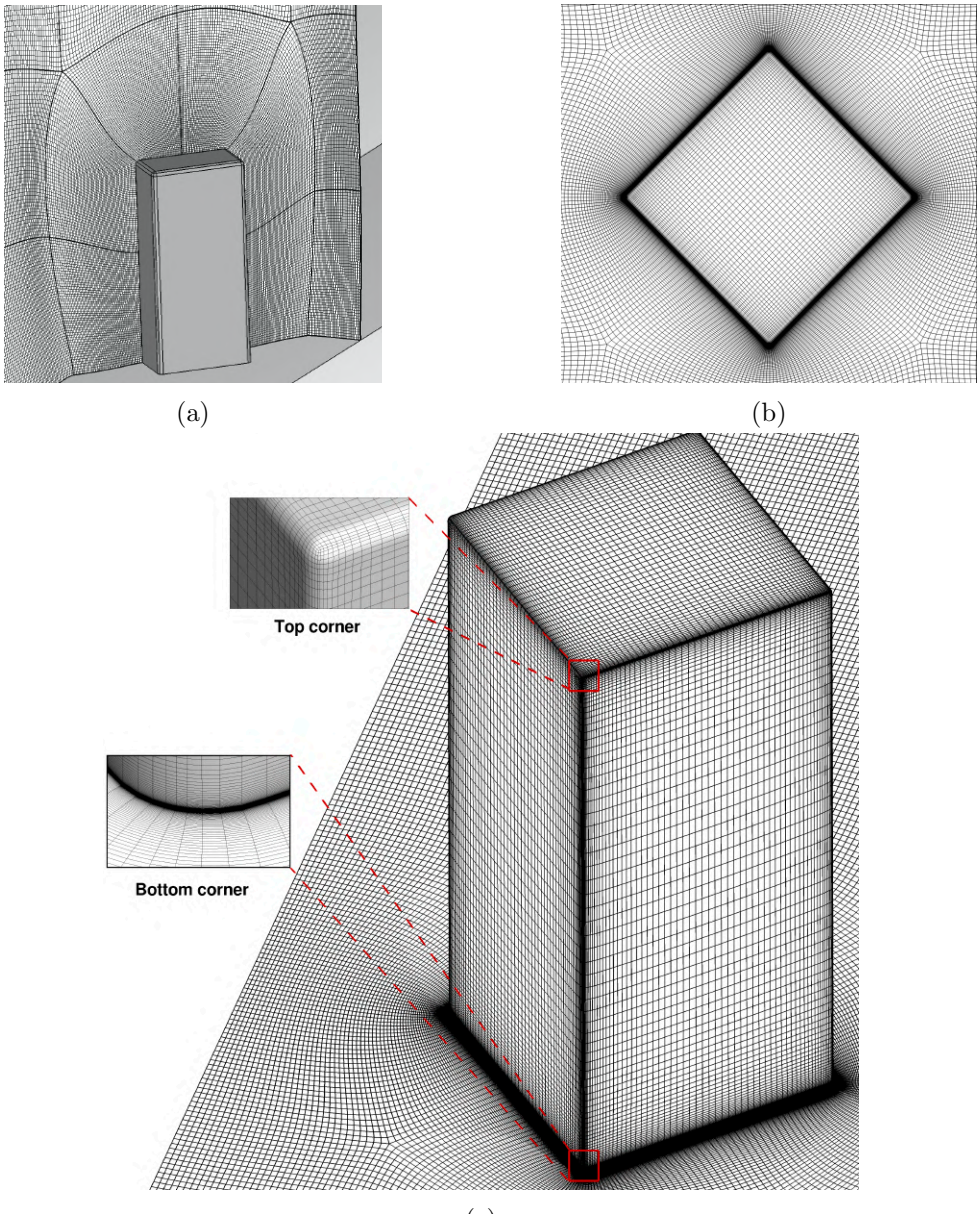

(a) (b)

(c)

Figure 3.7: (a) Grid topology (the grid is refined in a corridor surrounding the diamond-shaped trip in order to resolve the flow physics while keeping the total grid size manageable), (b) the top view of mesh, and (c) three-dimensional surface mesh around the trip.

Grid convergence studies are carried out for both trip configurations. As these studies are similar in both trip cases, we only present the convergence studies using the trip array. For a three-dimensional domain containing the trip array, we use a series of truncated

domains to conduct a grid convergence study. The domains are truncated at $x/D = 50$. Consistent with Subbareddy et al. (2014), the number of grid points diagonally spanning one of the diamond-shaped trips is used to conduct the grid convergence study. Spacings of 16 p.p.d. (points per diagonal) and 32 p.p.d. correspond to the truncated domains of 25 and 50 million cells, respectively. The y^+ of the near-wall grid spacing for the two- and three-dimensional domains is 0.1. A sampling frequency (f_s) of 5 MHz and the total samples (N) of 10,000 are used to compute the time-averaged, the root mean square (RMS), and PSD (using Hanning window by Harris 1978) of a flow quantity of interest in the present study. PSD of pressure (for an example) is computed as shown in Equation 5.1, where k ranges from 1 to N_f discrete frequency disturbances and $\overline{p}$ is the mean pressure.

$$PSD_k(\mathrm{Hz}^{-1}) = \frac{1}{2f_s}\left(\frac{|p'_k|}{\overline{p}}\right)^2 \tag{3.7}$$

Figures 3.8(a) and3.8(b) show grid convergence studies performed using time-averaged streamwise mass fluxes and spanwise wall shear stress in the two truncated domains. At all streamwise locations, the results agree well with each other. In Figure 3.9, PSD of pressure is plotted at $x/D = 26$, $y/D = 1.5$ and $z/D = 1$ in the two truncated domains. Local peaks at around 29 kHz and 45 kHz correspond to characteristic wind-tunnel noise (Semper & Bowersox 2017). However, the finer-grid domains (50 and 75 million cells) more accurately capture a local peak at 58 kHz when compared with the experimental data at the same probe location in the next section. It will also be shown later that the local peak at 58 kHz is associated with a dominant mode of instability induced by the trip array. This finding indicates that the truncated domain with 50 million cells is grid converged and accurately captures high-frequency coherent structures of interest. In the case of the isolated diamond-shaped trip, the three-dimensional domain with 90 million cells is also grid converged using the same time-averaged variables.

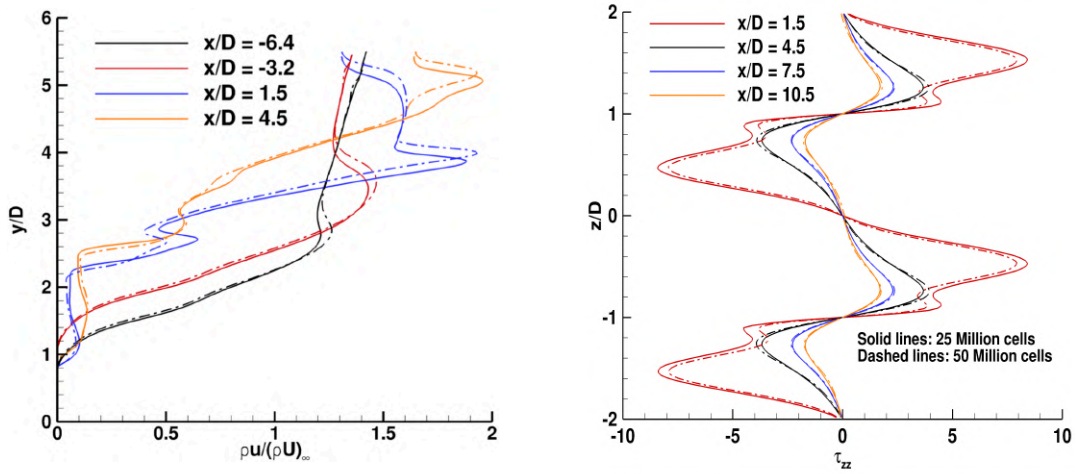

(a) (b)

Figure 3.8: Grid convergence study of the three-dimensional domain consisting of the trip array using nondimensionalized (a) mean streamwise mass flux in the wall-normal direction, (b) mean spanwise wall shear stress across spanSolid lines: 25 million cells (16 p.p.d.) and dashed lines: 50 million cells (32 p.p.d.).

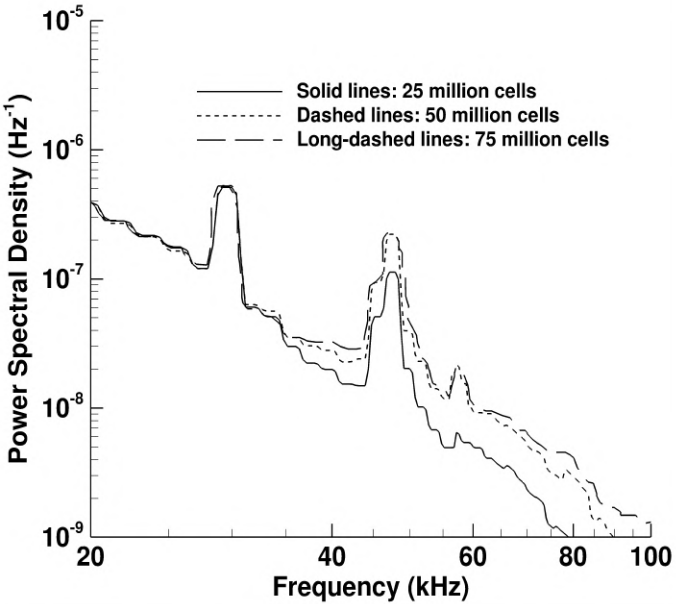

Figure 3.9: Grid convergence study of the three-dimensional domain consisting of the trip array using nondimensionalized power spectral density (PSD) of pressure vs. frequency at $x/D = 26$, $y/D = 1.5$, and $z/D = 1$. Solid lines: 25 million cells (16 p.p.d.), dashed lines: 50 million cells (32 p.p.d.) and long-dashed lines: 75 million cells (48 p.p.d.).

3.3 Comparison with experiment

In this section, the trip array DNS data are compared to the experiment using the wall-normal mean profiles of the streamwise mass flux, van Driest transformed velocity, and Mach number. We also compare the PSD of pressure from the trip array DNS to the experiment.

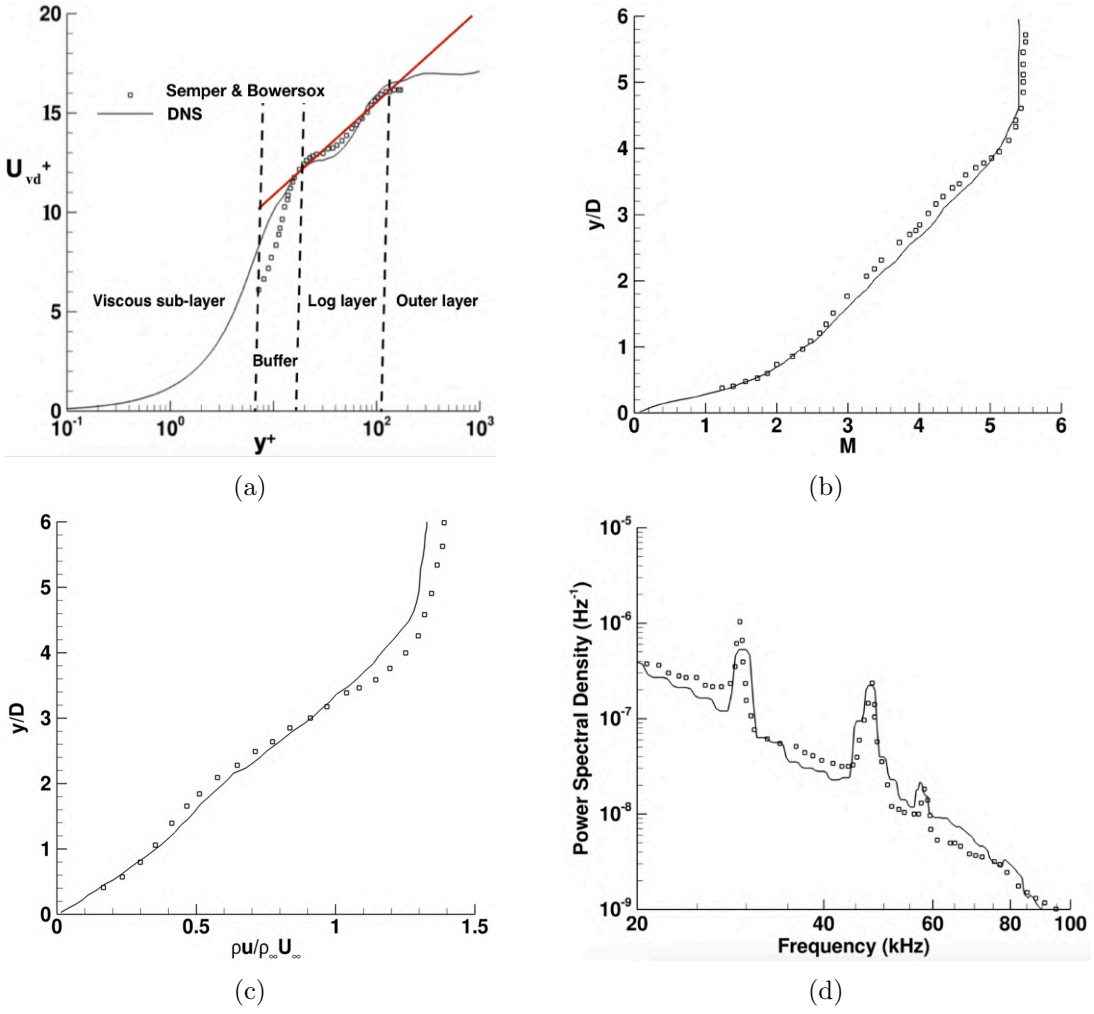

Figure 3.10: Wall-normal profiles of (a) van Driest transformed mean velocity, (b) mean Mach number, (c) mean streamwise mass flux at $x/D = 86$, and (d) PSD of pressure at $x/D = 26$ and $y/D = 1.4$. All plots are at $z/D = 1$.

The van-Driest-transformed mean velocity profile (van Driest 1956 and van Driest and Blumer) is given by:

$$\mathrm{U_{vd}}^{+} = \int_0^{U^+} \frac{\rho}{\rho_w} dU^+ \tag{3.8}$$

In Figure 3.10(a), experimental and computed plots of the van Driest transformed mean velocity profiles are presented. In the buffer region, we observe good agreement for larger y^+ values, while in the log-law region, there is close agreement for all y^+ values. In Figure 3.10(b), the mean Mach number profiles from the DNS reasonably agrees with the experimental data.

Figure 3.10(c) presents a comparison of the mean streamwise mass flux (normalized by freestream mass flux) with the experiment at $x/D = 86$ on the symmetry plane ($z/D = 1$). We observe that there is close agreement between the numerical simulation and the experiment. PSD plots of pressure at ($x/D = 26$, $y/D = 1.4$, $z/D = 1$) are shown in Figure 3.10(d). There is fair agreement between the experiment and the present study especially around peaks at 29 kHz, 45 kHz, and 58 kHz. In Figure 3.11, a Schlieren photograph of the experiment and an instantaneous density gradient magnitude (DGM) plot from the simulations are compared. The orientation of the upstream vortex system, the structure of the shock system, and the shear layers observed in the experiment and the simulations agree well.

We, therefore, have confidence in our simulations containing the trip array. We can extend this confidence to the isolated trip since both trip configurations share similar attributes regarding boundary conditions and meshing.

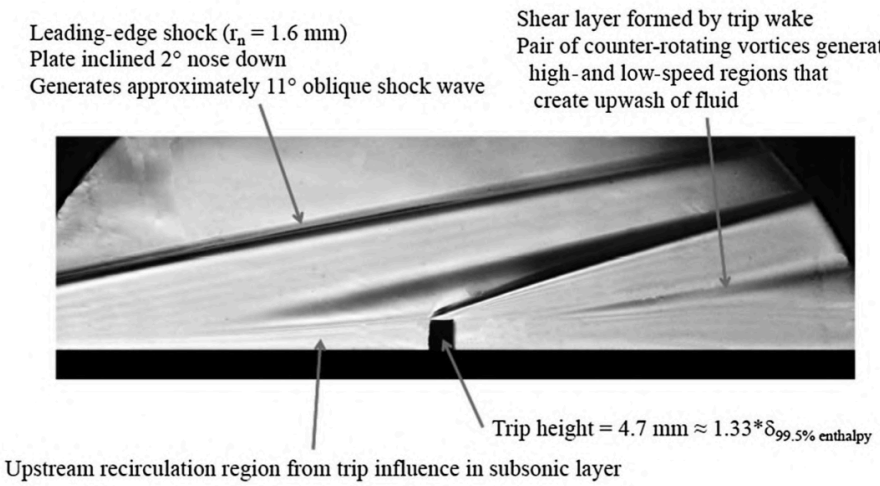

(a)

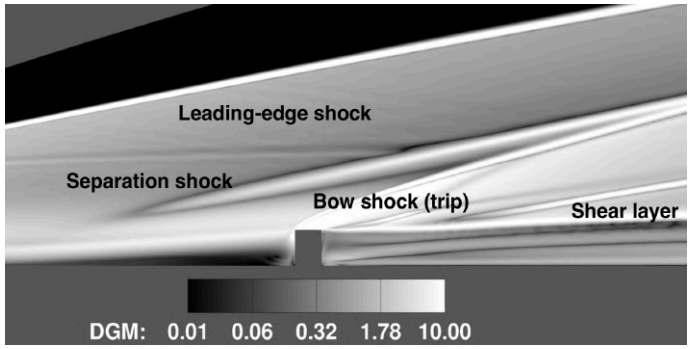

(b)

Figure 3.11: (a) Schlieren photograph from the experiment (Semper and Bowersox 2017) and (b) density gradient magnitude (DGM) contours from DNS at $z/D = 1$.

3.4 Results

We first investigate the isolated diamond-shaped trip and compare its instability mechanism with the isolated cylindrical trip (Subbareddy et al. 2014). Later we study this mechanism in the case of the trip array and compare it with the isolated diamond-shaped trip. No freestream disturbances are imposed so as to analyze the flow physics without freestream noise. The freestream values are used to nondimensionalize their respective field variables. Particularly, frequency in Hz is nondimensionalized to Strouhal number (St), which is based on U_∞ (freestream velocity) and D. The PSD of a flow quantity is normalized by its mean

value.

3.4.1 Isolated diamond-shaped trip

In this subsection, we characterize three distinct regions of unsteadiness in the isolated diamond-shaped trip flowfield as shown in Figure 3.12. The three regions are (1) the upstream vortex system, (2) the shock system ahead of the trip, and (3) the shear layers and the associated counter-rotating streamwise vortices which originate from its top, sides, and downstream surfaces. The Q-criterion (Hunt, Wray and Moin 1988) isosurfaces show the rotational motion of the upstream vortex system as well as the counter-rotating streamwise vortex pair (CVP) downstream. The Q-criterion is the second invariant of the velocity gradient tensor, and is used to identify vortices.

$$Q = -\frac{1}{2}\frac{\partial u_i}{\partial x_j}\frac{\partial u_j}{\partial x_i} \tag{3.9}$$

In Figure 3.12, we observe streamwise fluctuations of isosurfaces of Q-criterion downstream of the trip. These fluctuations later become hairpin-like structures, and eventually flow breakdown occurs. Next, we determine the source of these fluctuations and their critical frequencies, and compare with the isolated cylindrical trip.

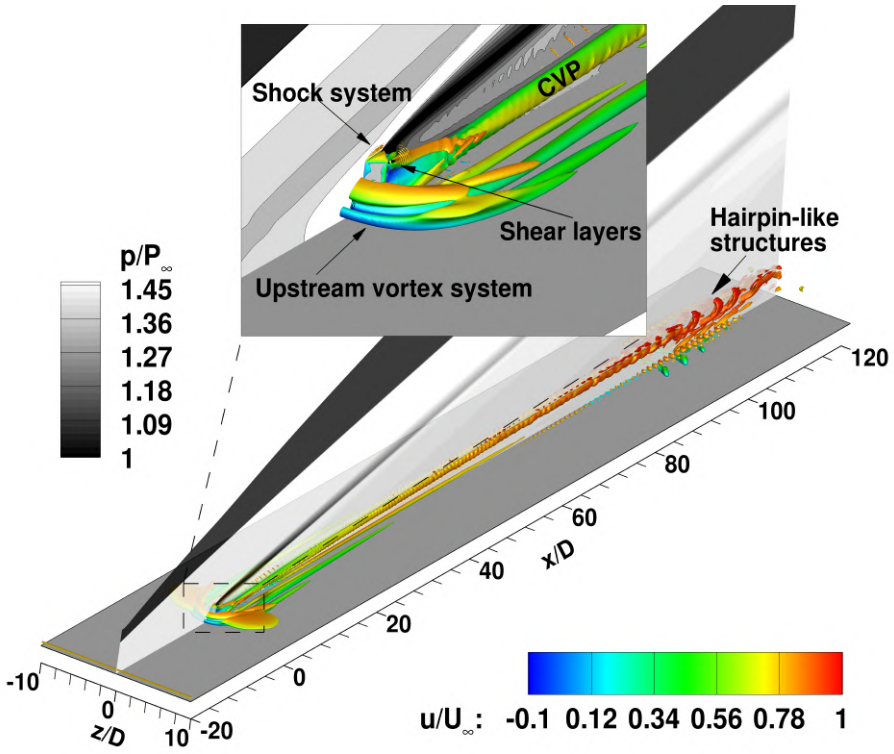

Figure 3.12: Q-criterion ($=2.5\times10^8$) isosurfaces colored by instantaneous streamwise velocity upstream and downstream of the isolated diamond-shaped trip. A symmetry plane is shaded by instantaneous pressure contours.

3.4.1.1 Upstream vortex system

First, let us consider the upstream vortex system that forms in front of the trip. Figure 3.13(a) shows that the mean recirculation region extends approximately $3D$ upstream of the trip. In the mean flow, there is a three-vortex system as shown in Figure 3.13(b). Probe 1 (see Figure 3.13b) is located in the upstream vortex system to quantify unsteadiness and find peak-amplitude frequencies using the PSD (pre-multiplied by St) of pressure fluctuations. In Figure 3.14, the PSD indicates that the peak-amplitude frequency is at St = 0.0123 (3 kHz) and a local peak frequency at St = 0.055 (15 kHz). The low-frequency unsteadiness at St = 0.0123 in the upstream vortex system is because the current simulation is at low Reynolds number ($Re_k = U_\infty k/\nu_\infty$= 24,000). Thus, this finding also agrees with Baker (1979), in which low-Reynolds number flow was found to have steady or low-frequency unsteady vortices in incompressible flows. The upstream vortices wrap the trip

to form horseshoe vortices downstream.

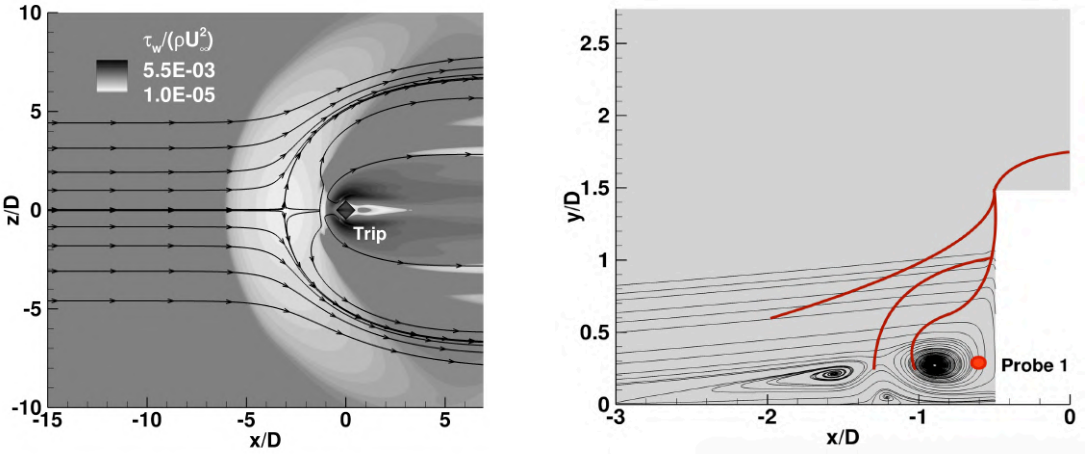

(a) (b)

Figure 3.13: (a) The mean streamwise wall shear contours around the trip (top view) and (b) the mean upstream recirculation region at $z/D = 0$ using the mean velocity streamtraces. Red lines without arrows show the time-averaged shock system in this plane. A red dot indicates Probe 1.

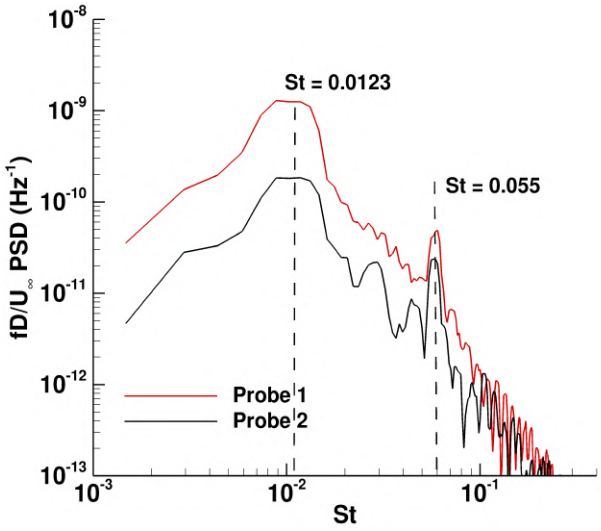

Figure 3.14: Premultiplied PSD of pressure at Probes 1 and 2.

3.4.1.2 Shock system

Second, we study the bow shock formed ahead of the trip as the top upstream portion of the trip is exposed to the supersonic flow. To understand the dynamics of the shock system, we plot the RMS of pressure and the mean turbulent kinetic energy on the symmetry plane near the trip as shown in Figures 3.15(a,b). In Figure 3.15(a), we observe the high RMS pressure at the bow shock, which indicates that the shock is unsteady. This observation is consistent with the mean turbulent kinetic energy contours as shown in Figure 3.15(b). The unsteadiness of the bow shock is caused by the interaction between the bow shock and the upstream vortices via shocks (see Figure 3.13b). PSD analysis of pressure at Probe 2 (see Figure 3.15a) behind the bow shock quantifies its unsteadiness in terms of frequency. As shown in Figure 3.14, we observe the peak-amplitude frequency at $St = 0.0123$ and a local peak frequency at $St = 0.055$. Thus, the shock system is unsteady similar to the upstream vortex system. However, the dominant source of instability observed downstream of the trip is still unclear. Therefore, let us study downstream regions of the trip to obtain more insights into the instability mechanism.

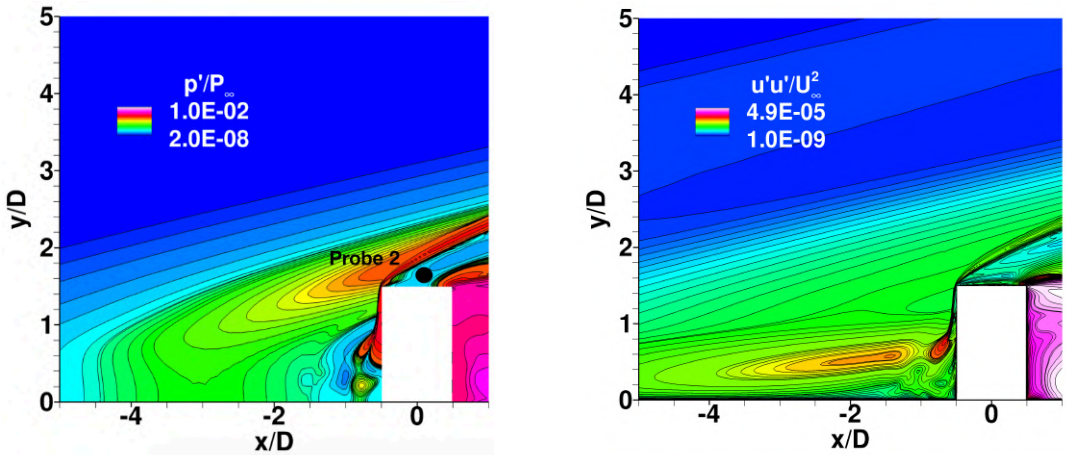

(a) (b)

Figure 3.15: (a) RMS of pressure and (b) the mean turbulent kinetic energy on the symmetry plane $z/D = 0$. Probe 2 (black dot) is located behind the bow shock.

3.4.1.3 Shear layers/counter-rotating streamwise vortices

In this subsection, we study the unsteadiness downstream of the trip using PSD analysis of pressure at Probes 3, 4, and 5 (Figure 3.16a). At these probe locations, the fluctuations of the Q-criterion isosurfaces (Figure 3.12) start to appear. In Figure 3.16(b), we observe peak-amplitude frequencies at $St = 0.055$ and 0.11 at all downstream probes. These critical frequencies can originate from the upstream vortex system, the unsteady shock system, or the downstream region of the trip. Therefore, we perform a freezing operation, that is we hold the flow state fixed during the simulation in a region of interest, and simulate the remainder of the flow domain for 10 flow times. In the present study, we freeze the upstream vortex system and the shock system ($x/D < 0$), and repeat the PSD analysis at the downstream probe locations. Thus, there is no unsteady forcing of the downstream flow by the upstream region. We still observe peak-amplitude frequencies at $St = 0.055$ and 0.11 after the freezing operation. This finding indicates that the sources of unsteadiness observed downstream of the trip are the flow structures which originate from the downstream portion of the trip ($x/D > 0$). Because the upstream flow is frozen, it cannot cause the observed unsteadiness. Therefore, the local peak frequency at $St = 0.055$ observed in the upstream vortex system and the shock system (see Figure 3.14) is due to the pressure disturbances propagating upstream from the source through the subsonic region.

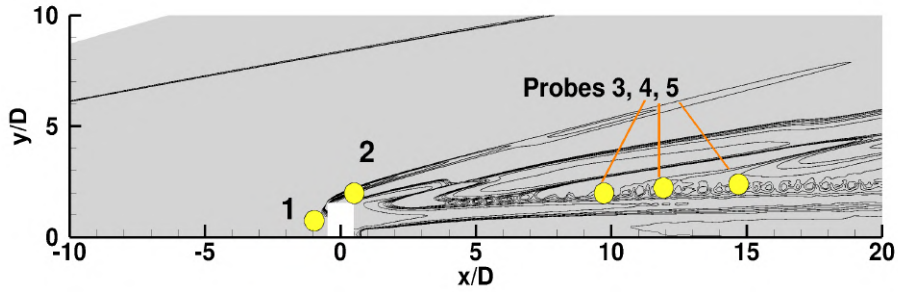

(a)

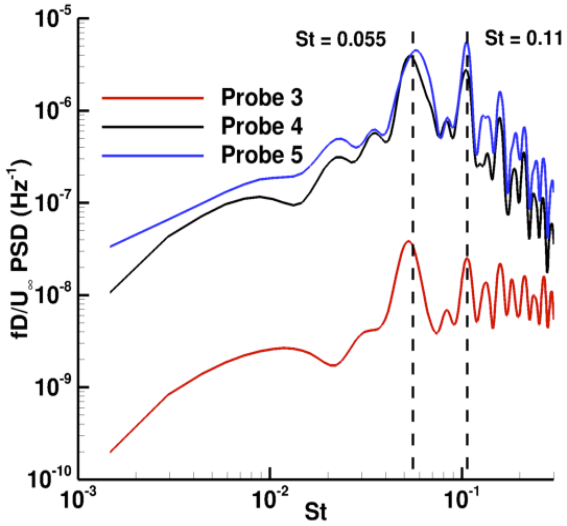

(b)

Figure 3.16: (a) Probe locations are shown around the isolated trip on the symmetry plane. Contour lines are of instantaneous pressure. (b) Premultiplied PSD of pressure at Probes 3, 4, and 5.

Figure 3.17 presents the flow structures downstream of the trip such as the mean horseshoe vortices, the mean CVP, and the mean shear layers on a streamwise plane at x/D = 10. The mean streamwise vorticity colors the streamwise plane. Contours of the mean streamwise vorticity show the CVP near the symmetry plane ($z/D = 0$) and the horseshoe vortices away from the symmetry plane. Contour lines on the plane indicate local shear values (U_s) that represent the mean local shear layers.

$$U_s = \sqrt{\left(\frac{\partial u}{\partial y}\right)^2 + \left(\frac{\partial u}{\partial z}\right)^2} \tag{3.10}$$

We observe that the shear layers envelop the CVP and the horseshoe vortices downstream. Directions of each of the CVP vortices are upwash as shown by the contours of mean streamwise vorticity. Therefore, the CVP lifts away from the wall (Brandt 2014).

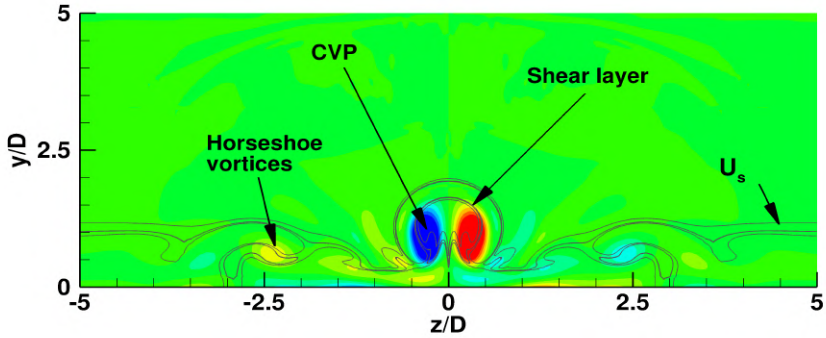

Figure 3.17: Contours of the mean streamwise vorticity showing the orientation of the mean counter-rotating streamwise (CVP) and the mean horseshoe vortices behind the isolated diamond-shaped trip at $x/D = 10$. The mean shear layers are shown using U_s contour lines.

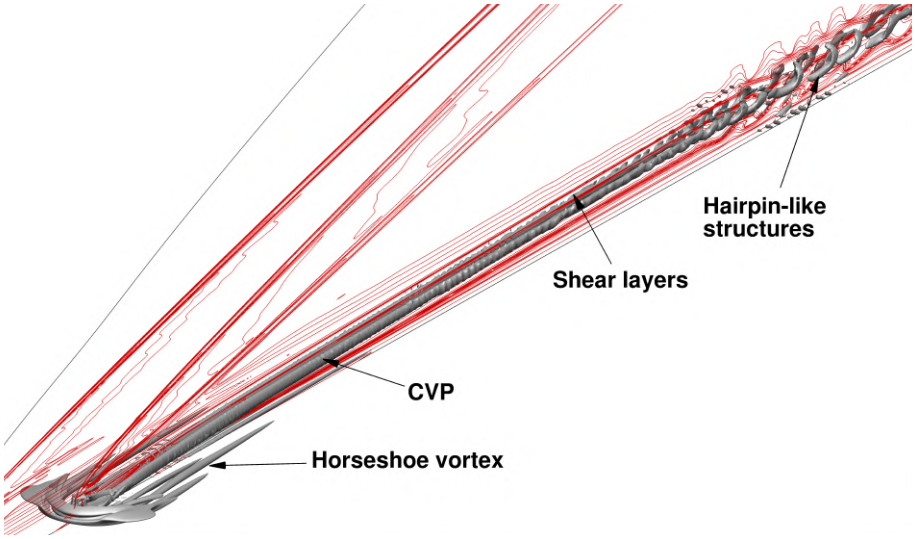

Figure 3.18: Shear layers (contour lines by U_s to show local shear values) from the top of the trip interacting with the CVP (Q-criterion isosurfaces colored by streamwise velocity) on the symmetry plane. Both flow structures are instantaneous.

In Figure 3.18, interactions between instantaneous shear layers (contour lines of local shear values on the symmetry plane) from the top edge and corners of the trip, and the instantaneous CVP (Q-criterion isosurfaces) are shown. We observe that the shear layers, as well as the CVP, fluctuate spatially when they interact with each other downstream of the trip. The lift-up mechanism of the CVP amplifies the interaction. Due to the interaction, the upper part of the CVP advects faster than its lower part. Thus, the CVP stretches streamwise to form hairpin-like structures. These structures, which get stretched further downstream, destabilize the shear layers. Therefore, the combined system of the shear layers and the CVP finally break down to turbulent flow. This finding indicates that the source of instability in the current trip configuration is a coupled system of the shear layers and the CVP. Furthermore, Figure 3.19 shows contours of the root mean square (RMS) of pressure and the mean turbulent kinetic energy on a streamwise plane at $x/D = 10$. We observe that the dominant prominence of these quantities are in the area where the shear layers and the CVP interact. No such strong perturbations are found in the horseshoe vortices at the same streamwise location. Similar findings are also observed at other streamwise locations. Therefore, these results are consistent with the previous analysis.

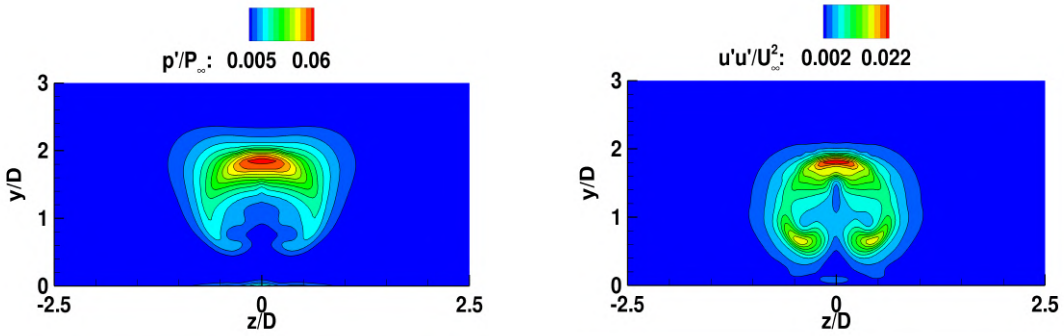

(a) (b)

Figure 3.19: (a) The RMS of pressure and (b) the mean turbulent kinetic energy on the streamwise plane at $x/D = 10$.

3.4.1.4 Three-dimensional dynamic mode decomposition

Now let us find globally dominant modes using DMD and analyze their mode shapes. DMD is a post-processing technique that utilizes a number of snapshots either from experiments or simulations to extract a set of modes, each of which has a fixed oscillation frequency and

decay/growth rate. A snapshot means a realization of a flow variable within a domain of consideration at a time instant. DMD extracts eigenvalues and eigenmodes using a linear mapping from the n^{th} snapshot to the $(n+1)^{th}$ snapshot. Proper orthogonal decomposition (POD) is a similar method. POD extracts modes that have broadband frequency content, whereas each DMD mode has its own frequency. However, DMD modes are nonorthogonal, unlike POD modes. Therefore, this lack of orthogonality of DMD modes makes it challenging to systematically select a group of modes that is the strongest representation of the flow dynamics. Jovanović, Schmid, and Nichols (2014) addressed this problem by developing a sparsity promoting variant of the standard DMD algorithm. Sparsity-promoting dynamic mode decomposition (SPDMD) achieves a balance between the quality of approximation and the number of DMD modes. The adjustment is carried out using the least-squares deviation (between the matrix of snapshots and the linear combination of selected DMD modes) with a supplementary term that penalizes the l_1-norm of the vector of DMD amplitudes. For more information on SPDMD, readers are referred to Jovanović et al. (2014).

In the present study, the snapshot domain is three-dimensional because a volumetric snapshot provides more detailed and accurate dynamics of the flow which is complex. In DMD, snapshots of data are formed as columns into a matrix ψ (of size $M \times N$, say). M and N are total degrees of freedom and number of snapshots respectively. For the selection of the dominant modes, we use the Chu disturbance energy norm (Chu 1965). For more information, readers are also referred to Hanifi (1996) and Nichols et al. (2017). In short, this norm H (defined by 3.11) incorporates all the flow quantities to select the most energetic DMD mode from a given snapshot matrix representing flow dynamics of interest.

$$H = \int_V \left\{ \frac{1}{2}\rho_o(u'^2 + v'^2 + w'^2) + \frac{1}{2}\frac{c_o^2\rho'^2}{\gamma\rho_o} + \frac{1}{2}\frac{\rho_o c_v T'^2}{T_o} \right\} dV \tag{3.11}$$

In (3.11), "X_o" and "X'" are the time-averaged and fluctuating values of flow variable "X", respectively. Mode shapes of pressure associated with the selected DMD modes are used so as to be consistent with the PSD analysis performed earlier.

The region of snapshot considered in the present trip configuration ranges $x/D \in$ [-7, 20] across the span height. The region was selected because (1) no flow breakdown region is included (minimizes nonlinearity), (2) all modes of transition can be studied, and (3) the number of degrees of freedom is smaller (compared to the entire domain). The sampling period is 5.0 μsec, and the number of snapshots is 100 in the present study. Since the

dominant frequencies observed in the previous PSD analysis are at $St = 0.055$ and 0.11, and the present Nyquist frequency is at $St = 0.37$, the sampling frequency is sufficient to capture the relevant high-frequency modes. $M = 40$ million cells and $N = 100$ snapshots. Since the ψ matrix is tall (M) and skinny (N), the TSQR algorithm (Sayadi and Schmid 2016) is implemented to carry out parallel QR factorizations. The algorithm is very efficient and scalable for the present case.

3.4.1.4.1 ***DMD results***

We obtain two dominant DMD modes at $St = 0.055$ and $St = 0.11$ based on the Chu disturbance energy norm. Frequencies of these DMD modes are consistent with the previous PSD analysis. To quantify the contribution of each DMD mode to the flow dynamics, we calculate their respective performance loss. The performance loss due to a set of selected DMD modes is the deviation between the actual snapshot matrix ψ and a reconstructed matrix formed by the linear combination of the selected DMD modes. Based on the performance loss, mode 1 ($St = 0.055$) and mode 2 ($St = 0.11$) contain approximately 27% and 7% of the total energy of the flow dynamics respectively. In Figure 3.20(a), pressure perturbations of mode 1 are plotted on the symmetry plane. Mode 2 has similar mode shapes, and therefore, is not shown here. We observe that perturbations appear to originate from the downstream region of the trip. This finding is also consistent with the previous analysis, in which the sources of the unsteadiness are the shear layers and the CVP. Moreover, Figure 3.20(b) indicates that mode 1 is varicose-type instability in which the maximum interaction occurs between the wall-normal shear layers and the CVP.

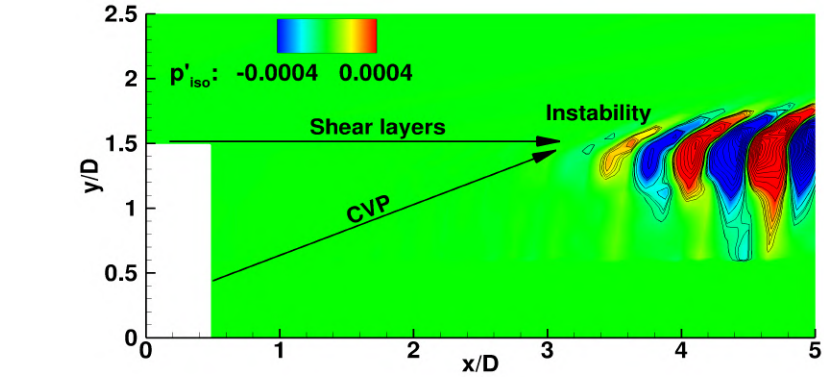

(a)

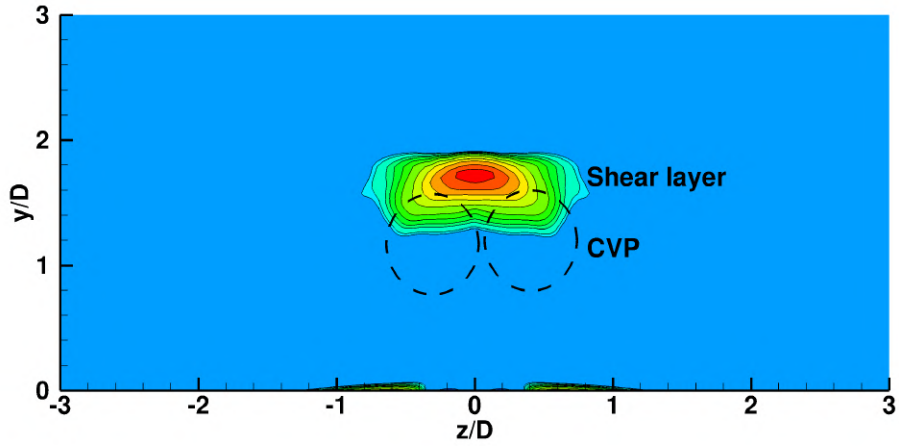

(b)

Figure 3.20: Mode shapes of mode 1 ($St = 0.055$) on (a) the symmetry plane and (b) the streamwise plane ($x/D = 10$) using pressure contours.

3.4.1.5 Comparison to the isolated cylindrical trip

In this subsection, we compare the instability mechanisms of the isolated cylindrical and diamond-shaped trip flows. In the case of the isolated cylindrical trip, the source is the upstream vortex system, while that of the isolated diamond-shaped trip is a coupled system of the shear layers and the CVP from its downstream region. A reason behind this difference is the trip shape. Since the cylindrical trip is blunter compared to the diamond-shaped trip, the cylindrical trip has a larger stand-off distance between the bow shock and its stagnation point, and therefore, additional upstream vortices. However, in the diamond-shaped trip, due to the sharper upstream trip surface, there are higher pressure gradients across

its side edges, which lead to the formation of the shear layers being more unstable than the upstream vortex system. Hence, the downstream flow structures become the dominant source of instability in the isolated diamond-shaped trip. Furthermore, in the DMD analysis of the isolated diamond-shaped trip, we observe that the pressure perturbations are significantly more prominent in the downstream region than in the upstream vortex and the shock systems. However, in the isolated cylindrical trip, the dominant DMD modes show strong presence of unsteadiness of the shock system that causes instabilities downstream. Therefore, the trip shape plays a significant role in the instability mechanism and flow unsteadiness around the trip.

3.4.2 Trip array

This subsection discusses and characterizes unsteadiness induced by the trip array as shown in Figure 3.21. Q-criterion isosurfaces show the rotational motion of the two pairs of counter-rotating streamwise vortex pairs per trip. The two CVP pairs lie on top of each other, and therefore, are named as CVP-L and CVP-U pairs ("L" for the lower pair near the wall, and "U" for the upper pair away from the wall). These pairs (the CVP-L pair is formed due to the wrapping of the upstream vortex system and the CVP-U pair, similar to the CVP discussed earlier in the isolated diamond-shaped trip, originates from the wake of the trip) are clearly shown in Figure 3.21. To understand the instability mechanism in the present trip configuration, we discuss flow structures in the region downstream of the trip array similar to the isolated diamond-shaped trip. The upstream vortex system, the shock system, and the formation of the CVP-U vortices associated with the trip array are discussed briefly in Appendix B.

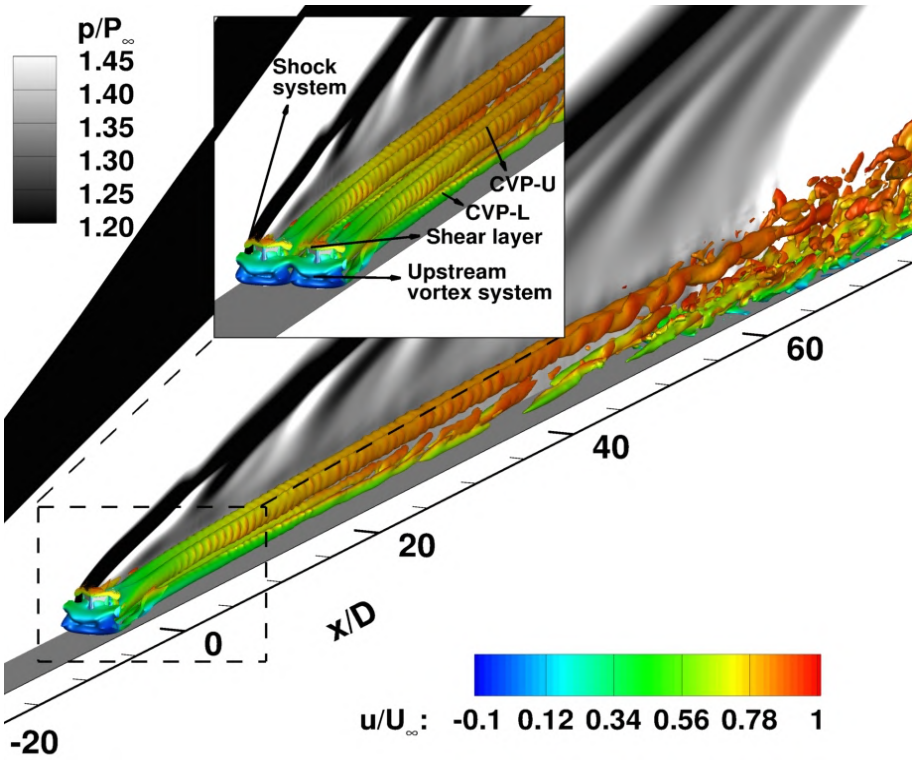

Figure 3.21: Q-criterion ($=2.5\times10^8$) isosurfaces colored by the nondimensionalized streamwise velocity upstream and downstream of the trip array. A spanwise plane on the left side shows instantaneous pressure contours.

3.4.2.1 Shear layers/counter-rotating vortex system

First, PSD analysis at Probes 3, 4, and 5 is shown in Figure 3.22(a). We observe peak-amplitude frequencies at $St = 0.11$, 0.22, and 0.33. To investigate the source of these peak-amplitude frequencies, we perform a freezing operation (similar to the isolated diamond-shaped trip) in the upstream vortex system and the shock system, and carry-out PSD analysis at the downstream probes. We still observe the same peak-amplitude frequencies. This finding indicates that the source of these peak-amplitude frequencies is the region downstream of the trip array (consistent with the isolated diamond-shaped trip). Therefore, let us now study flow structures originating from the downstream region of the trip array to understand more about the instability mechanism.

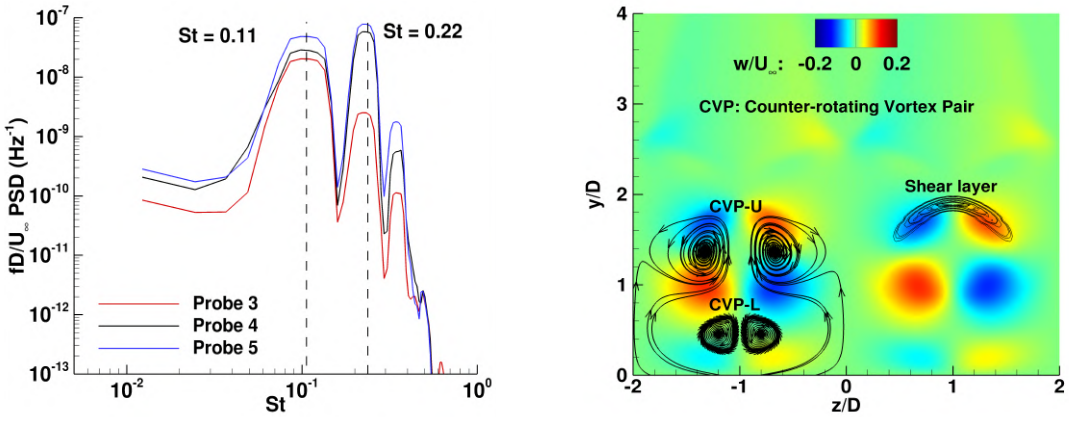

(a) (b)

Figure 3.22: (a) Pre-multiplied PSD of pressure at the downstream probes 3, 4, and 5. (b) Orientation of the mean counter-rotating streamwise vortex pairs (CVP) and the mean three-dimensional shear layers surrounding the CVP at $x/D = 10$. Trip centers are at z/D = -1 and 1.

Figure 3.22(b) shows a detailed positioning of both mean CVP pairs along with the mean shear layers at $x/D = 10$. It is interesting to note that the mean CVP-L is closer to the symmetry plane in the trip array than the mean horseshoe vortices due to the isolated diamond-shaped trip. We observe the CVP-U has upwash fluid movement, while the CVP-L has downwash fluid movement. Since the rotational motion of the CVP-U is greater than that of the CVP-L (see Figure 3.21), the net fluid movement is away from the wall. Furthermore, the CVP-U is enveloped by the shear layers. This net upward movement of the CVP-U leads to more interaction between the shear layers and the CVP-U further downstream. Figure 3.23 shows that the interactions between the shear layers and the CVP-U lead to the formation of hairpin-like structures similar to the isolated diamond-shaped trip. These hairpin-like structures, which get further stretched due to the interactions, destabilize the shear layers. Finally, the hairpin-like structures and the shear layers break down to turbulent flow. Therefore, the source of instability remains a coupled system of the shear layers and the CVP-U.

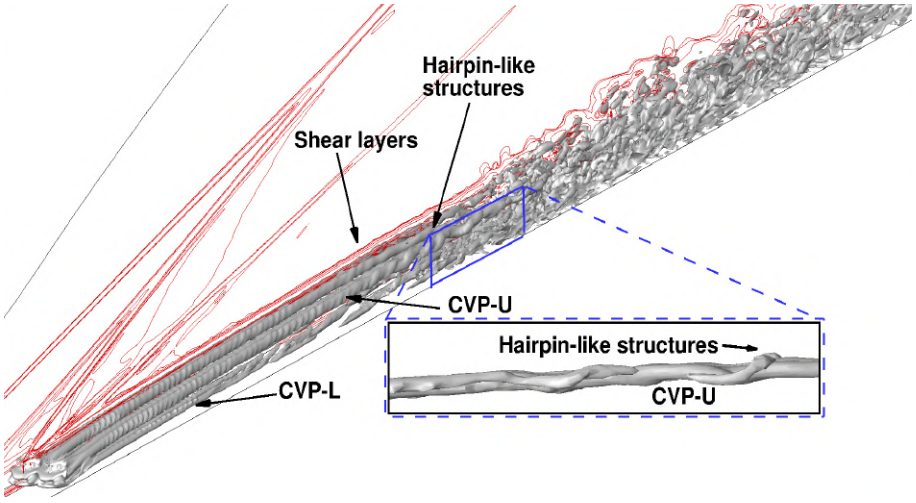

Figure 3.23: Shear layers (contour lines by U_s to show local shear values) from the top of the trips interacting with the CVP-U (Q-criterion isosurfaces colored by streamwise velocity) on the symmetry plane. Both flow structures are instantaneous.

Furthermore, Figure 3.24 shows strong unsteadiness around the interaction between the CVP-U and the shear layers using the RMS of pressure on a streamwise plane at $x/D = 10$. This finding is also consistent with the previous PSD analysis.

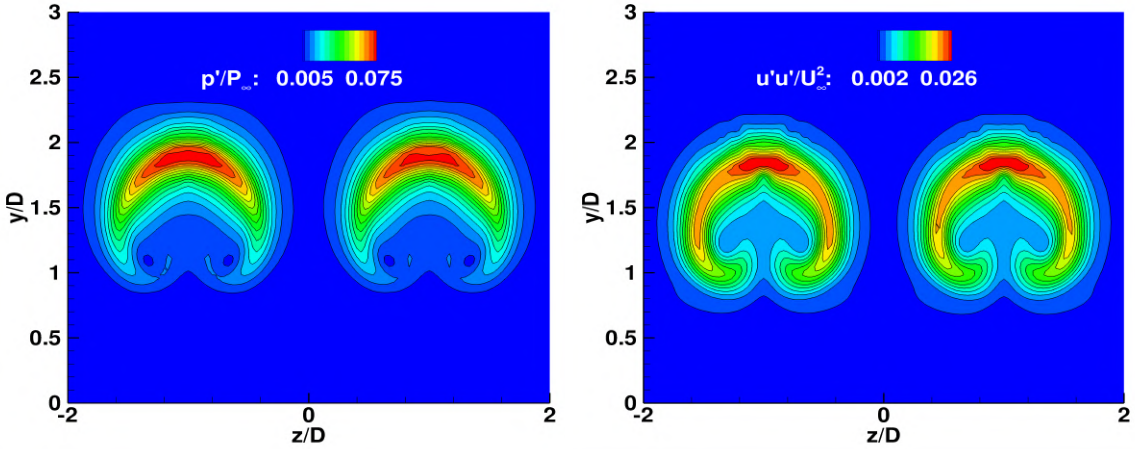

(a) (b)

Figure 3.24: (a) The RMS of pressure and (b) the mean turbulent kinetic energy on the streamwise plane at $x/D = 10$.

Similar to the isolated diamond trip, let us now globally find the dominant frequencies, and study their modal shapes and overall contribution to the flow dynamics around the trip array using three-dimensional DMD and the Chu disturbance norm in the next subsection.

3.4.2.2 Three-dimensional dynamic mode decomposition

Similar to the isolated diamond-shaped trip, let us now find the globally dominant frequencies, and study their mode shapes and overall contribution to the flow dynamics around the trip array using three-dimensional DMD and the Chu disturbance norm. A region of snapshot ranges as $x/D \in$ [-20, 20] across the span height. The sampling period is 5 μsec, and the number of snapshots is 100. $M = 40$ million cells and $N = 100$ snapshots.

3.4.2.2.1 *DMD results*

We obtain two dominant DMD modes at $St = 0.11$ (mode 1) and $St = 0.22$ (mode 2) based on the Chu disturbance energy norm (shown by 3.11). These DMD modes are consistent with the previous PSD analysis. To quantify contribution of each DMD mode to flow dynamics, we calculate their respective performance loss. Based on performance loss, mode 1 and mode 2 carry 48% and 15% of the total energy of flow dynamics respectively. Therefore, mode 1 is the dominant mode which causes instability downstream. The corresponding DMD amplitude and eigenvalue spectra are shown in Figure 3.25(a) and (b) respectively. Performance loss and sparsity-promotion spectra are shown in Figure 3.26(a) and (b) respectively.

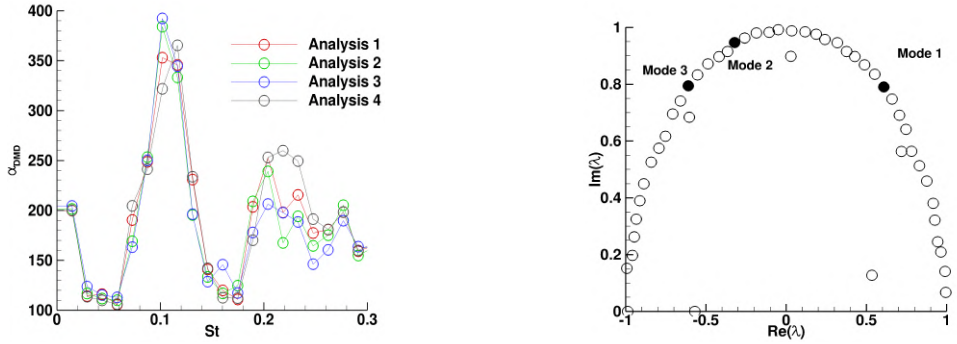

(a) (b)

Figure 3.25: (a) DMD amplitudes vs. Strouhal number at different initial snapshots (termed as "Analysis") and (b) eigenvalue spectrum.

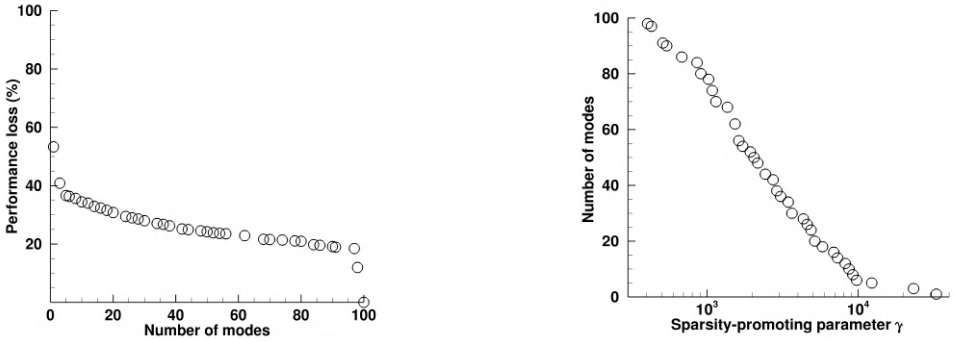

(a) (b)

Figure 3.26: (a) Performance loss vs. number of modes retained and (b) number of modes retained vs. γ values.

Let us now discuss mode shapes of mode 1 (mode 2 is similar) as shown in Figure 3.27(a) on the symmetry plane ($z/D = 1$). We observe that the shear layers from the top sides of the trip and the counter-rotating streamwise vortex pair from its wake interact to cause instability downstream of the trip array. This finding indicates that the source of instability in the current trip configuration is similar to the isolated diamond-shaped trip. The dominant instability is consistently the varicose type as shown by Figure 3.27(b). The PSD analysis carried out earlier agrees with the modal analysis.

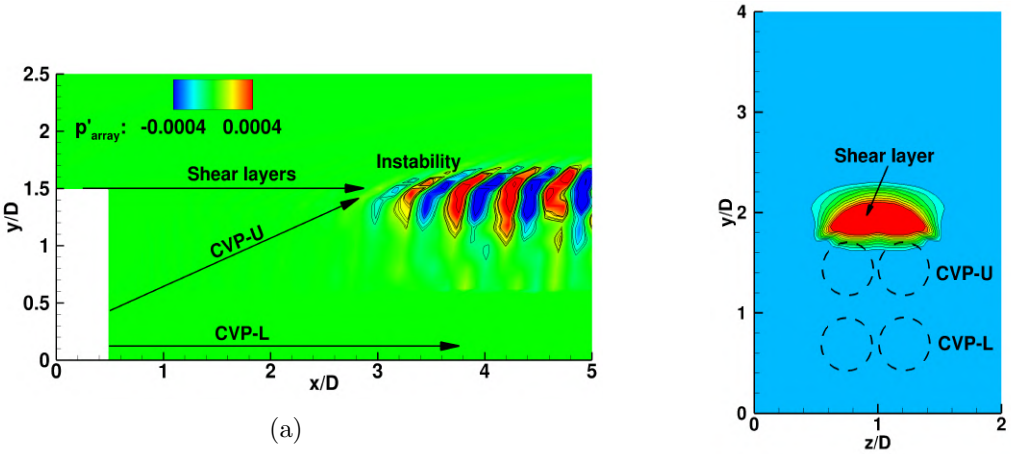

(a) (b)

Figure 3.27: Mode shapes of mode 1 ($St = 0.11$) on (a) the symmetry plane and (b) the streamwise plane ($x/D = 10$) using pressure contours.

3.4.2.2.2 Spatial power spectral analysis

In this section, we use another method to select the mode with the highest growth rate along the streamwise direction. For this purpose, spatial evolution of the normalized PSD of pressure at different frequencies with respect to the streamwise distance at $z/D = 1$ is shown in Figure 3.28(a) for the trip-array configuration. Amplitudes at different frequencies are averaged over different wall normal distances (less than $y/D = 3$) on the plane $z/D = 1$. From Figure 3.28(a), one can observe the PSD of different frequencies are different upstream of the trip. It could be due to the selective excitement of the frequency modes due to the interaction between the shear layers and the CVP-U. Furthermore, PSD of all the frequencies increases exponentially past the roughness element. In a logarithmic scale, their rates of increment are almost linear. However, specific frequencies ($St = 0.11$ and 0.22) appear to be dominant (based on PSD) as the streamwise distance increases.

Let us consider an expression for spatial evolution of the PSD of a given frequency f as 6.2.

$$PSD(x, f) = exp(\alpha(f)x) \tag{3.12}$$

To select the dominant frequency or frequencies, we use a norm as shown in 3.13.

$$Norm(f) = \int_0^L PSD(x, f)exp(-\alpha(f)x)\, dx \tag{3.13}$$

L in 3.13 is only up to $x/D = 10$ to analyze the spatial evolution within the region of exponential growth of all the frequencies. Here, $\alpha(f)$ indicates a constant spatial growth rate of each frequency. The value of $\alpha(f)$ is determined using the least square method between the PSD values (PSD(x,f)) and exp($\alpha(f)$x). The value of $\alpha(f)$ is computed using 3.14.

$$\alpha(f) = \frac{\sum_1^N log(PSD(x, f))}{\sum_1^N x} \tag{3.14}$$

where, N is the total number of points selected at different streamwise distances. Based on the value of $Norm$, peaks at St = 0.11 (30 kHz) and 0.22 (60 kHz) appear in figure 3.28(b). This observation suggests that the dominant frequencies selected agree well with the SPDMD and previous PSD analysis.

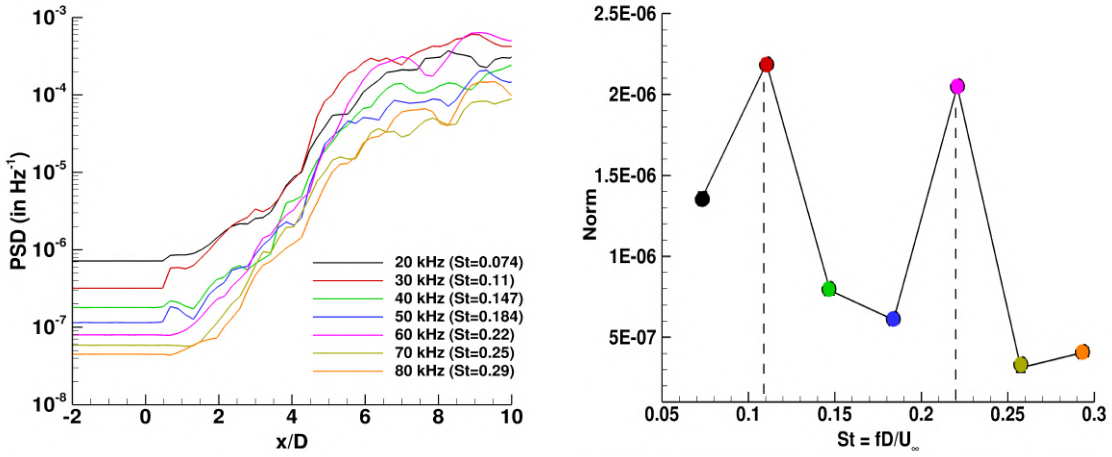

(a) (b)

Figure 3.28: (a) Streamwise evolution of PSD of pressure at $z/D = 1$ and $y/D = 1.33$, and (b) variation of the selected norm with respec to dominant frequencies.

3.4.2.3 Comparison to the isolated diamond-shaped trip

In this subsection, we compare the instability mechanisms of the isolated diamond-shaped trip and the trip array flows. The source of instability is observed to be consistent in both configurations. Therefore, the trip spacing does not alter the source of instability. However, we found two differences regarding dominant frequencies (the most unstable mode) and instability onset locations. Instability onset location is the downstream location at which the shear layers and the CVP-U (the trip array) or the CVP (the isolated diamond-shaped trip) begin to fully interact with each other. The difference in the instability onset locations is around $1D$ as shown in Figure 3.29 using RMS of pressure contours. This difference is small because the effect of neighboring counter-rotating streamwise vortices from the wake of the trip array is minimal just downstream of the trips. However, the streamwise growth of instabilities in the trip array is higher than the isolated diamond-shaped trip as flow breaks down much earlier in the trip array. This finding is due to a combined effect of the CVP-U from the wake of neighboring trips and the CVP-L from the upstream vortex system in the trip array. Dominant frequencies are at $St = 0.055$ in the case of the isolated trip and $St = 0.11$ in the case of the trip array. This disparity in the dominant frequencies can be due to the difference in spanwise spacing available for the CVP (isolated diamond-shaped trip: more spacing and lower frequency) or the CVP-U (trip array: less spacing

and higher frequency) as these downstream flow structures force the shear layers to become unstable. In Figure 3.30, we observe that the flow becomes transitional earlier in the trip array configuration based on the streamwise evolution of the mean skin-friction coefficient (C_f defined by 3.15).

$$C_f = \tau_{wall}/(\rho_\infty U_\infty^2) \tag{3.15}$$

In 3.15, τ_w is the mean wall-shear stress. This finding indicates that the trip array configuration is more effective in tripping the incoming laminar boundary layer, and therefore, this tripping arrangement is used in high-speed vehicles like scramjets, where turbulent flows ahead of their combustion engines are desirable.

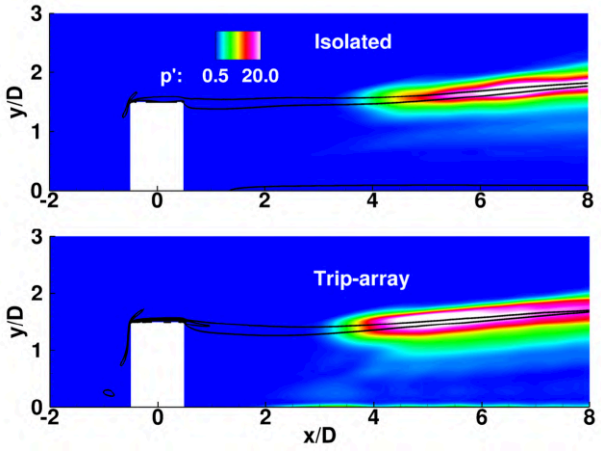

Figure 3.29: Comparison of the instability onset locations in the isolated diamond-shaped trip and the trip array using RMS of pressure at $z/D = 1$. Black contour lines indicate local shear values, U_s, to show the mean shear layers from the top edges of the trip.

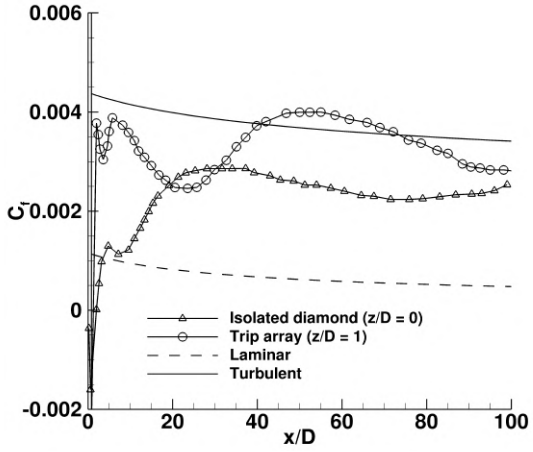

Figure 3.30: Comparison of the mean skin-friction coefficient along the streamwise direction in the isolated diamond and the trip array configurations.

Chapter 4

Parametric Study: Passive Trips

In this chapter, we perform parametric studies of instability due to both trip configurations. As discussed earlier in the chapter 1, to optimally design a scramjet (for example), it is desirable to predict the transition-onset before its combustion chamber at a wide spectrum of flight conditions. However, this prediction is a very complex problem, as many factors alter the transition-onset such as edge Mach number, freestream Reynolds number (by altering freestream density), roughness (shape, height, and alignment), and freestream disturbances. For brevity, in the present study, we particularly focus on four parameters: (1) freestream Reynolds number, (2) roughness height, (3) intermediate trip spacing, and (4) roughness shape in the trip array.

4.1 Effects of freestream Reynolds number

One of the parameters which can alter flowfields is freestream Reynolds number. Wheaton and Schneider (2012) investigated the effects of freestream Reynolds number on flow unsteadiness of isolated cylinder trip flows as shown in Figure 4.1. They found that altering freestream Reynolds number led two interesting observations regarding instability frequency. First, there was no change in the instability frequency (instability-1 in Figure 4.1) associated with the upstream vortex system. Second, the instability frequency (instability-2 in Figure 4.1), which was related to separated shear layers and a counter-rotating vortex pair from the wake of the trip, changed with the freestream Reynolds number. A higher freestream Reynolds number led to a higher frequency (instability-2) of instabilities due

to the shear layers and the counter-rotating vortex pair. Hence, are these findings similar in the current diamond-shaped trip configurations? To vary freestream Reynolds number ($Re_\infty = \rho_\infty U_\infty k/\mu_\infty$), freestream density is altered in the present study. Here, a higher Reynolds number (Re_∞ = 72,000: 3× $Re_{\infty 0}$) case is considered. $Re_{\infty 0}$ is the base or previous freestream Reynolds number = 24,000, and it is based on U_∞, k, and freestream kinematic viscosity (ν_∞). We compare high-Re_∞ findings with the baseline trip configurations (low-Re_∞) as discussed earlier.

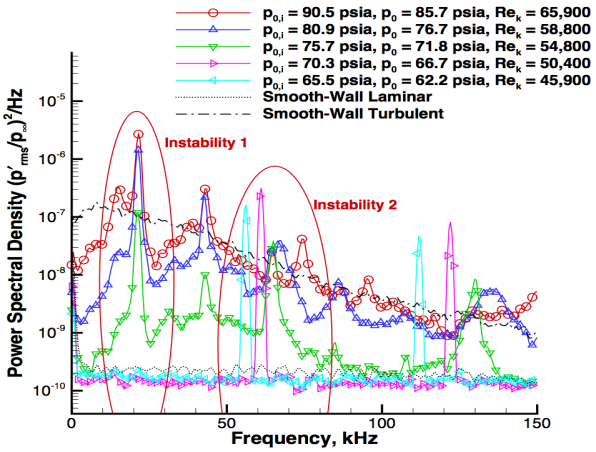

Figure 4.1: Effects of Reynolds number on the near-effective cylindrical roughness element at Mach 6. Reproduced from Wheaton and Schneider (2012)

4.1.1 Trip array

A similar three-dimensional domain, that contains two diamond-shaped trips and larger mesh size, is used to carry out the current investigation. The grid-converged size of the domain is approximately 120 million cells. The domain extends up to $50D$ downstream of the trip center. We obtain a statistically stationary solution after 30 flow through times.

In Figure 4.2(a), we observe one mean upstream vortex similar to the baseline configuration. However, the mean upstream extension of the upstream vortex system increases to $\approx 10D$ (increased by 30%). It is because k/δ increases from 1.48 to 1.8 (δ decreases with higher Re_∞), and therefore, a larger recirculation region is formed. In Figure 4.2(b), we observe higher pressure perturbations across the separated shock and near the stagnation region of the trip in the higher Re_∞ case as expected.

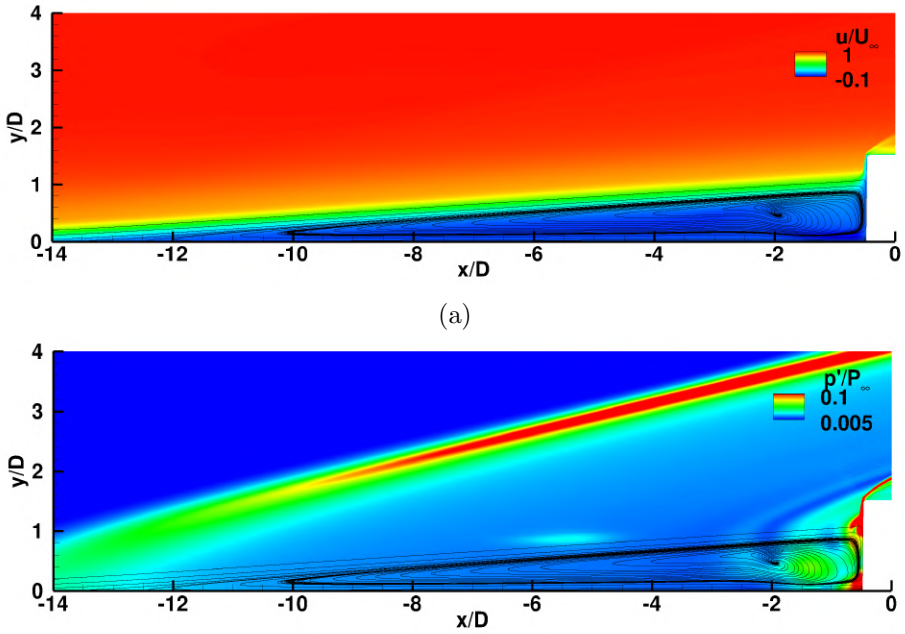

Figure 4.2: (a) The mean upstream vortex and (b) the shock systems on a plane ($z/D = 1$) in the trip-array configuration.

Comparison of the wall-normal mean turbulent kinetic energy profiles at different streamwise stations is shown in Figure 4.3. We observe that a higher Reynolds-number flow leads to higher mean turbulent kinetic energy. Similar trends were also found using RMS of pressure.

Q-criterion isosurfaces colored by instantaneous streamwise velocity show breakdown processes downstream of the trip array as in Figure 4.4. We observe hairpin-like structures that later become unstable and breakdown to turbulent flows.

The PSD analysis of pressure indicates that the peak-amplitude frequency is at higher frequencies (St=0.26) with higher amplitudes as shown in Figure 4.5. To find the source of instability observed downstream of the trip array, we carry-out another freezing operation for 10 flow through times. As shown in Figure 4.5, we obtain the same frequency at Probe 3. This finding indicates that the source of instability in the current higher Re_∞ case is consistently the coupled system of the shear layers and the counter-rotating vortex pair.

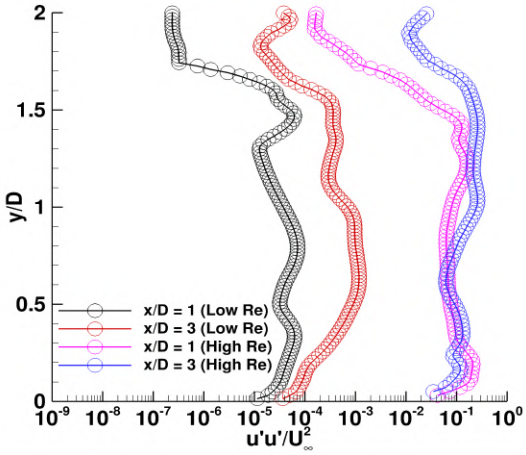

Figure 4.3: The wall-normal mean turbulent kinetic energy profiles at different streamwise stations in high and low Reynolds-number cases in the trip array.

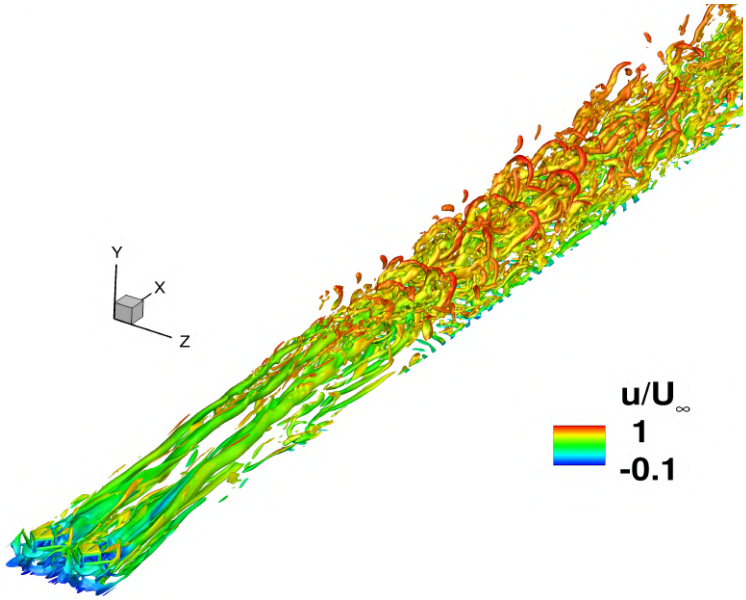

Figure 4.4: Q-criterion isosurfaces colored by streamwise velocity around the trip array at the higher Re_∞ case.

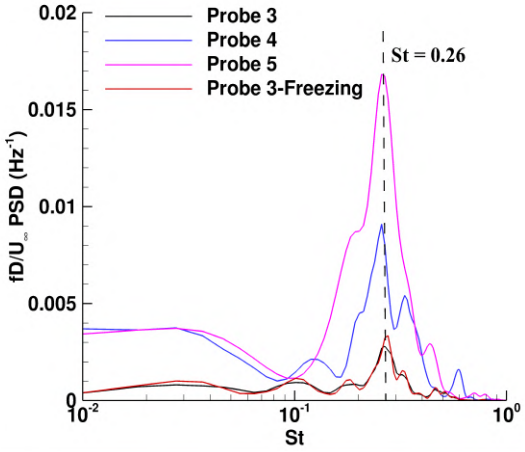

Figure 4.5: Premultiplied PSD of pressure at Probes 3, 4 and 5 downstream of the trip-array configuration.

4.1.2 Isolated trip configuration

Another three-dimensional domain, that contains an isolated diamond-shaped trip, is used to carry out simulations at the higher Re_∞. The grid-converged size of the domain is also approximately 120 million cells in this case. The domain extends up to 50 D downstream of the trip center. We obtain a statistically stationary solution after 30 flow times.

In Figure 4.6, the mean upstream vortex and shock systems are observed. Figure 4.6(a) shows the mean vortices ahead of the trip. It is interesting to note that the number of the mean upstream vortices is three, and consistently, the same as the lower Re_∞ case.

Similar to the trip-array configuration, Figure 4.7 shows that wall-normal profiles of the mean turbulent kinetic energy at different streamwise stations increase with the higher Re_∞ as expected.

Figure 4.26 shows Q-criterion isosurfaces colored by streamwise velocity upstream and downstream of the isolated trip.

In Figure 4.9, we observe that PSD of pressure at Probes 3, 4 and 5 is consistently peak at $St = 0.12$. To find the source of instabilities observed downstream of the isolated trip configuration as shown in Figure 4.26, we carry-out additional freezing operation ahead of the center of the trip. After the freezing procedure, we still find the same peak-amplitude frequency at Probe 3.

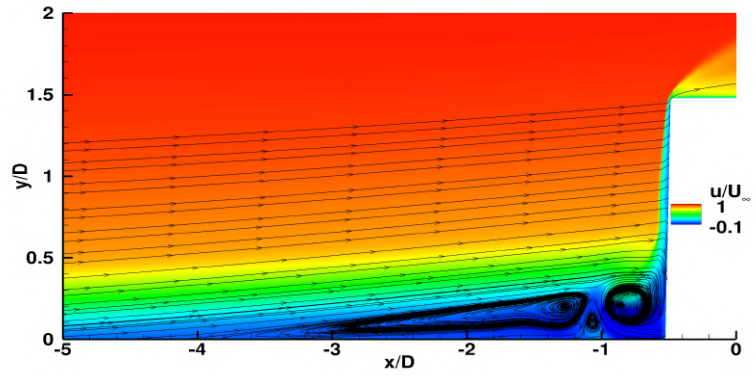

(a)

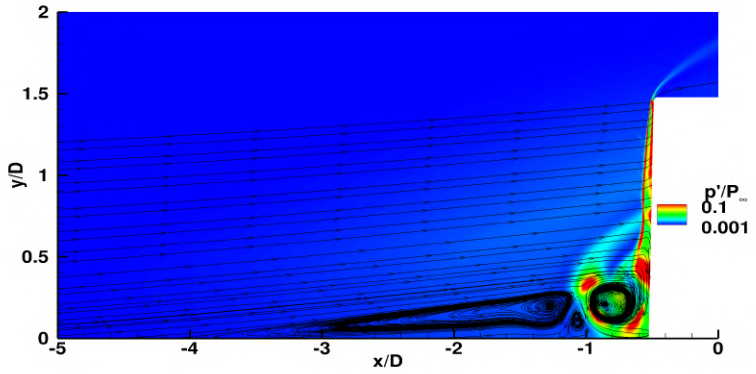

(b)

Figure 4.6: (a) The mean upstream vortex and (b) shock systems ahead of the isolated trip configuration at higher Re_k.

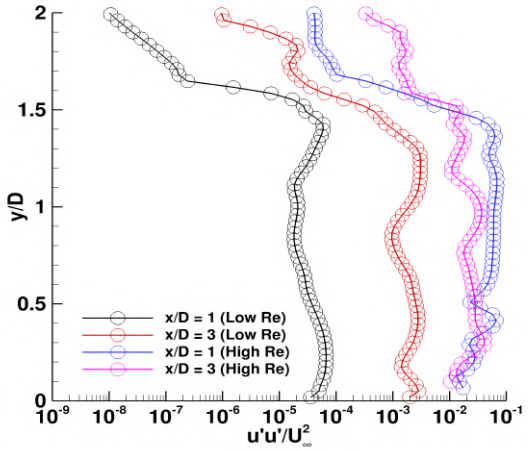

Figure 4.7: Wall-normal turbulent kinetic energy evolution along streamwise in high and low Reynolds number cases in the trip array.

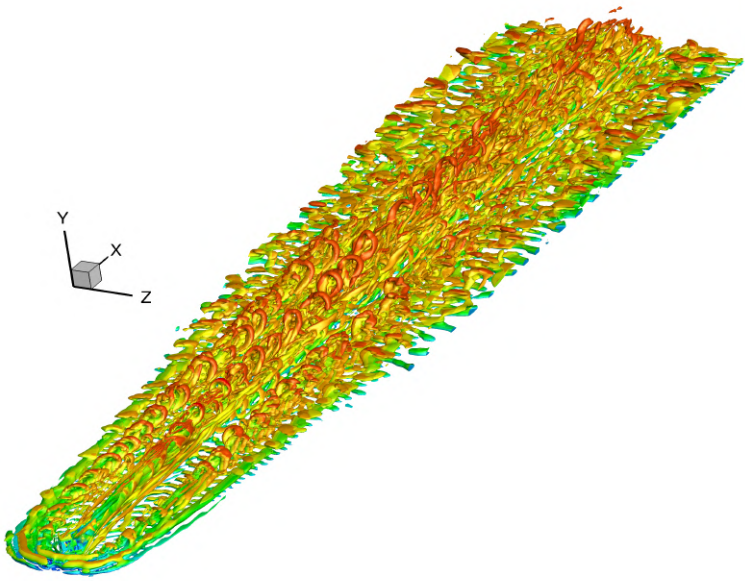

Figure 4.8: Q-criterion isosurfaces colored by streamwise velocity around the isolated diamond trip at high Re_∞.

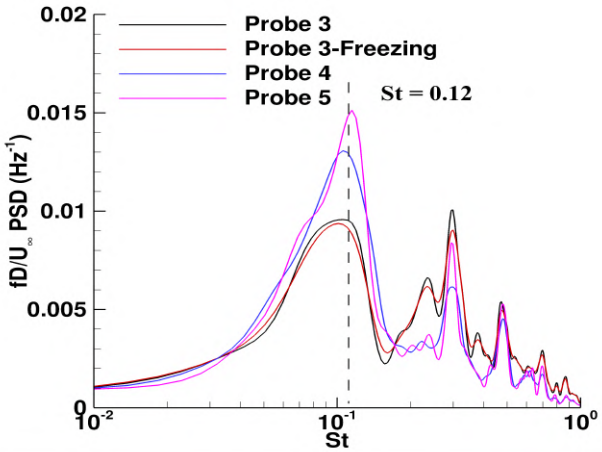

Figure 4.9: Premultiplied PSD of pressure at Probes 3, 4 and 5 downstream of the isolated trip configuration.

4.2 Effects of trip height

In this section, we discuss the effects of trip heights on the flow unsteadiness. Wheaton and Schneider (2014) investigated the effects of trip height on unsteadiness upstream of an

isolated cylindrical trip. Specifically, they performed measurements of unstable frequencies and transition-onset locations in the wake of isolated cylindrical trips at near-critical trip heights. A critical trip height at a given flight condition is the trip height which is sufficient to induce transition upstream of the smooth-wall transition-onset location. Minor modifications in the experimental parameters were observed to have a significant effect on the transition-onset location due to the trip with the near-critical trip heights. Likewise, a trip height is considered to be effective when a transition-onset location does not move upstream with an increasing trip height.

Wheaton et al. 2011 found that the decrement of the trip heights of the isolated cylindrical trip led to the disappearance of the frequency associated with the dominant instability mechanism (the upstream vortex system). Interestingly, the frequency associated with the second dominant mode of instability (the shear layers from the top edges and the counter-rotating vortex pair from the wake) lowers down along with its corresponding amplitude as the trip height is reduced. The finding is shown in Figure 4.10.

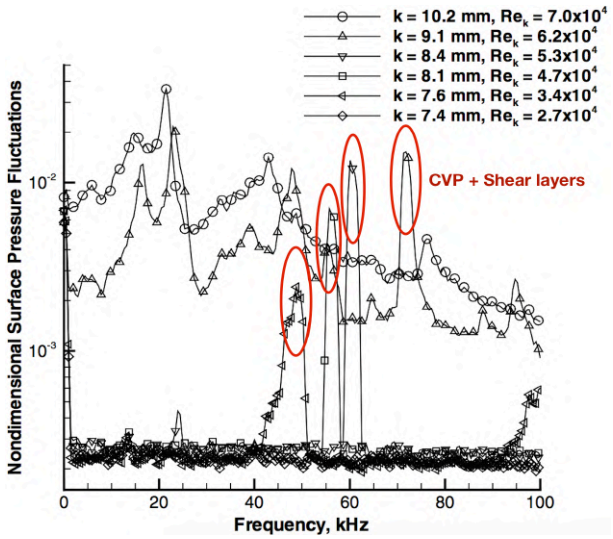

Figure 4.10: Effects of trip height of an isolated cylindrical trip at Mach 6. Reproduced and modifed from Wheaton et al. (2014).

In the present study, we consider four main cases: k/δ =1.3 (>1), $k/\delta = 1$, and $k/\delta =$ 0.8 and 0.7 (< 1). A schematic of the variation of the trip heights is shown in Figure 4.11.

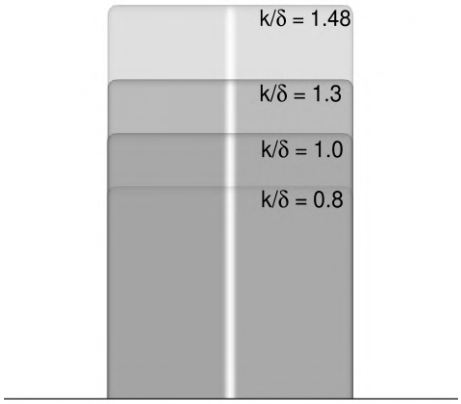

Figure 4.11: A schematic of the variation of the trip heights.

Let us first study a case at $k/\delta = 0.8$, and later investigate the effects of all the different trip heights on the instability mechanism. Based on the previous chapter, we expect that the mechanism in the isolated and trip-array configurations to be similar at different trip heights. Therefore, for the present study, we only study the effects on the trip-array configuration to maintain brevity and conciseness.

4.2.1 $k/\delta = 0.8$

In this case, the roughness height (k) is smaller than the untripped boundary layer thickness (δ). The converged mesh size of the domain containing two trips is around 110 million cells.

In Figure 4.12(a), the RMS contours of pressure are plotted on a plane ($z/D = 1$) with streamtraces of the mean velocities. The streamtraces indicate the presence of a single vortex system in the mean sense. This finding is similar to the baseline trip-array configuration. Second, the RMS contours show dominant prominence of pressure fluctuations near the bow shock, which is formed ahead of the trip array.

In Figure 4.12(b), contours of the mean spanwise velocity are plotted on a streamwise plane at $x/D = 3$. Black streamtraces indicates the mean velocity and red streamtraces show the mean local shear values (U_s). The mean velocity contour lines indicate the presence of the CVP-U and the CVP-L pairs, and the mean local shear contour lines show the presence of the mean shear layers emanating from the top of the trip array. It is observed (not shown) that the rotational motion of the CVP-L is weaker compared to that of the CVP-U. This finding indicates that the source of instability may be the coupled system of the shear

layers and the CVP-U similar to the baseline k/δ configuration.

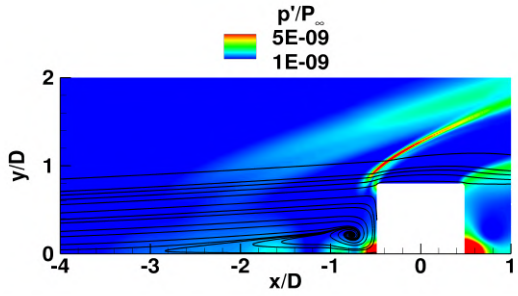

(a)

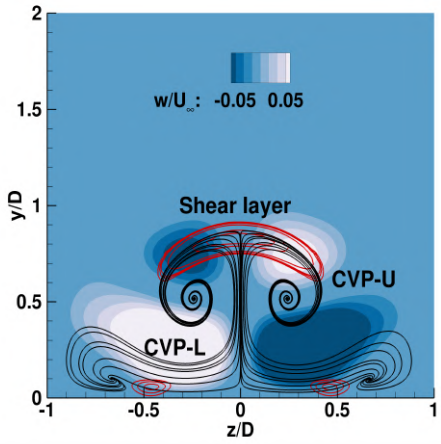

(b)

Figure 4.12: (a) The RMS contours of pressure and the streamtraces of the mean velocity ahead of the trip array whose $k/\delta = 0.8$. (b) Contours of the mean spanwise velocity superimposed by red contour lines of the mean local shear values (U_s) at $x/D = 3$. Black contour lines are streamtraces of the mean velocity.

In the upper image of Figure 4.13(a), we plot the streamwise evolution of the mean turbulent kinetic energy along the region of interaction between the shear layers and the CVP-U. It is observed that the evolution is linear with respect to the streamwise distance up to $x/D = 30$. Besides, the lower image of Figure 4.13(b) also shows the prominence of the mean turbulent kinetic energy in the region of the interaction. Furthermore, at Probe 1 ($x/D = 30$, $y/D = 1.8$, $z/D = 0$), pre-multiplied PSD of spanwise velocity and turbulent kinetic energy is plotted in Figure 4.13(b) to compute the peak-amplitude frequency associated with instability downstream of the trip array. The peak-amplitude frequency is found

to be $St = 0.08$. To confirm the source of instability as the coupled system, we perform a freezing operation ahead of the center of the trip ($x/D < 0$) up to 20 flow through times. We still obtain the same peak-amplitude frequency (St) at 0.08, and this finding confirms the source of instability to be the coupled system similar to the baseline trip-array configuration. Therefore, we observe that the source of instability does not change even if k/δ is reduced to 0.8. The instability mechanism in the other trip-height cases was also observed to be the same as $k/\delta = 0.8$.

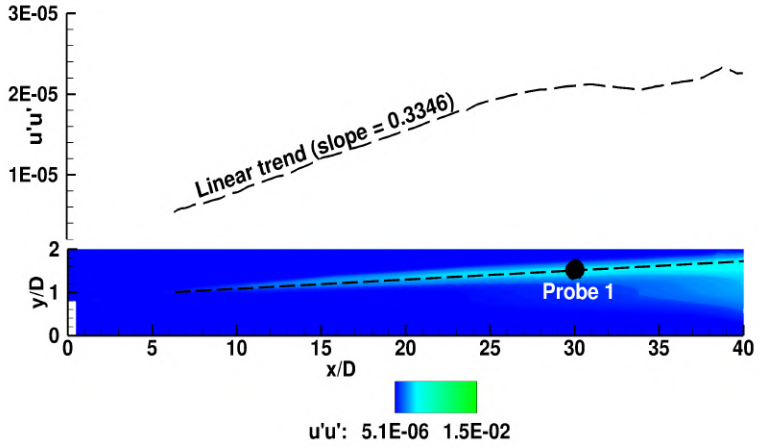

(a)

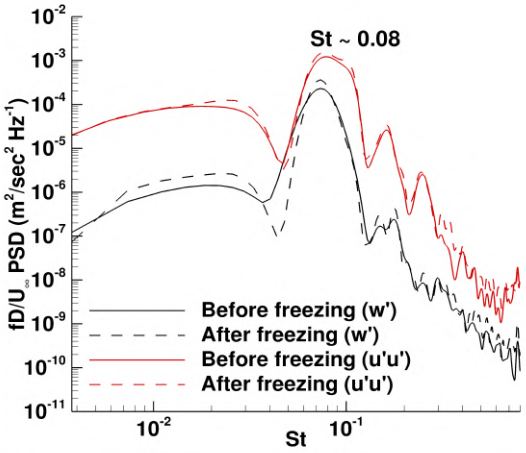

(b)

Figure 4.13: (a) The mean turbulent kinetic energy contours on the symmetry plane ($z/D = 0$) along with a linear trend of the kinetic energy along the region, where the shear layers and the CVP-U interact. (b) PSD of spanwise and kinetic energy fluctuations at the Probe 1 ($x/D = 30$, $y/D = 1.8$, $z/D = 0$).

4.2.2 Dynamic mode decomposition

To obtain the globally dominant mode in the present case $k/\delta = 0.8$, we carry-out dynamic mode decomposition in the vicinity of the trip array. The snapshot domain extends from x/D = [-10, 50] across the span. The total degrees of freedom is 21 million cells per trip. The snapshot frequency is 200 kHz, and the number of snapshots taken is 125. The Nyquist frequency of 100 kHz ($St = 0.37$) is sufficient to capture the dominant mode oscillating at the peak-amplitude frequency. Since the ψ matrix is tall (M) and skinny (N), the TSQR algorithm (Sayadi and Schmid 2016) is implemented to carry out parallel QR factorizations.

In Figure 4.14, mode shapes of the dominant mode 1 (spanwise velocity fluctuations at $St = 0.08$) is colored on the symmetry plane. Three dynamical flow structures emanating from the trip array are shown: the shear layers, the CVP-U, and the CVP-L. Since it is confirmed that the source of instability is due to the shear layers and the CVP-U, we observe strong prominence of mode 1 in the region where these two flow structures interact most. The shear layers are observed to stretch the CVP-U streamwise. This stretching of the CVP-U causes the formation of hairpin-like structures that later breaks down to turbulent flow similar to the baseline trip-array configuration.

These findings indicate that the DMD mode captured is consistent with the PSD analysis carried out earlier, and this mode dominantly causes instability downstream of the trip array. In the following subsection, we discuss the overall effect of different trip heights on the instability mechanism.

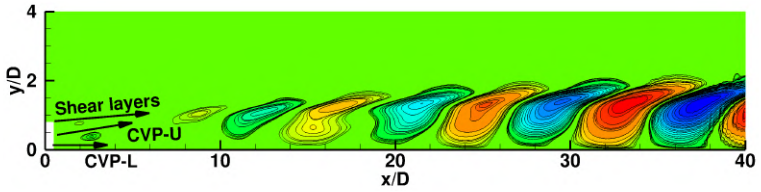

Figure 4.14: Mode shapes of the dominant mode 1 at $St = 0.08$ in the $k/\delta = 0.8$ case. Contours are of spanwise velocity fluctuations.

4.2.3 Overall effects

The overall effects of the trip height in the present study is centered around (1) the mean upstream recirculation extension, (2) the associated peak-amplitude frequency, (3) the maximum kinetic energy at a fixed location (here, we choose $x/D = 10$), and (4) the mean

instability-onset location.

4.2.3.1 Mean upstream recirculation extension

The mean upstream recirculation extension is measured on the symmetry plane of a trip as it is almost same across the span. In Figure 4.15(a), we observe that the variation of the mean upstream recirculation extension is linear with respect to the trip height (k/δ). We also find that as the k/δ lowers, the mean upstream recirculation extension reduces. This finding is due to lesser blockage created by trips with lower k/δ.

4.2.3.2 The mean instability-onset location

In Figure 4.15(b), we observe that an increment in k/δ values leads to a decrement of the mean instability-onset location. This finding indicates that the instability-onset can be moved ahead or delayed based on the trip height used. It is interesting to note that the nature of the relationship between k/δ and the mean instability-onset location is also linear. A possible reason is that the flow behavior is linear (or weakly non-linear) up to the mean instability-onset location at all the k/δ cases.

4.2.3.3 The maximum kinetic energy

Figure 4.15(c) shows the variation of the maximum mean turbulent kinetic energy on a streamwise plane at $x/D = 10$ (similar at $x/D = 20$ and 30) with respect to k/δ. The variation is non-linear and asymptotic in nature. The maximum kinetic energy is highest when $k/\delta = 1.48$, while it is lowest when $k/\delta = 0.7$. The reason is that when k/δ is higher, the higher-speed shear layer and counter-rotating vortex pair interact to cause stronger velocity perturbations downstream of the trip array.

4.2.3.4 Peak-amplitude frequency

The PSD analysis of pressure was also performed using different trip heights at their respective mean instability-onset locations (see Figure 4.15b). It is observed that the peak-amplitude frequency is found to be altered based on the k/δ value selected. At a higher k/δ trip height, the peak-amplitude frequency is observed to be higher, and at a lower k/δ trip height, the peak-amplitude frequency reduces. This finding is consistent with Wheaton et al. (2014). This decrement of the peak-amplitude frequency when the trip height is reduced

indicates that the earlier instability-onset (due to a taller trip) is associated with a higher peak-amplitude frequency.

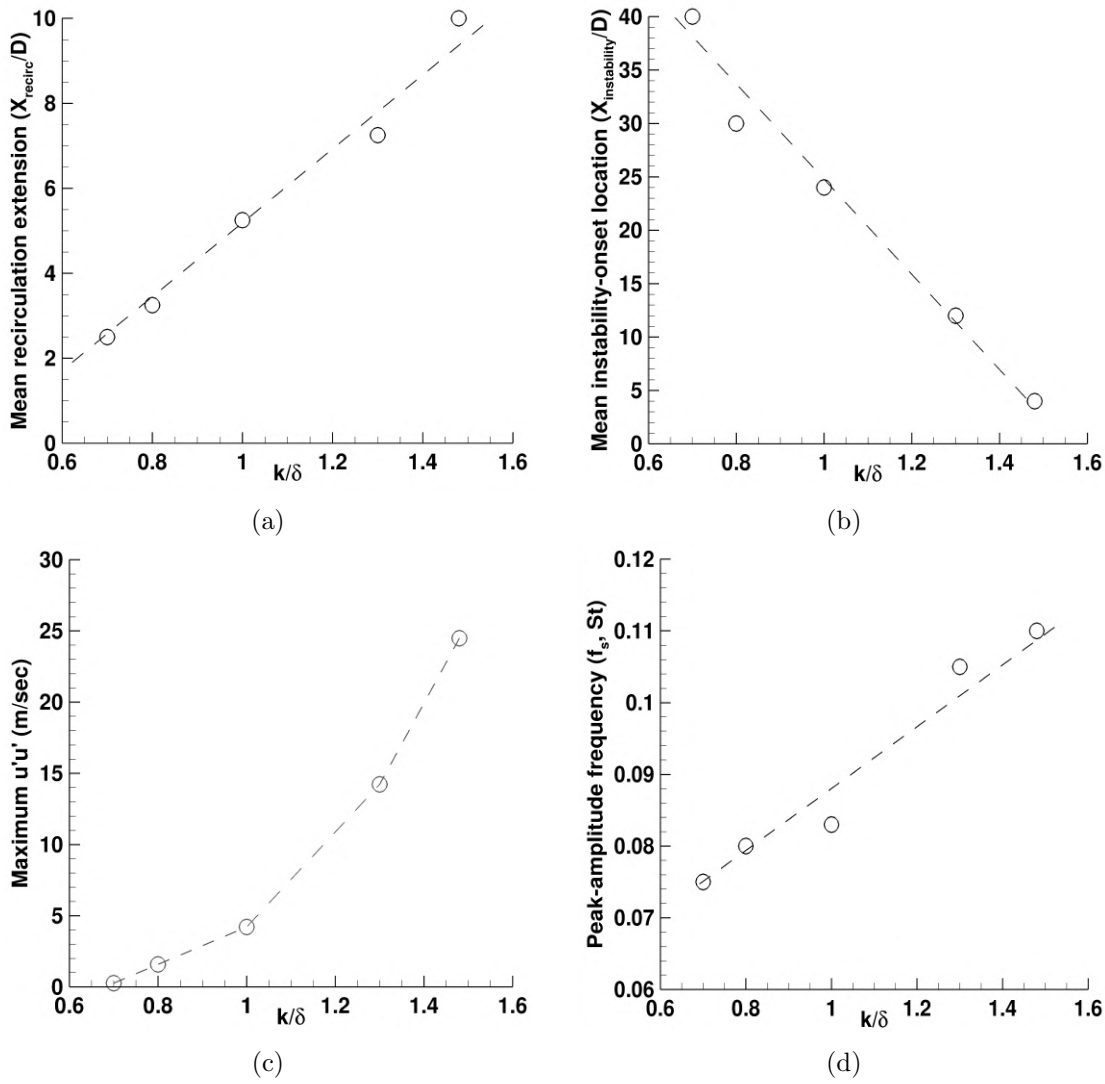

Figure 4.15: Effects of trip height on (a) the mean upstream recirculation extension, (b) the mean instability-onset location, (c) the maximum mean turbulent kinetic energy on a streamwise plane at $x/D = 10$, and (d) the peak-amplitude frequency associated with the instability.

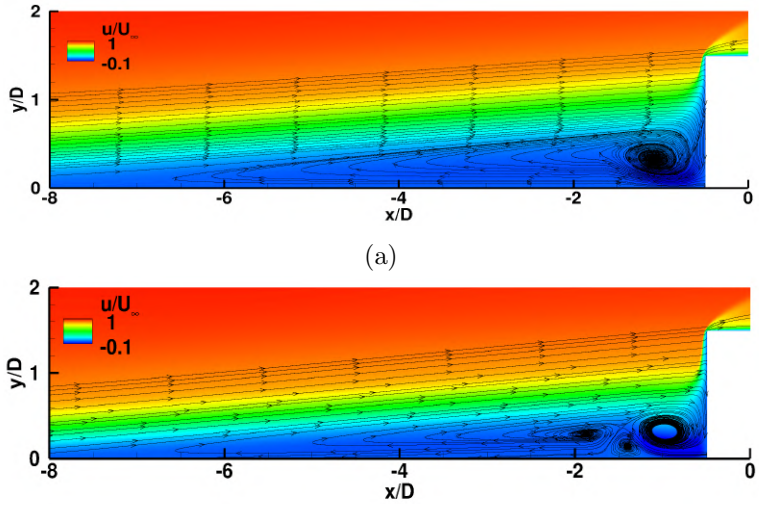

(a)

(b)

Figure 4.16: The mean upstream vortex system ahead of a diamond-shaped trip using (a) s/D = 3 and (b) s/D = 4 trip configurations.

4.3 Effects of intermediate trip spacing

In this section, we discuss the effects of intermediate trip spacing between the isolated diamond-shaped trip ($s/D = \infty$) and the trip array ($s/D = 2$). We mainly focus on the critical spacing ($s/D_{critical}$) after which the CVP-U and CVP-L are not on top of each other, and each trip of the array becomes an isolated diamond-shaped trip. Figures 4.16(a) and 4.16(b) show the mean upstream vortex system on the plane ($z/D = 1$) for trip configurations with s/D=3 and s/D=4 respectively. We observe that the number of the mean vortices increases from 1 to 3 similar to the baseline isolated diamond trip configuration as s/D is increased from 3 to 4.

Similarly, Figures 4.17(a) and 4.17(b) show streamtraces of the mean velocity at x/D = 5 using $s/D = 3$ and $s/D = 4$ cases. This findings indicate the critical trip spacing ($s/D_{critical}$) lies in between 3 and 4 in the present study.

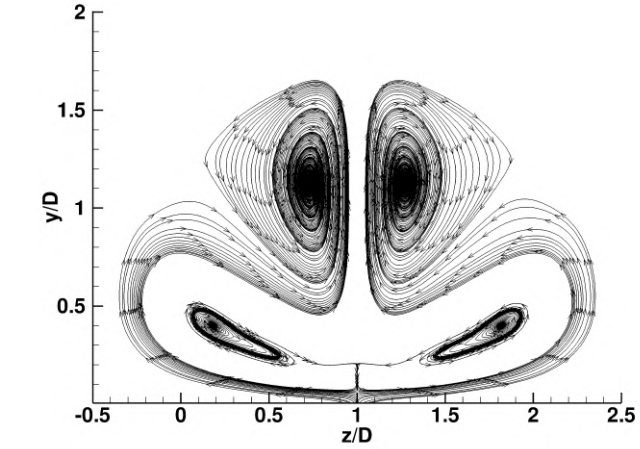

(a)

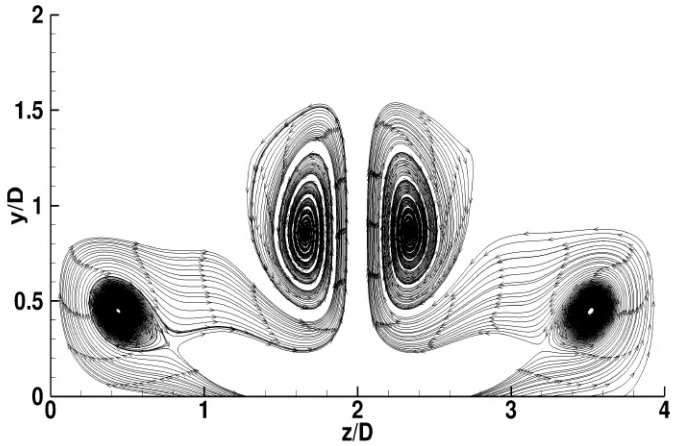

(b)

Figure 4.17: Streamtraces of the mean velocity on a streamwise plane at $x/D = 5$ with (a) s/D =3 and (b) $s/D = 4$.

4.4 Effects of trip shape: Array

In this section, we perform DNS simulations of an experimental campaign carried by Williams et al. (2018) in their hypersonic boundary layer facility (HyperBLAF) at Princeton University. In the experiment, an array of cylindrical trips was used to trip a Mach-7 laminar boundary layer. A reason to select another experimental data is to validate our simulations further and gain more confidence in our analysis. The primary objective is to qualitatively compare the flow unsteadiness due to an isolated cylindrical trip and the

trip array containing cylindrical trips. A schematic of the experimental setup is shown in Figure 4.18.

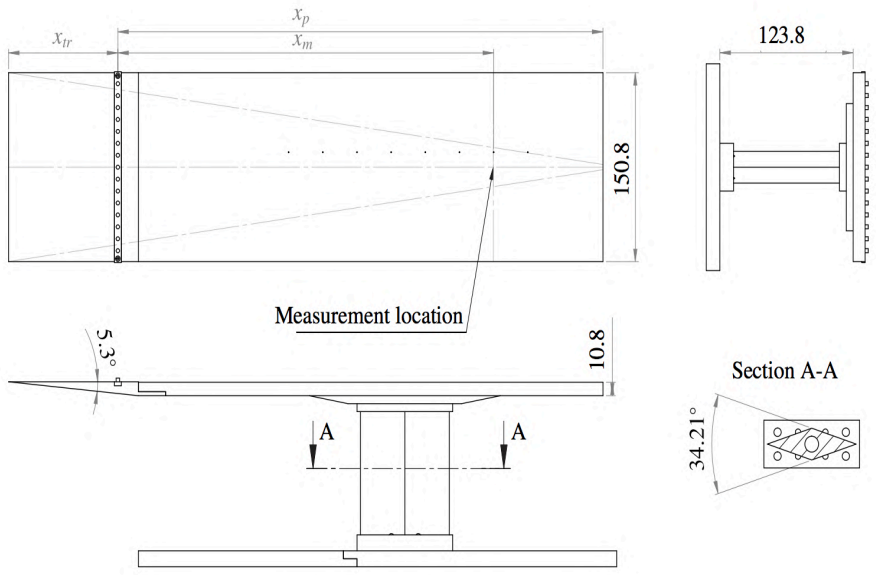

Figure 4.18: A schematic of the experimental setup. Reproduced from Williams et al. (2018). All dimensions are in mm.

4.4.1 Boundary conditions

Freestream conditions of the experimental campaign are shown in Table 4.1.

Table 4.1: Freestream conditions: HyperBLAF facility at Princeton University.

SN	Mach number (M_∞)	Temperature (T_∞)	Pressure (P_∞)	Unit Re_∞/m
1	8	48.6 K	1373 Pa	35×10^6/m

Trip height is 2.75 mm, spanwise trip-width (D) is 3.18 mm, and the untripped boundary layer thickness (δ_{99}) at the trip location (101.6 mm from the leading edge of the flat plate) is 1.72 mm. Therefore, $k/\delta = 1.6$, and is close to the k/δ (=1.48) considered earlier in the baseline configuration. $s/D = 3$ i.e. the center-center spacing between the two neigboring trips is $3\times D$.

A schematic of the boundary conditions to perform DNS simulations of this experiment

is shown in Figure 4.19. The inflow boundary condition is supersonic inflow (interpolated from a 2-D domain similar to the diamond-shaped trips), the spanwise boundary conditions are transitionally periodic, the thermal nature of the wall is isothermal (the thermal conductivity of the wall material (brass) used in the experiment is high, and the wall is pre-heated to 300K), and the outflow boundary is supersonic. The flat plate is at a zero angle of attack.

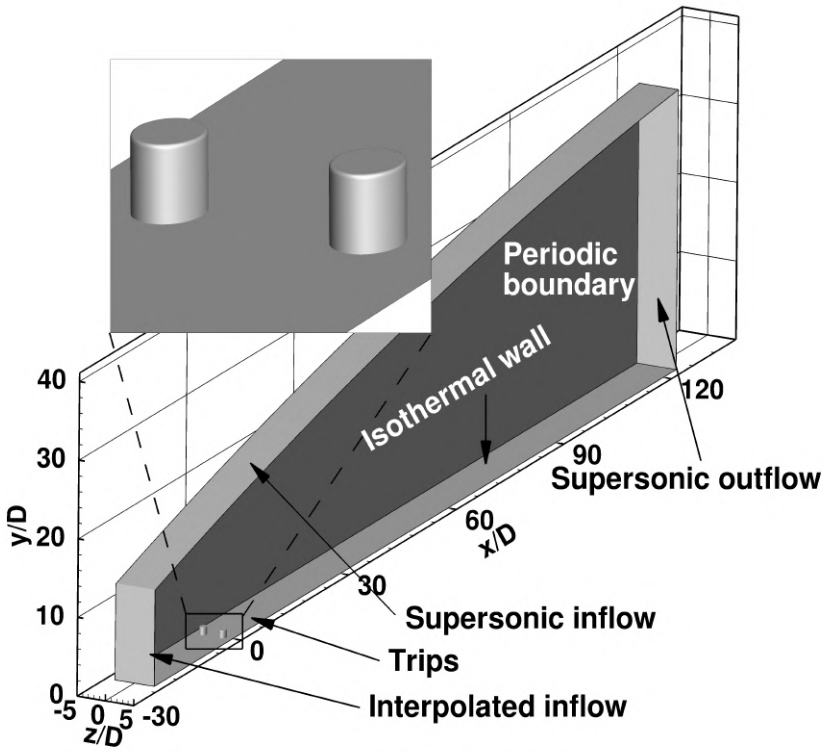

Figure 4.19: A schematic of the boundary conditions of the 3-D computational domain used to simulate the experiment.

4.4.2 Mesh generation

Three-dimensional meshes are generated using Link3D to simulate the experiment. Isometric and top views of the mesh generated in the vicinity of a cylindrical trip used in the experiment are shown in Figures 4.20. The converged mesh size is approximately 120 million cells. The near-wall spacing unit (y^+) is 0.1. The computational time step is temporally converged to 10 nanoseconds in this current case. The HyperBLAF facility is a blowdown

wind tunnel. However, to study the instability mechanism only due to the trip array and the lack of data related to the characterization of the freestream disturbances, we do not incorporate any freestream disturbance.

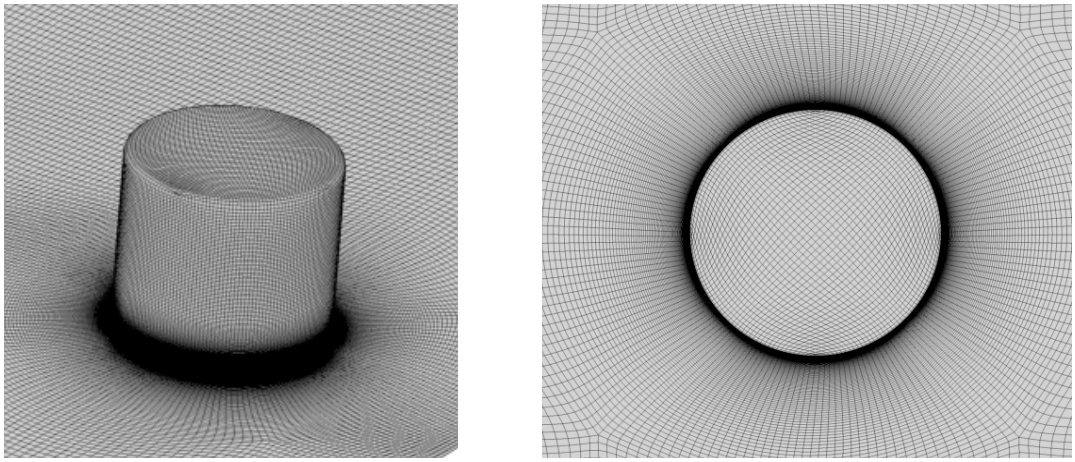

(a) (b)

Figure 4.20: (a) Isometric and (b) top views of the mesh generated near one cylindrical trip.

4.4.3 Comparison with the experiment

Let us first carry-out validation of the present numerical simulations with the experiment. This validation will provide more confidence in our simulations. We compare the mean van Driest velocity profile, and the RMS values of streamwise and wall-normal velocities with respect to the wall-normal distance in Figures 4.21(a), (b) and (c) respectively. In Figure 4.21(a), we observe that there is substantial agreement between our simulation and the experiment. However, Figures 4.21(b) and (c) indicate that the experiment and our simulation are not in a good agreement in the region close to the wall especially in case of the mean streamwise velocity. A reason could be that our simulation has no freestream disturbances, while the experiment has these disturbances. Therefore, higher fluctuations of velocities are expected in the experiment, and therefore, the RMS values of both experimental velocity profiles are higher than the numerical data.

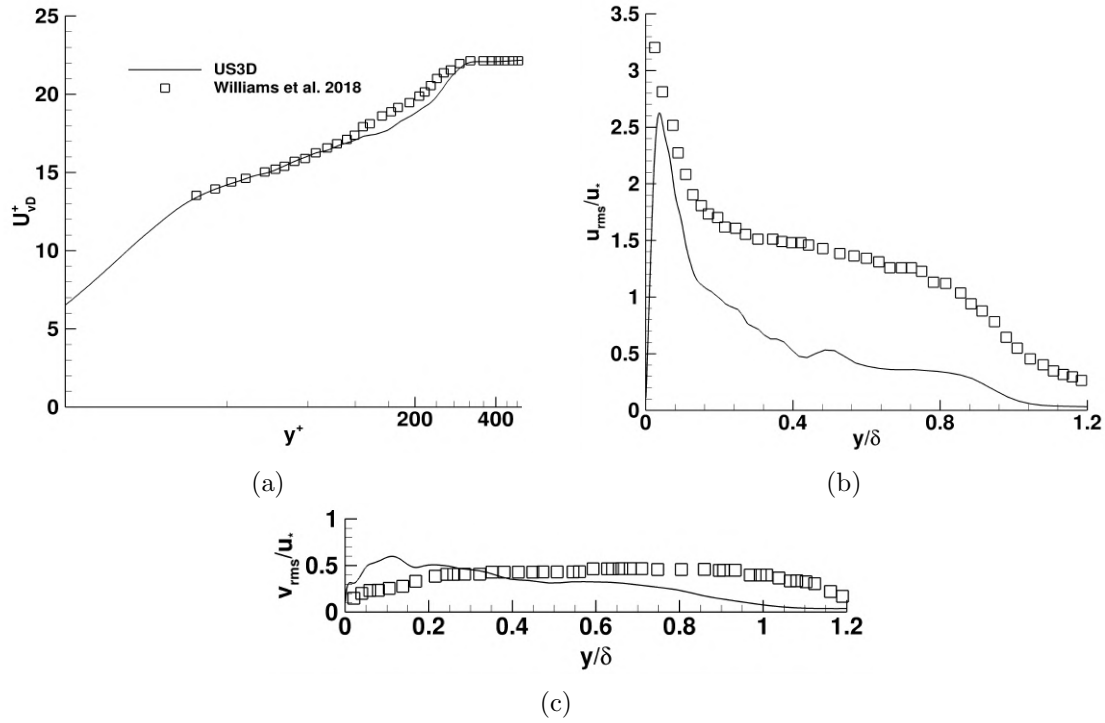

Figure 4.21: (a) The mean van Driest transformed velocity, (b) the RMS of the streamwise velocity, and (c) the RMS of the wall-normal velocity with respect to the wall-normal distance.

4.4.4 Results

In this section, we discuss three dynamically important flow structures in the vicinity of the trip. They are (1) the upstream vortex system, (2) the shock system, and (3) the shear layers from the top sides and corners of the trip and the counter-rotating vortex pair from its wake.

4.4.4.1 Upstream vortex and shock systems

First, let us investigate upstream vortex and shock systems ahead of the trip as shown in Figures 4.22(a) and 4.22(b). We observe that the number of the mean upstream vortices is four, and their structures look similar to the isolated cylinder trip (Subbareddy et al. 2014). Second, we observe that these mean upstream vortices interact with the shock system formed ahead of the trip. The interaction occurs via compression waves similar to the previous diamond-shaped trips and the isolated cylindrical trip by Subbareddy et al.

(2014). This interaction then could send dominant disturbances downstream in the wake and the shear layers causing unsteadiness and flow breakdown.

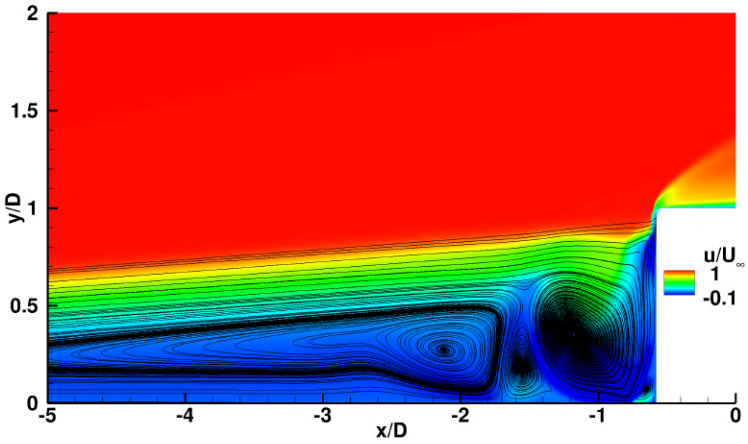

(a)

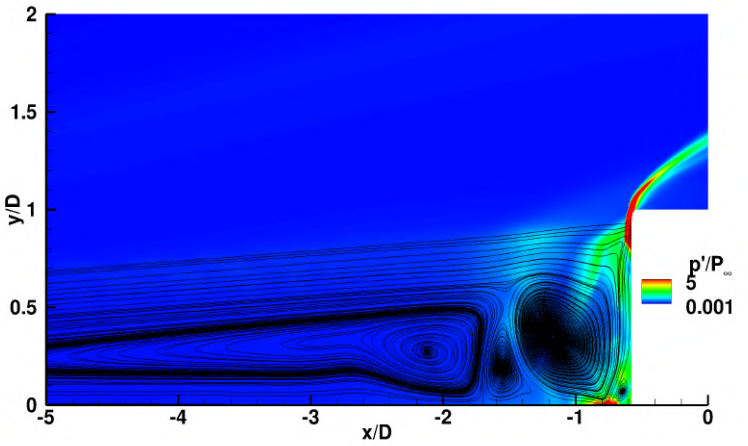

(b)

Figure 4.22: (a) The mean upstream vortex system and (b) the mean shock system ahead of a cylindrical trip considered in the present study.

4.4.4.2 Shear layers and counter-rotating vortex pairs

Third, we discuss the shear layers and the counter-rotating vortex pairs downstream of the trip array at different streamwise stations as shown in Figures 4.23 and 4.24. The counter-rotating vortex pairs (CVP-U) emanate from the wake, while CVP-L originates from the upstream vortex system similar to the previous trip array using diamond-shaped trips. We

observe that the CVP-U and the CVP-L are not directly on top of each other at all the streamwise locations. However, it is interesting to note that the mean turbulent kinetic energy in the CVP-L region is higher than in the CVP-U region as shown in Figure 4.25. This finding indicates that the dominant source of instability may be emanating from the upstream vortex system compare to the shear layers and the CVP-U.

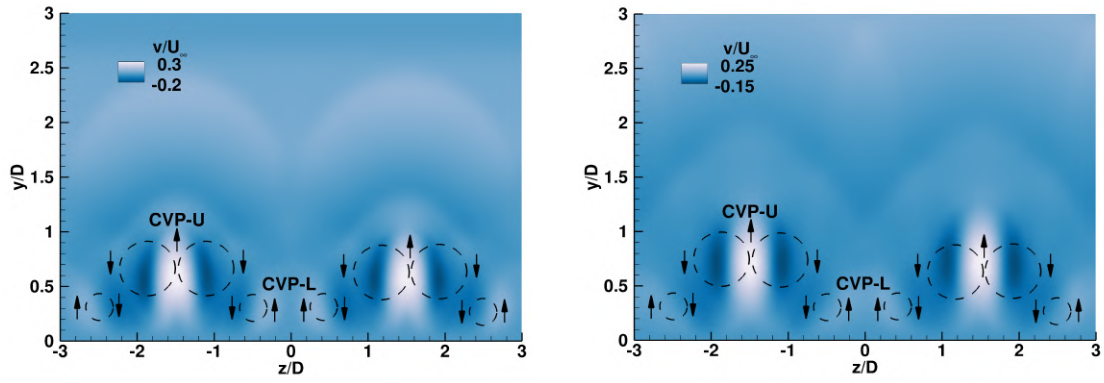

(a) (b)

Figure 4.23: The mean counter-rotating vortex pairs (CVP-L and CVP-U) are shown on a streamwise plane at (a) $x/D = 5$ and (b) $x/D = 10$.

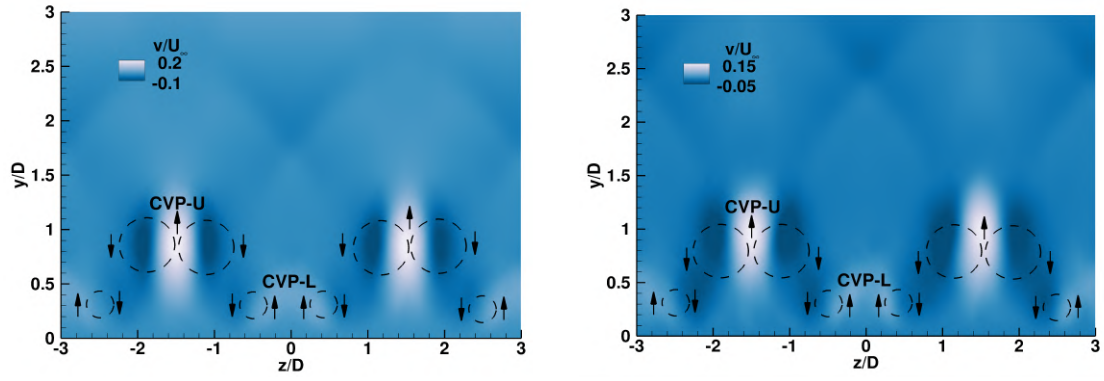

(a) (b)

Figure 4.24: The mean counter-rotating vortex pairs (CVP-L and CVP-U) are shown on a streamwise plane at (a) $x/D = 15$ and (b) $x/D = 20$.

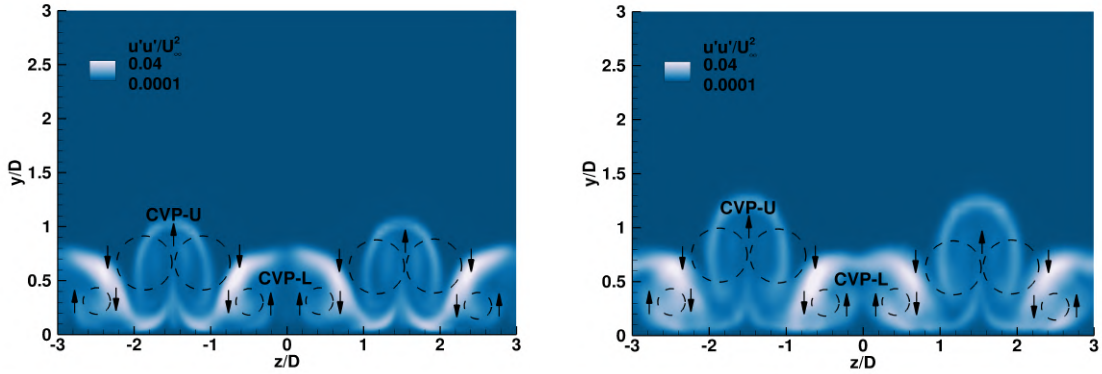

Figure 4.25: The RMS value of counter-rotating vortex pairs (CVP-L and CVP-U) shown on a streamwise plane at (a) $x/D = 5$ and (b) $x/D = 10$.

Q-criterion isosurfaces colored by instantaneous streamwise velocity is shown in Figure 4.26. Downstream of the trip array, we observe unsteadiness in the form of hairpin-like structures. Therefore, is the source of this unsteadiness the upstream vortex system or the downstream region of the trip (the shear layers and the CVP-U)? To resolve this issue, we first carry-out the PSD analysis at Probes 1, 2 and 3 shown in Figure 4.26. Peak-amplitude frequencies ($St = 0.2$ and 0.4) are observed at all the probes as shown in Figure 4.27(a). We then perform a freezing operation upstream of the trip array. The freezing operation, which is carried out for 10 flow through times, resulted in the disappearance of the instability observed downstream of the trip array. This finding is shown by time-series data of pressure after the freezing operation at Probe 1 as shown in Figure 4.27(b). Pressure fluctuations observed before freezing at Probe 1 decay after the freezing operation.

This finding indicates that the unsteadiness observed downstream of the trip array is due to disturbances traveling from the upstream vortex system similar to the isolated cylindrical trip by Subbareddy et al. (2014). Therefore, the dominant source of instability is dependent upon the trip shape in both isolated and trip-array configurations using diamond-shaped and cylindrical trips.

Furthermore, we also carry-out three-dimensional dynamic mode decomposition (DMD) to find the globally dominant frequency. The streamwise extension of the snapshot domain is $-5 \leq x/D \leq 15$ across the span. The sampling frequency and the total number of snapshots are 500 kHz and 126 respectively. Using the Chu disturbance norm, we find the dominant

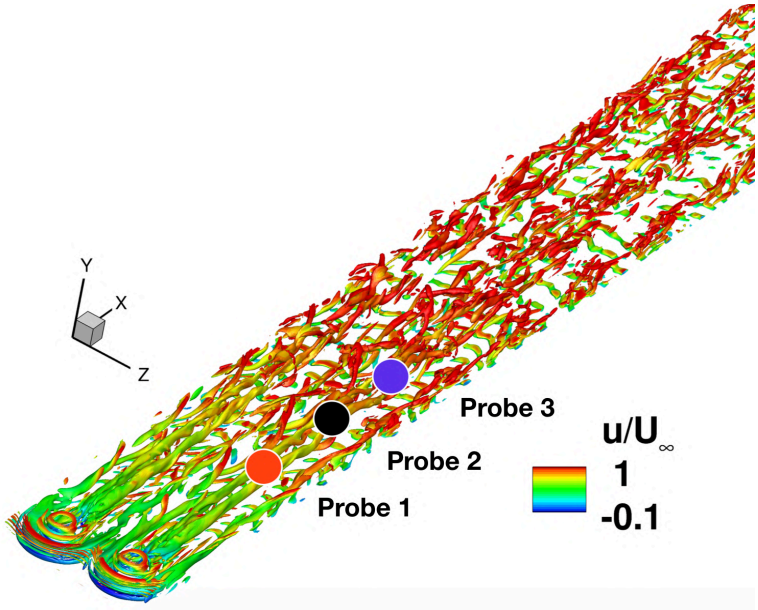

Figure 4.26: Q-criterion isosurfaces colored by streamwise velocity around the array of cylinder trips.

mode is at $St = 0.2$. Mode shapes of the dominant mode using pressure perturbations are strongly prominent in the region upstream of the trip, and these disturbances propagate downstream of the trip array as shown in Figure 4.28(a). Based on the performance loss analysis, the dominant mode (mode 1, say) contributes approximately 40 % of the flow dynamics as shown in Figure 4.28(b).

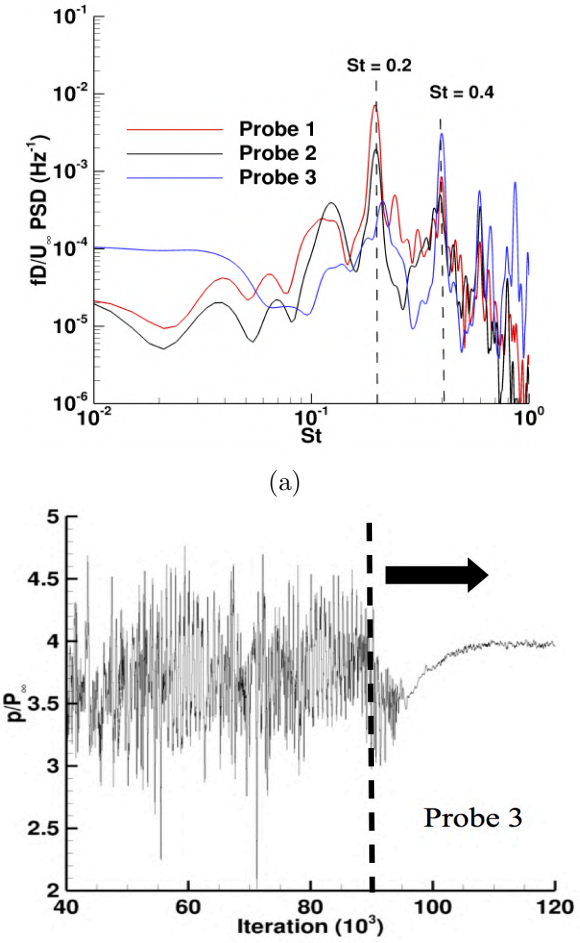

Figure 4.27: (a) Pre-multiplied PSD at Probes 1, 2 and 3 shown in Figure 4.26 and (b) a time-series plot of pressure at Probe 3 after the freezing operation.

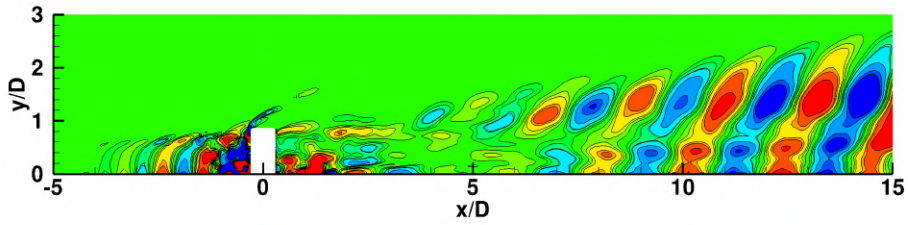

(a)

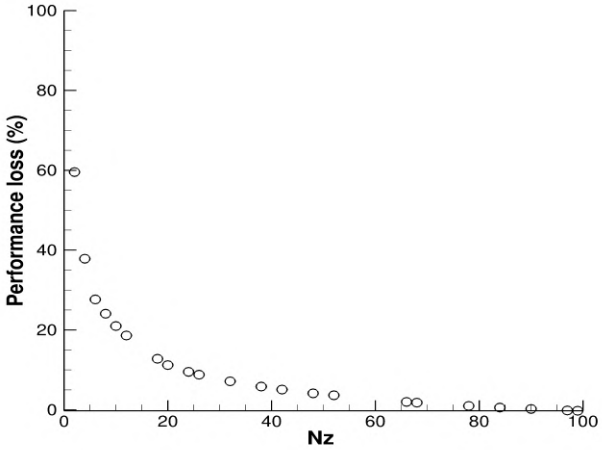

(b)

Figure 4.28: (a) Mode shapes of the dominant DMD mode 1 at $St = 0.2$ on the symmetry plane of one trip using pressure perturbations, and (b) performance loss with respect to the number of DMD modes.

Chapter 5

Active Tripping

The current study is intended to reinvestigate one of the wind tunnel tests by Berry et al. (2004) using a straight slot configured as a 2-D sonic jet on the Hyper-X forebody model. Streamwise streaks are observed downstream of the jet, and these streaks lead to turbulent flow. The objective of the present work is to investigate the physical mechanism of the formation of the streamwise streaks using DNS, DMD, and PSD analysis. An outcome of this analysis is the dominant spanwise wavelength and frequency downstream of the jet. A schematic of a JISC configuration using the 2-D jet is shown in Figure 5.1.

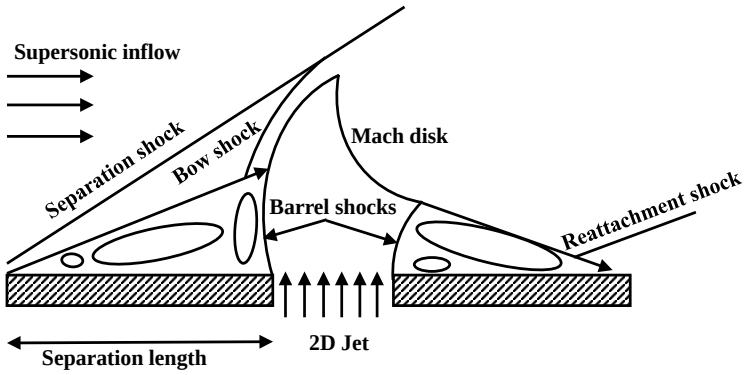

Figure 5.1: A schematic of a 2-D jet configuration.

The chapter is organized as follows: (5.1) provides an overview of the experiment considered in the present investigation, (5.2) illustrates the computational setup, (5.3) presents the results including dynamic mode decomposition, and (5.4) compares the current DNS data with the experiment. Numerical methods and modeling are same as in passive tripping.

5.1 Experimental facility

The facility associated with the present study is the 31-Inch Mach-10 wind tunnel at NASA Langley Research Center (LaRC). This facility is a blow-down tunnel in which dried, heated, and filtered air is used as the test gas. A range of operating conditions of the tunnel can be found in Miller (1990) and Micol (1998). It has a closed 31- by 31-inch test section. The freestream conditions are shown in Table 5.1. Three compression ramps, that are used in the experiment, have compression angles of 2.5^0, 8^0, and 11^0. Their respective streamwise lengths are 0.319 m, 0.135 m, and 0.258 m. The location of the 2-D jet is 187.5 mm downstream of the leading edge. The spanwise and the streamwise width of the slot is approximately 0.1016 m and 0.127 mm respectively. The angle of attack is 2^0. A schematic (inverted) of the experimental setup is shown in Figure 5.2.

Table 5.1: Freestream conditions: 31-Inch Mach-10 facility at NASA Langley Research Center

SN	Mach number (M_∞)	Temperature (T_∞)	Pressure (P_∞)	Unit Re_∞/m
1	10	49 K	252 Pa	2.2×10^6/m

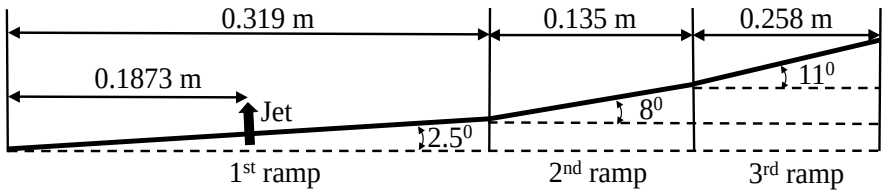

Figure 5.2: A schematic of the Hyper-X forebody and the 2-D jet.

5.2 Computational setup

5.2.1 Boundary conditions

A schematic of the boundary conditions of the given flow configuration is shown in figure 5.3. The inflow boundary is supersonic at Mach 10. In the present study, we mainly focus on instabilities generated by the sonic jet. Therefore, the first compression ramp is only

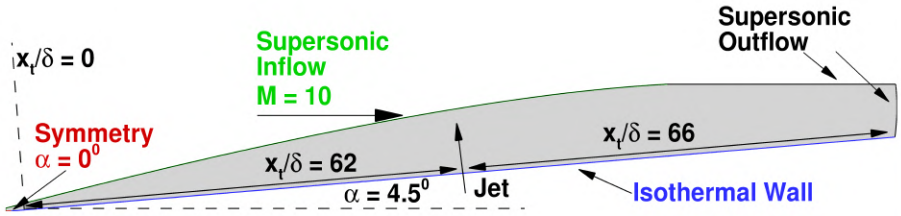

Figure 5.3: A schematic of the boundary conditions. Spanwise boundaries are transitionally periodic.

considered for the investigation. Hence, the flat plate (wall) has the net angle of attack of 4.5^0 (angle of attack (α) + the first compression ramp angle = 2^0 + 2.5^0). Since the runtime of the facility is short and does not change the initial wall temperature (= 300 K), the wall is isothermal. There is a symmetry boundary ahead of the flat plate at 0^0 degree angle of attack. The outflow boundary is supersonic. Spanwise boundaries are transitionally periodic. The boundary layer thickness ($\delta = \delta_{99}$) at the jet location without the jet is approximately 3 mm. Therefore, the location of the jet from the leading edge of the flat plate is 62δ. The streamwise length and the spanwise width of the domain parallel to the wall are 128δ and 33δ respectively. The jet, which is imposed wall-normal and has the injector inflow right next to the wall, is sonic at 300 K. The jet pressure is based on a parameter called pressure ratio (PR). Pressure ratio is defined as the ratio of the jet pressure to the stagnation pressure (937 Pa), which is based on the edge pressure at the jet location. In the present paper, PR varies from 0 to 50. One flow through time is defined as the time taken to cover a distance from the leading edge to the jet (62δ) at the freestream velocity of 1384 m/sec.

5.2.2 Grid generations

Structured grids are generated using Pointwise, a mesh generator with a built-in smoother. Singularities are used to locally cluster the grids near the jet. The near-wall spacing of the jet has y^+ of 0.1. Figure 5.4 shows mesh generation in the vicinity of the sonic jet from the top view. The meshes are also shown in Figure 5.5(a) from the side view and in Figure 5.5(b) from an isometric view. Red circular dots indicate the presence of mesh singularities, while the red rectangle (tall and skinny) near the wall shows the 2-D jet injector. Grid convergence study of the current mesh configuration is carried using the

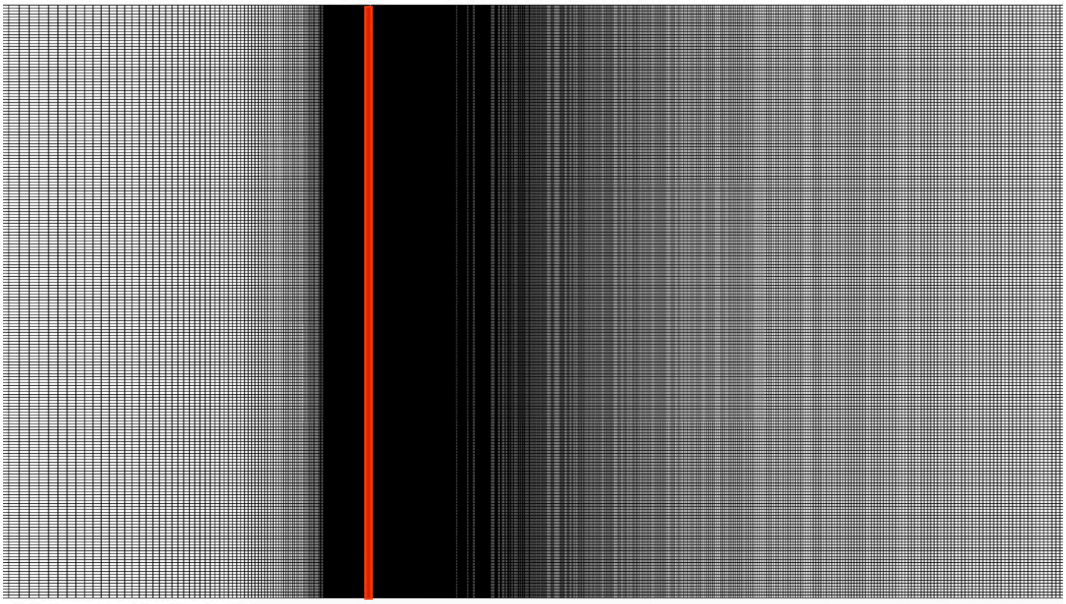

Figure 5.4: Mesh from the top view upstream and downstream of the 2-D jet. The red line indicates the straight slot used in the experiment.

mean wall-normal profile at different streamwise locations and PSD of spanwise velocity at a mid-span location on the symmetry plane (probed at $x/\delta = 62.5$, $y/\delta = 0.2$). Three meshes considered for the convergence study are 25 (mesh-1), 50 (mesh-2), and 100 (mesh-3) million cells at $PR = 25$. Figure 5.6(a) shows that mesh-1 may be grid-converged as mesh-1 and mesh-2 have the mean same wall-normal profiles of streamwise velocity at different streamwise stations. However, Figure 5.6(b) indicates that mesh-2 is grid-converged as mesh-2 and mesh-3 have the same peak-amplitude frequency at around 6.3 kHz, while 4.8 kHz is the peak-amplitude frequency in mesh-1 at the same probe. The sampling frequency of 100 MHz is used to compute the mean, the RMS value, and PSD of a flow quantity of interest in the current study. The computational time step of 10 nanoseconds is used in the present investigations. PSD of spanwise velocity (w) is computed as shown in 5.1, where k ranges from 1 to N_f discrete frequency disturbances.

$$PSD_k(\mathrm{m^2sec^{-2}\ Hz^{-1}}) = \frac{1}{2f_s}|w_k|^2 \tag{5.1}$$

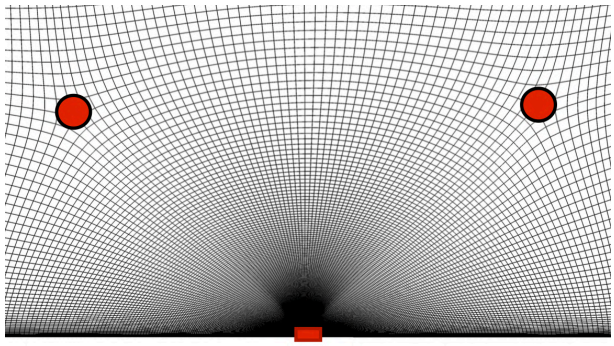

(a)

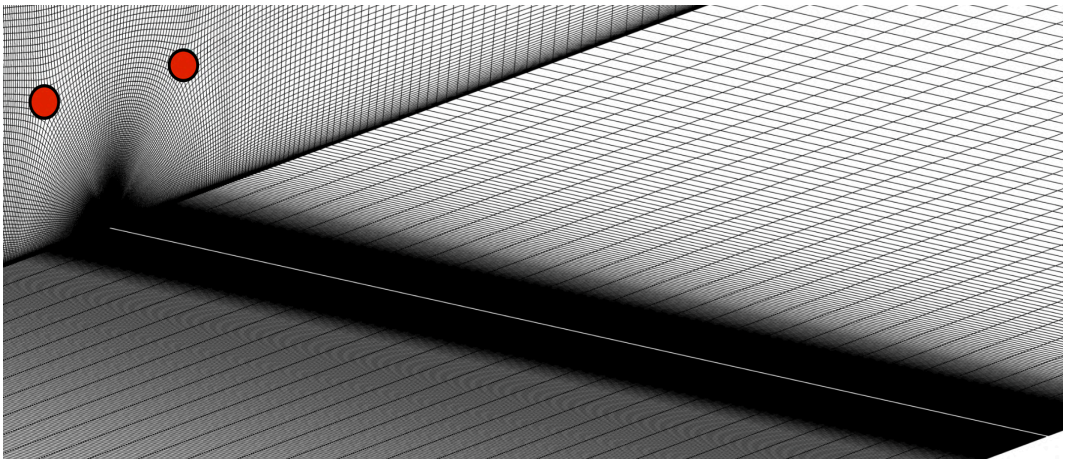

(b)

Figure 5.5: (a) Mesh showing two singularities (red dots) from the side view and (b) mesh showing the 2-D sonic jet (red line) and grids near the jet from the isometric view.

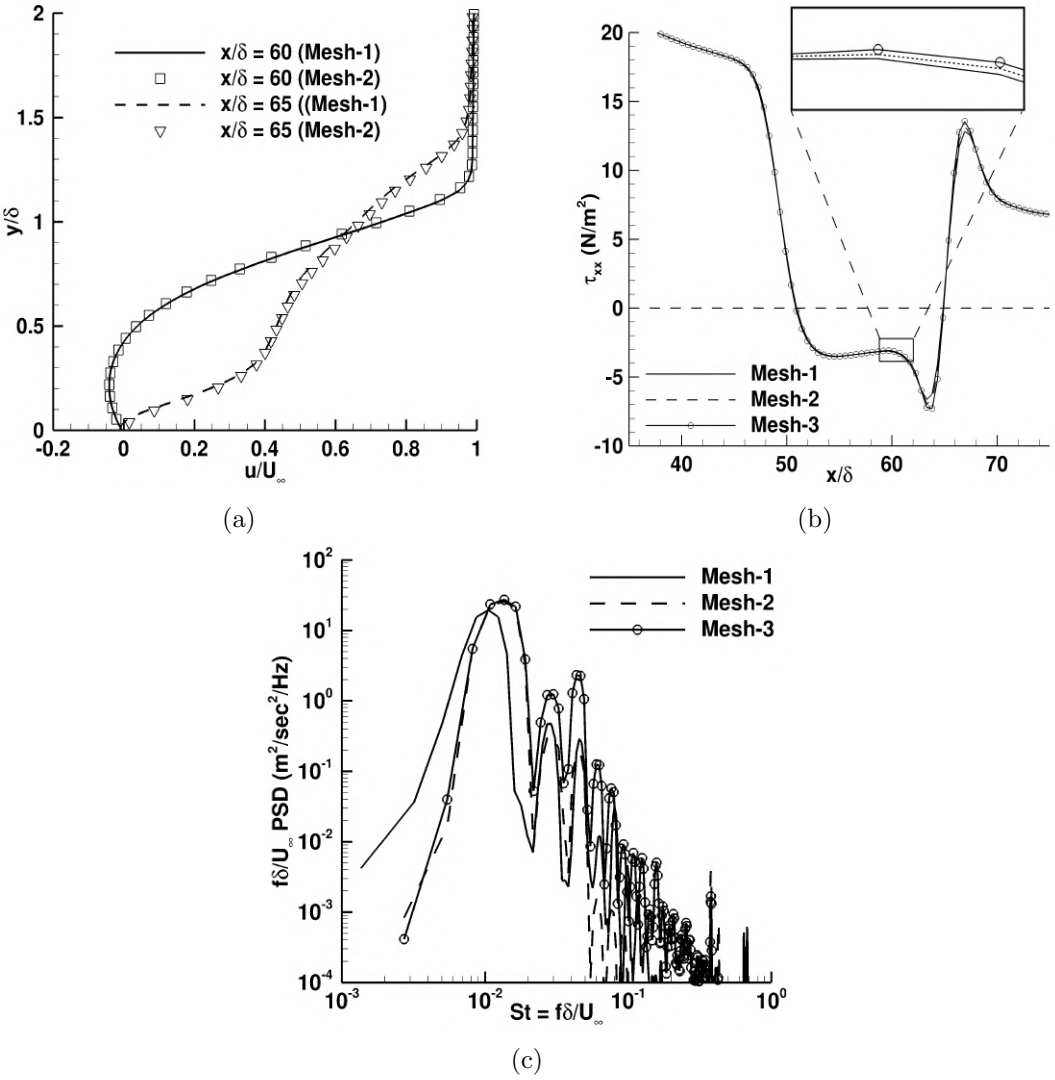

Figure 5.6: Grid convergence study using (a) the mean wall-normal profile of streamwise velocity, (b) the streamwise evolution of the mean streamwise wall-shear stress, and (c) PSD of spanwise velocity probed at $x/\delta = 62.5$ and $y/\delta = 0.2$.

5.3 Results

This section consists of two major subsections. First, we perform bifurcation analysis using different PR ratios. Second, we select an unsteady PR case to understand its flow physics that causes the flow to become turbulent.

5.3.1 Bifurcations

A bifurcation in the current context is a PR ratio that leads to a noticeable change in the flow field. Here, we discuss three successive bifurcations based on different pressure ratios (PR). The PR ratios, which are varied in this subsection, range from 0 to 35. To study these bifurcations, five specific PR ratios are shown in Figure 5.7. All plots are on a symmetry plane colored by instantaneous Mach number. When the PR ratio is equal to 0.5, no significant change in the flow structure is observed as shown in Figure 5.7(a). As the PR ratio is increased to 1, a 2-D steady bubble (D-B) is formed downstream of the jet as shown in Figure 5.7(b). This 2-D steady bubble formation is the first bifurcation point. Figure 5.7(c) shows that a 2-D steady upstream bubble (U-B) is formed when the PR ratio is 4. As the PR ratio is increased to 8, a secondary upstream bubble (U-B-S) is formed between the U-B bubble and the jet as shown in Figure 5.7(d). At this latter PR ratio, the flow becomes weakly unsteady, and therefore, is the second bifurcation point. With the increment of the PR ratio to 25, the flow becomes fully unsteady that is evident by the presence of additional secondary vortices upstream and downstream of the jet as shown in Figure 5.7(e). This PR ratio is the third bifurcation point.

Therefore, the three successive bifurcations are (1) a 2-D steady bubble formation, (2) a 3-D weakly unsteady (quasi), and (3) a 3-D fully unsteady. Figure 5.8 shows these three bifurcations with respect to PR. In Figure 5.8, Amp is defined as the difference between the maximum and the minimum amplitudes of the sinusoidal unsteadiness at the probe location ($x/\delta = 62.5$, $y/\delta = 0.2$, $z/\delta = 0.0$). We observe the second bifurcation point is at $PR = 8$ after which flow begins to be quasi-unsteady. In the current work, the flow becomes quasi-unsteady if the unsteady perturbations observed ahead of the jet dissipate later downstream. Finally, we note the third bifurcation point ($PR = 22$) at which the flow is fully unsteady upstream and downstream of the jet. These plots are spanwise-converged.

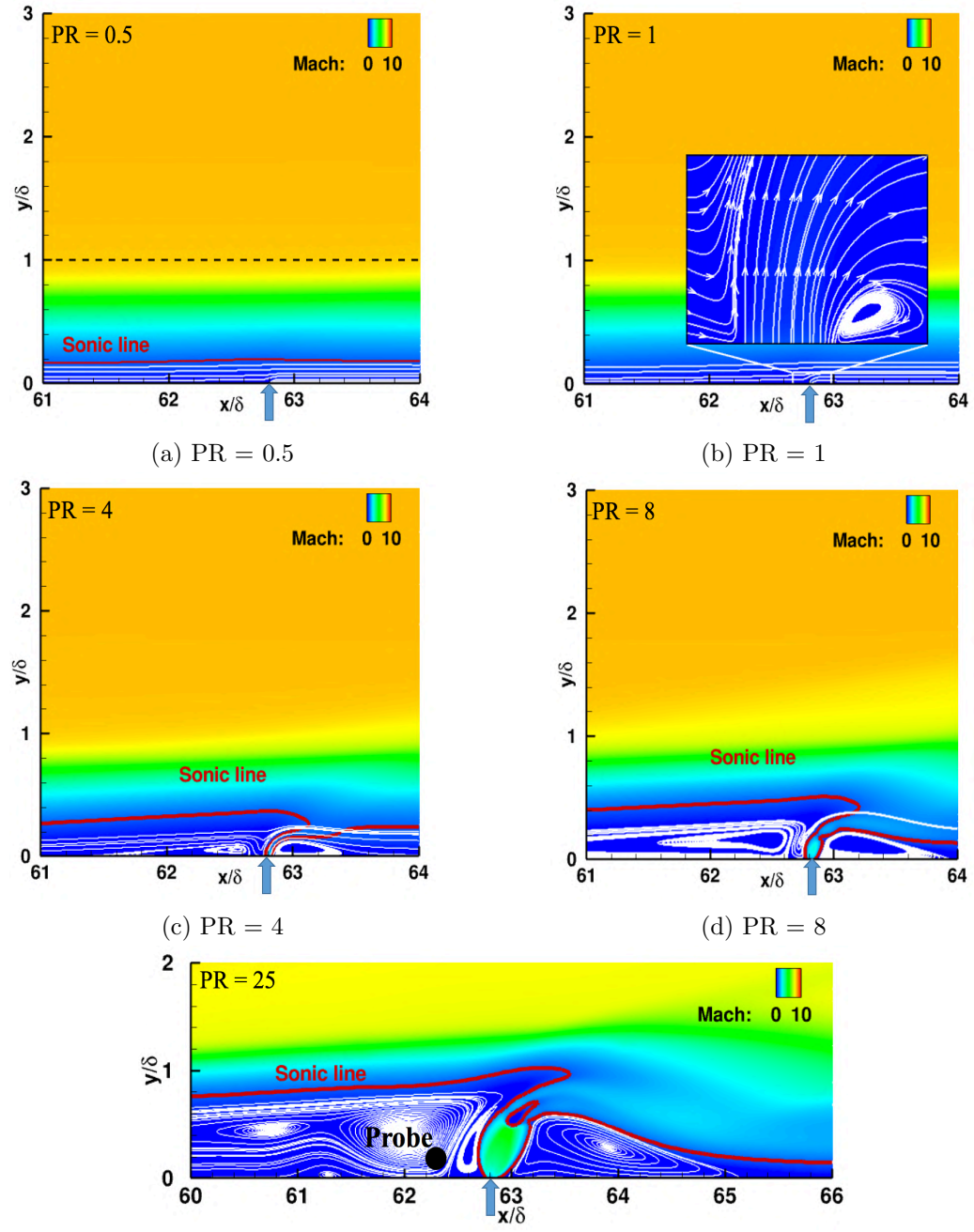

(a) PR = 0.5

(b) PR = 1

(c) PR = 4

(d) PR = 8

(e) PR = 25

Figure 5.7: Flow dynamics in the vicinity of the 2-D jet due to different PR ratios.

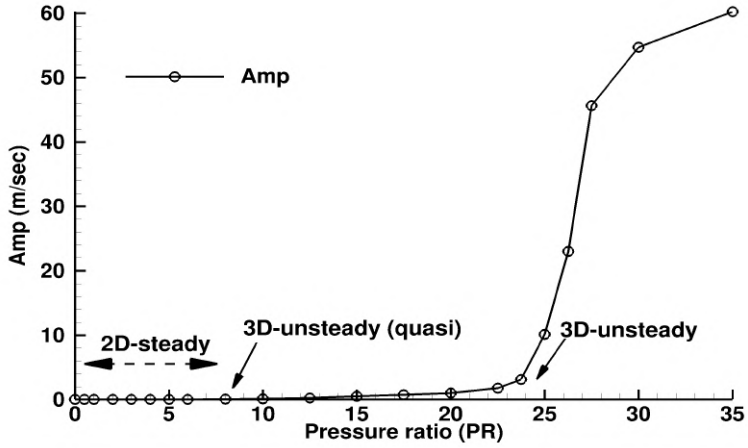

Figure 5.8: Three successive bifurcations: (1) 2-D steady bubble formation, (2) 3-D quasi-unsteady, and (3) 3-D fully unsteady.

5.3.2 Three-dimensional simulations

In this subsection, we characterize three-dimensionality of the flow induced by the jet using PSD and DMD. In Figure 5.9, Q-criterion isosurfaces colored by the spanwise velocity upstream and downstream of the jet are shown. The Q-criterion isosurfaces particularly show streamwise vortices downstream of the jet. Furthermore, a spanwise periodicity of the streamwise vortices (streamwise streaks) is observed both upstream and downstream of the jet. Therefore, a few questions arise: (1) what is the source of these streaks, and (2) what is their dominant spanwise wavenumber and temporal frequency?

On the left spanwise plane shown in Figure 5.9, instantaneous Mach number contours are plotted. We observe four shocks; (1) a bow shock from the leading edge of the flat plate, (2) a separation shock ahead of the upstream bubbles, (3) a secondary bow shock ahead of the 2-D jet, and (4) the reattachment shock downstream of the jet.

5.3.3 Spatio-temporal analysis

In this subsection, we characterize unsteadiness at different spatial locations upstream and downstream of the jet using PSD, the mean turbulent kinetic energy and DMD of the 3-D simulations at $PR = 25$. The PR ratio of 25 is selected as the unsteadiness observed around the jet is more apparent than lesser PR cases. First, we compute the dominant spanwise wavenumber of the streamwise streaks as shown in Figure 5.9. Second, we find the dominant

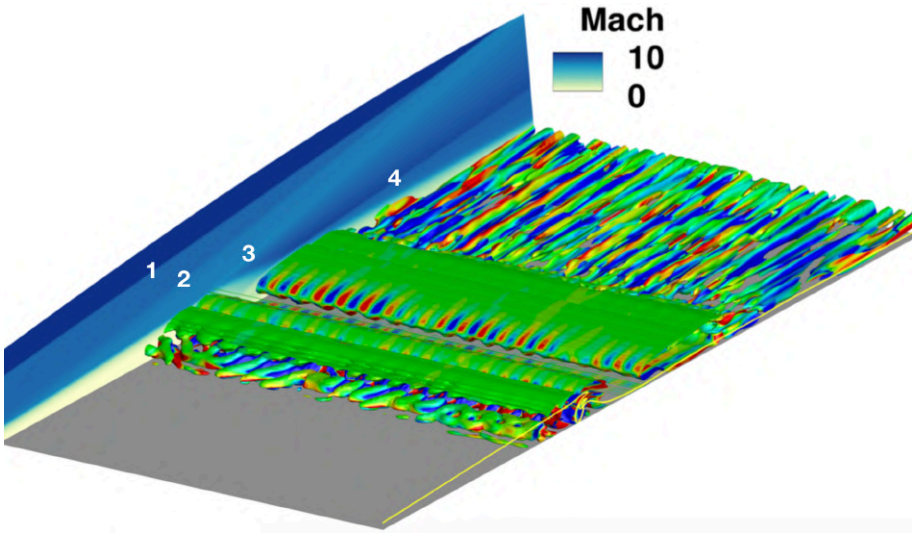

Figure 5.9: An isometric view of Q-criterion colored by instantaneous spanwise velocity. Instantaneous Mach contours on the left spanwise plane show different shocks near the jet. Numbers 1-4 indicate different shock systems. A yellow-colored streamtrace, that indicates a sonic line (sonic jet), is shown on the right side.

DMD mode which has the strongest representation of the flow dynamics.

5.3.3.1 Dominant spanwise wavenumber

The dominant spanwise wavenumber using spanwise PSD of spanwise wall shear stresses at two streamwise locations (upstream of the jet: $x/\delta = 60.5$, $y/\delta = 1$ and downstream of the jet: $x/\delta = 68.5$, $y/\delta = 1$) is computed. The grid-converged time-averaged spanwise PSD is shown in Figure 5.10. At both streamwise locations, we observed that the dominant spanwise wavenumber in terms of $\beta\delta$ is approximately 6.4. β is defined as $2\pi/\lambda$, and it is the spanwise wavenumber of a streamwise streak. λ is defined as the spanwise wavelength of the streak. Furthermore, it is observed that spanwise velocity fluctuations at all spanwise wavenumbers increase from upstream to downstream of the jet.

5.3.3.2 Dynamic mode decomposition

Now let us find globally dominant modes using DMD and analyze their mode shapes to study the instability mechanism. For the selection of the dominant modes, we use the Chu disturbance energy norm similar to the previous cases. Mode shapes of spanwise velocity

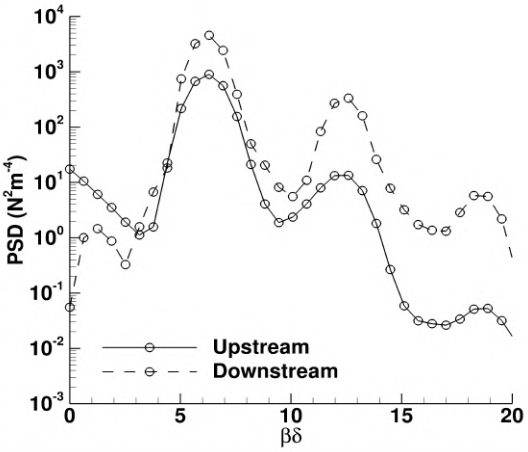

Figure 5.10: The time-averaged spanwise PSD analysis of spanwise wallshear upstream (x/δ = 60.5) and downstream (x/δ = 68.5) of the jet using the mesh-2.

associated with the selected DMD modes are studied so as to be consistent with the PSD analysis and the DNS simulations performed earlier.

The region of snapshot considered in the present trip configuration ranges $x/\delta \in$ [42.5, 92.5] across the span height. The region was selected because (1) no flow breakdown region is included (minimizes nonlinearity), (2) all modes of instability can be studied, and (3) the number of degrees of freedom is smaller (compared to the entire domain). The sampling period is 5.0 μsec, and the number of snapshots is 100 in the present study. Since the dominant frequencies observed in the previous PSD analysis are at St = 0.015 and 0.03, and the present Nyquist frequency is at St = 0.22, the sampling frequency is sufficient to capture the relevant high-frequency modes. M = 5 million cells and N = 101 snapshots. Since the ψ matrix is tall (M) and skinny (N), the TSQR algorithm is implemented to carry out parallel QR factorizations.

5.3.3.2.1 DMD results

We obtain two dominant DMD modes at St = 0.015 and St = 0.03 based on the Chu disturbance energy norm. Frequencies of these DMD modes are consistent with the previous PSD analysis. To quantify the contribution of each DMD mode to the flow dynamics, we calculate their respective performance loss. Based on the performance loss, mode 1 (St = 0.015) and mode 2 (St = 0.03) contain approximately 82% and 7% of the total energy of

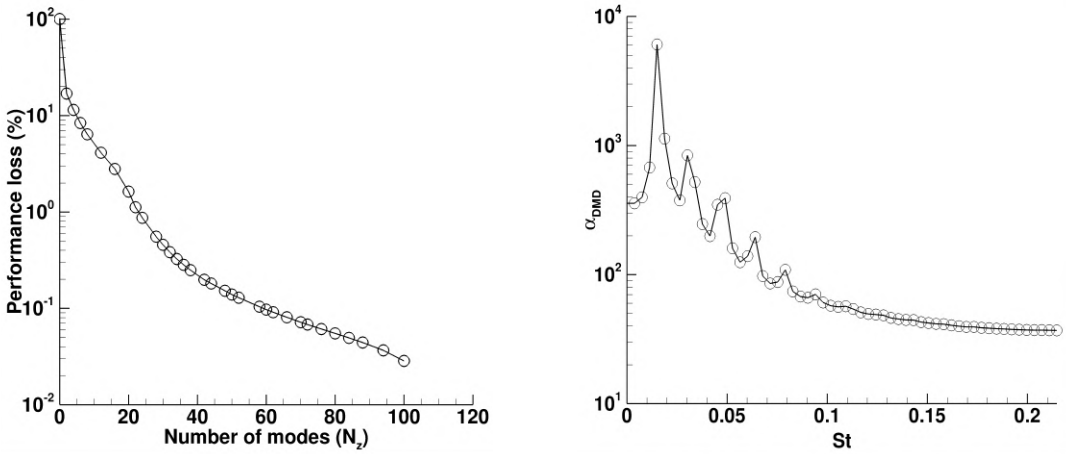

(a) (b)

Figure 5.11: (a) Performance loss and (b) DMD spectrum at $PR = 25$.

the flow dynamics respectively. The performance loss analysis is shown in Figure 5.11(a). In Figure 5.11(b), we observe that the dominant mode is around at 0.015 followed by its harmonic modes (0.03 and 0.045). This finding is also consistent with the performance loss and the PSD analysis of the current 3-D simulations.

Let us consider the dominant mode 1 to find the source of the streamwise streaks observed as it captures most of the energy of fluid dynamics. Figure 5.12 shows the streamwise streaks upstream and downstream of the jet using spanwise velocity fluctuations of the mode 1. The nondimensionalized spanwise wavenumber ($\beta\delta$) is around 6.4 which is consistent with the previous PSD analysis of spanwise velocity at the two streamwise locations.

To understand the source of the streaks observed in Figure 5.12, let us study the temporal evolution of mode 1 near the jet and find from where the streaks are emanating. In Figures 5.13(a)-(h), we observe that the direction of spanwise velocity perturbation alters from positive to negative and vice-versa in the region, where the coupled system of the primary upstream bubble and the secondary upstream bubble interact to cause the second bifurcation. In other words, these two bubbles emanate two flow structures that lie on top of each other and have opposite spanwise velocities. These flow structures then travel to the top of the downstream bubbles to form a streamwise streak. This process is also shown in Figure 5.14 from the back view of the sonic jet. Next, we propose a possible mechanism to obtain insights on the formation of the two unsteady flow structures from the bubbles

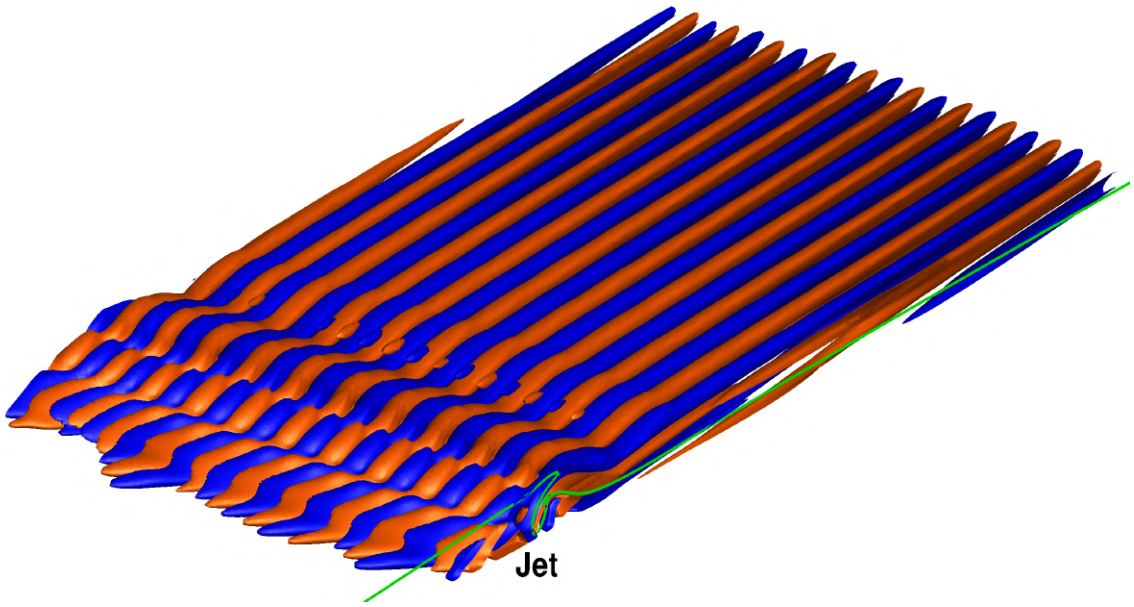

Figure 5.12: Mode shape of the mode 1. Isosurfaces are of spanwise velocity perturbation, and they are colored by spanwise velocity perturbation itself.

and the coupling between the two upstream bubbles at the same PR ratio.

5.3.4 Instability Mechanism

Figure 5.15(a) shows instantaneous contours of streamwise velocity on a wall-parallel plane ($y/\delta = 1.0$). Contour lines (shown by black lines) show the prominence of the primary and the secondary upstream bubbles. We observe that the spanwise undulation of the primary bubbles is complementary to the secondary bubbles. As the flow travels along the right direction towards the primary bubbles, two flow structures are formed on either side of the maximum bubble strength locations (shown by yellow-colored contours) with opposite spanwise velocities. These flow structures travel towards the secondary upstream bubbles. Since the secondary bubbles with the maximum bubble strength are present downstream of the center of the two primary bubbles with the maximum strength, the spanwise velocities of the two flow structures change in directions while traveling across the secondary bubbles. Finally, the two flow structures from each secondary bubble travel on top of the sonic jet to form a streamwise streak downstream.

Figure 5.15(b) shows instantaneous contours of spanwise velocity. Contour lines, that are

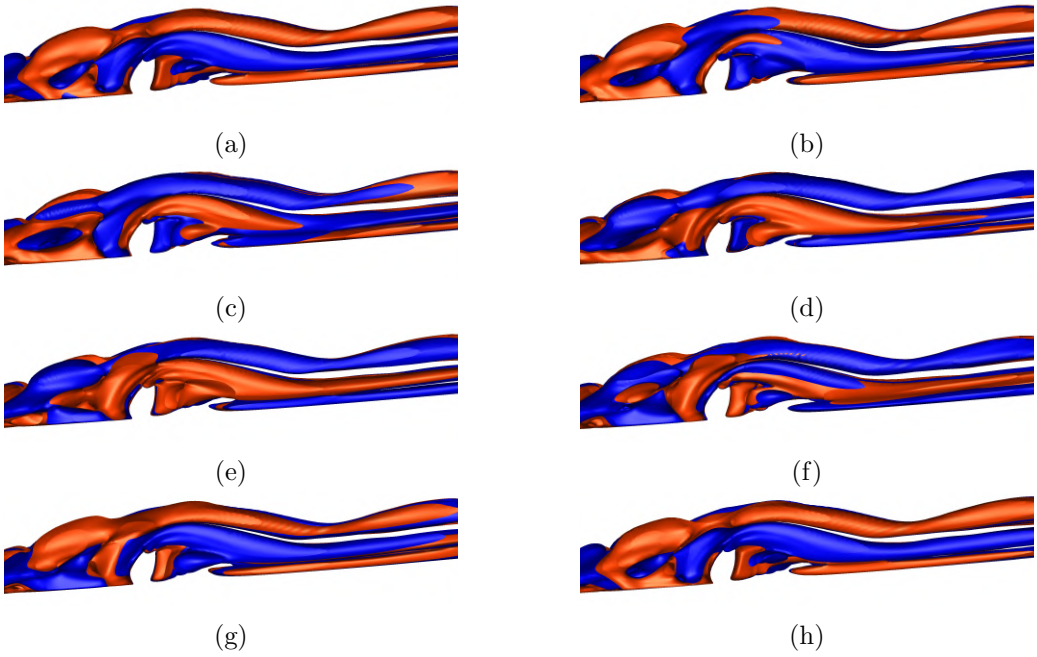

Figure 5.13: One periodic temporal evolution of mode 1 from the side view in the vicinity of the jet. $PR = 25$.

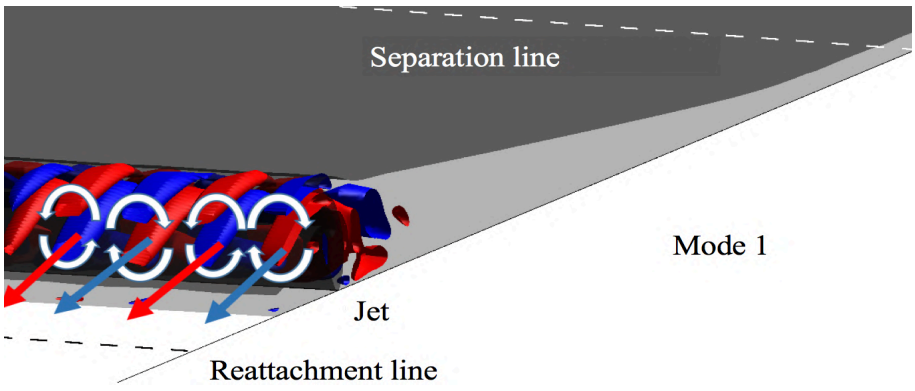

Figure 5.14: Physical mechanism of the formation of streamwise streaks downstream of the jet. Back view.

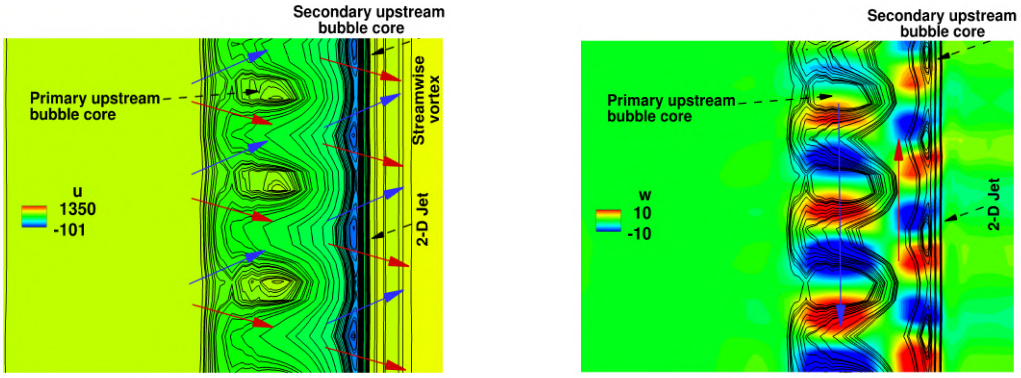

(a) (b)

Figure 5.15: (a) The formation of the streamwise streaks in the upstream region and (b) the net spanwise movement of the upstream bubble system.

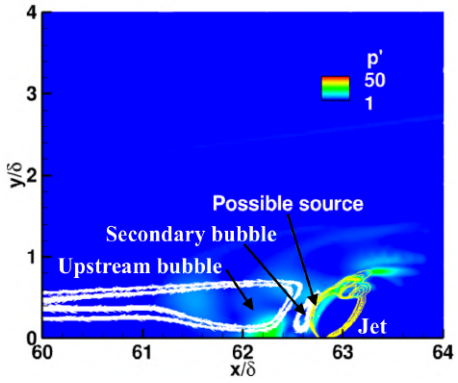

Figure 5.16: The R.M.S. contours of pressure on a plane at $z/\delta = 0$.

shown by black lines, indicate streamwise velocity. These lines, as shown in Figure 5.15(a), show the prominence of the upstream bubbles. It has been found that the spanwise vorticity of the primary bubble is greater than the secondary bubble. Therefore, the non-zero net spanwise movement of the upstream bubble system is found. Hence, we observe spanwise velocity fluctuations at a temporal frequency at a fixed probe as discussed earlier in the current study.

The spanwise undulation of both bubbles is possibly due to the presence of the secondary bubbles, which modulates the primary bubbles at a specific spanwise wavelength. The source of the unsteadiness appears to be in the region between the secondary bubbles and the sonic jet as shown by the R.M.S. of pressure in Figure 5.16.

5.4 Comparison to the experiment

DNS simulations show that there exist streamwise streaks downstream of the jet similar to the trip array configurations discussed in the earlier chapters. It was found later that the experimental slot-width (=0.2286 mm) was larger than the one used earlier after re-measurement. Streamwise streaks downstream of the correct slot-width are also shown in Figure 5.17 using instantaneous temperature contours on a wall-parallel plane at $y/\delta = 0.7$. Since the experimental data is currently not permitted for a public release by NASA, numerical data is only presented here. Based on private communication with Scott Berry at NASA LaRC, the wavelength of the streamwise streaks was observed to be around 10 mm, i.e., non-dimensionalized streak length ($\beta\delta \approx 0.19$) at $PR = 25$. The mean dominant spanwise-streak wavelength is known to be around $\beta\delta = 0.19$ as shown in Figure 5.18. The PSD analysis across span was carried out at $y/\delta = 0.7$ and $x/\delta = 80$. The entire simulation went through approximately 30 flow through times.

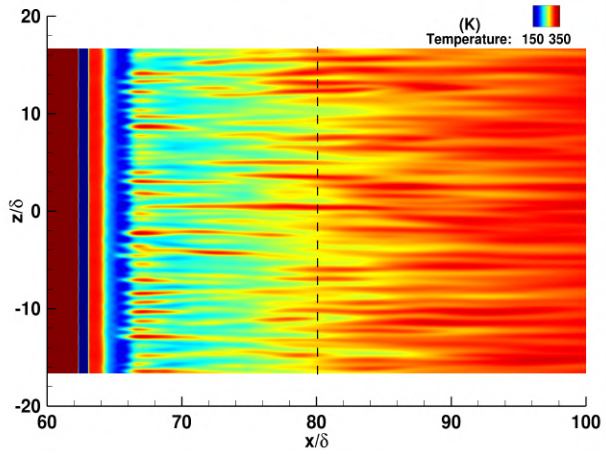

Figure 5.17: Temperature contour (in K) on a wall-parallel plane at $y/\delta = 0.7$ and $PR = 25$. The dashed line is the spanwise line where the time-averaged spanwise PSD analysis is carried out.

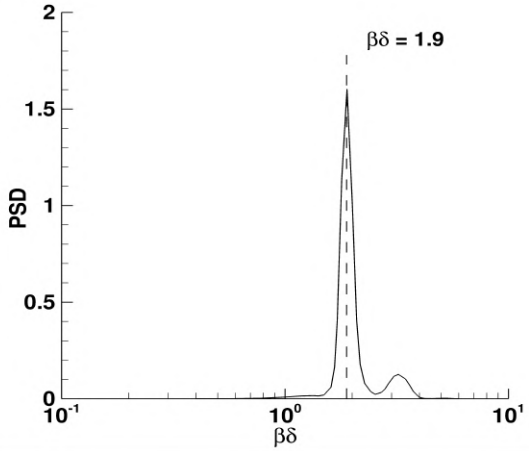

Figure 5.18: The mean spanwise PSD ($T'/\overline{T}$) of temperature at $x/\delta = 80$ and $y/\delta = 0.7$. $PR = 40.0$

Chapter 6

Parametric Study: Active Trips

In this chapter, we carry-out parametric studies based on (1) the thermal nature of the wall, (2) real gas effects, (3) the angle of injection, (4) streamwise streaks at different PR ratios. In addition, we also compare different jet parameters such as the mean Mach-disk height, and the mean upstream and downstream separation lengths with existing models.

6.1 Effects of thermal nature of the wall

First, let us change the thermal nature of the wall from isothermal to adiabatic and study its effect on the instability mechanism. Since the freestream Mach number (M_∞) is 10, the thermal nature of the wall can have a significant effect in the boundary layer, and therefore, the instability mechanism. The value of δ_{99} (denoted as δ) is 4.9 mm at the jet location using the adiabatic wall, i.e., the location of the sonic jet is at $x/\delta = 38.4$ in this case. We carry-out another bifurcation analysis similar to the isothermal case. In Figure 6.1(a), we observe that the first bifurcation point, which is the formation of the steady 2-D bubble downstream of the jet, is $PR = 1$. As we increase PR to 15, the second bifurcation point, which is the formation of the upstream secondary bubble leading to quasi-unsteady flow, is observed. If the pressure ratio is increased beyond 45, the flow becomes unsteady. This pressure ratio is the third bifurcation point. Except for the first bifurcation point, the second and the third bifurcation points are shifted to higher values when compared to the isothermal wall-boundary case. A possible cause of these shifts of the second and the third bifurcation points is the thicker boundary layer in the current wall-boundary case.

Now let us investigate unsteadiness in the vicinity of the jet as shown in Figure 6.1(b) at $PR = 50$ since the unsteadiness at this PR ratio is more clearly observed. The peak-amplitude frequency of spanwise velocity at a probe location ($x/\delta = 38.0$, $y/\delta = 0.2$, $z/\delta = 0.0$) is at $St = 0.009$, which is less than in the isothermal case. Similarly, the non-dimensional dominant spanwise wavenumber ($\beta\delta$) across span at ($x/\delta = 42.5$, $y/\delta = 0.3$) is 3.5 (see Figure 6.1(c)), which is also less than in the isothermal case.

6.1.1 DMD results

To investigate the instability mechanism, we carry-out DMD analysis using the same parameters (sampling frequency, sampling domain size, sampled quantity). The total degrees of freedom is approximately 4 million cells. We obtain the dominant DMD mode at $St = 0.009$ (mode 1) based on the Chu disturbance energy norm. According to the performance loss analysis as shown in Figure 6.2(a), mode 1 is observed to capture almost 88% of the total energy of the flow dynamics in the selected domain. Non-dimensionalized spanwise wavenumber ($\beta\delta$) is found to be 3.5 (see Figure 6.2(b)). These findings are also consistent with the previous DNS and PSD data. Furthermore, we observe that the source of streamwise streaks is still the upstream bubble system, and this funding is similar to the isothermal case.

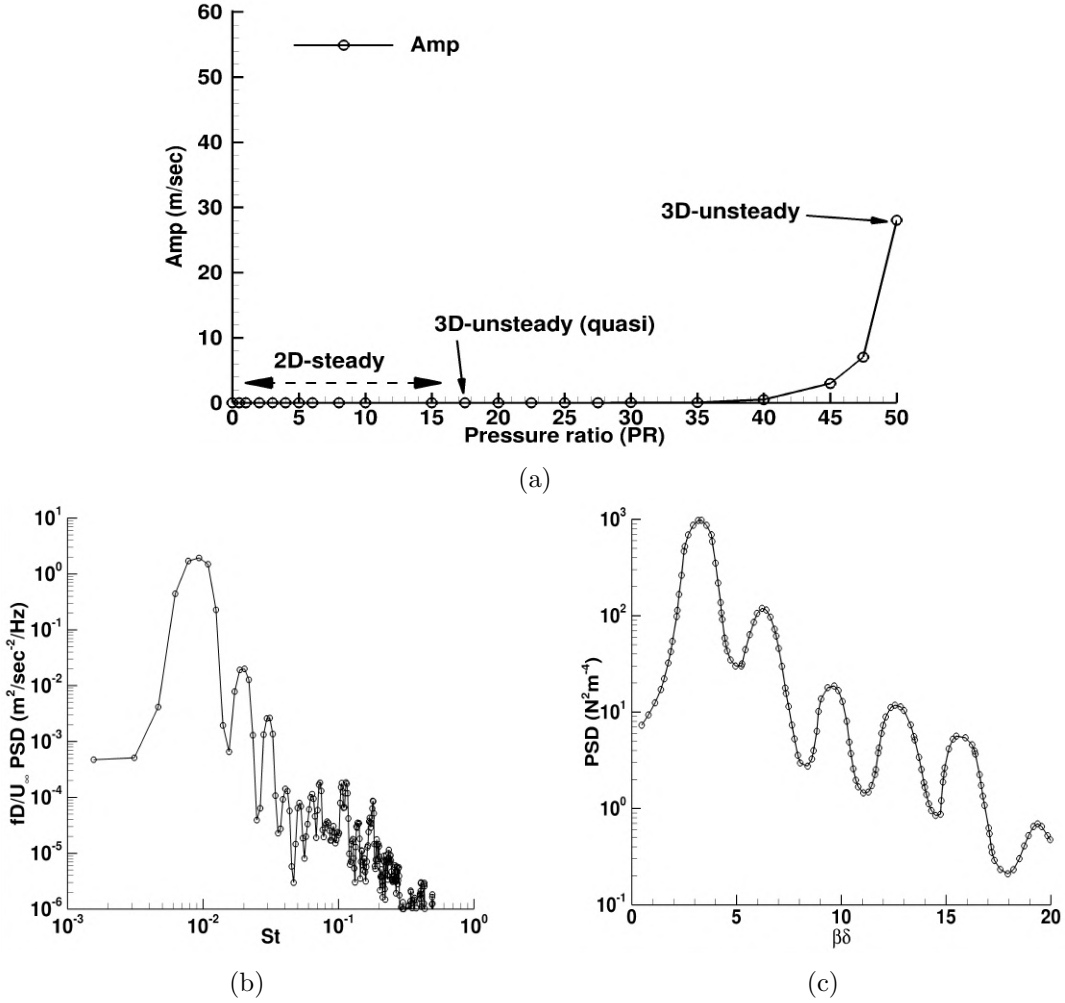

Figure 6.1: (a) Bifurcation analysis using the adiabatic wall, (b) the PSD analysis of spanwise velocity at a probe ($x/\delta = 38.0$, $y/\delta = 0.2$, $z/\delta = 0.0$), and (c) the time-averaged spanwise PSD analysis at a streamwise location ($x/\delta = 42.5$) using spanwise wall-shear stress.

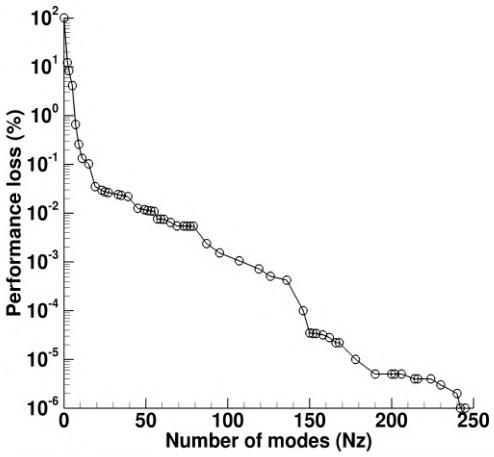

(a)

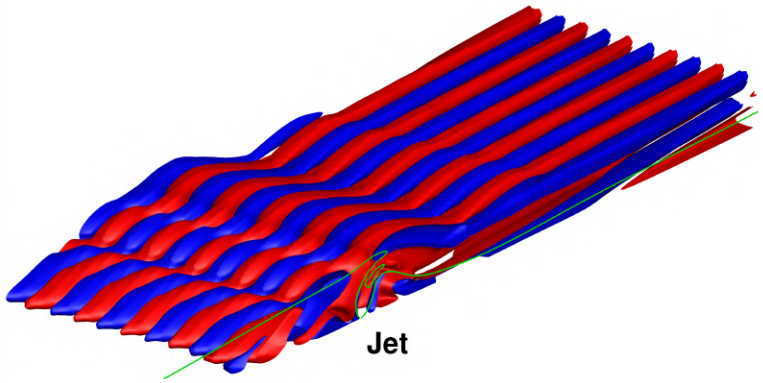

(b)

Figure 6.2: (a) Performance loss in the adiabatic case and (b) isosurfaces of mode shapes of the dominant DMD mode using contours of spanwise velocity perturbations.

b

6.2 Real gas effects

In this section, we study the effects of real gas on the flow unsteadiness in the isothermal case. Gases considered are N_2 and 0_2. Their heat capacity at constant pressure (C_p) changes with temperature (T) in this gas-type setup. Equation 6.1 is based on Lewis curve fitting.

$$C_p(T)/R(J/K) = a_1 + a_2T + a_3T^2 + a_4T^3 + a_5T^4 \tag{6.1}$$

The values of all the coefficient a_i (i = 1,5) are shown in Table 6.1.

Table 6.1: Thermodynamic co-efficients: N_2 and O_2. McBride et al. 1993.

SN	Species	a_1	a_2	a_3	a_4	a_5
1	N_2	3.531E00	-1.2366E-04	-5.03E-07	2.435E-09	-1.4088E-12
2	O_2	3.782E00	-2.9967E-03	9.847E-06	-9.68E-09	3.243E-12

First, we compare the peak-amplitude frequency at a probe located at (x/δ = 38.0, y/δ = 0.2, z/δ = 0.0) using both real and perfect gases as shown in Figure 6.3(a). Similarly, we also investigate differences of the nondimensionalized dominant spanwise wavenumber ($\beta\delta$) as shown in Figure 6.3(b). No significant difference is found using either real or perfect gas. This finding indicates that the previous analysis of the instability mechanism using the perfect gas is still valid at the present high Mach number simulations. We expect to obtain similar findings using DMD, and therefore, do not perform it in this section.

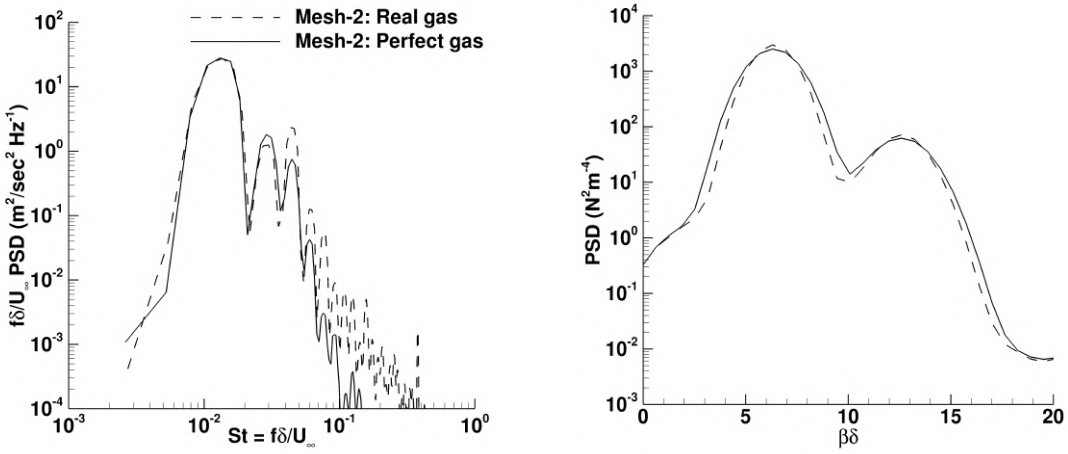

(a) (b)

Figure 6.3: (a) Premultiplied PSD of spanwise velocity at the probe location ($x/\delta = 38.0$, $y/\delta = 0.2$, $z/\delta = 0.0$) and (b) Spanwise PSD analysis of spanwise velocity at a streamwise location ($x/\delta = 62.5$, $y/\delta = 0.3$).

6.3 Effects of injection angle

McClinton (1972) carried out an experimental campaign to determine the effect of injection angle on the jet penetration and mixing rate downstream of isolated or an array of rounded sonic jets. Freestream Mach number was 4.04. Injection angles (away from the line which is normal to the flat plate) such as 0^0, 30^0, 45^0, and 60^0 were studied. This investigation was a part of a research program on the development of technology for the design of supersonic combustion ramjets. Results of this investigation indicated that, at the higher injection angles, less free-stream momentum loss was required to turn and accelerate the injected gas downstream. Besides, the lower injection angles resulted in increased penetration at the downstream stations surveyed and faster mixing of the injected gas with the free stream.

In the present study, we mainly focus on the effects of injection angle in the flow structures in the vicinity and downstream of the sonic jet. Furthermore, we change the injection angle positively or negatively away from the line normal to the flat plate as shown in Figure 6.4. The injection angle, which is aligned with the freestream direction, is denoted by -ϕ, while the injection angle, which is against the freestream direction, is indicated by +ϕ. The constant $PR = 25$ is used to carry out all the simulations.

Therefore, let us study the effect of these two opposite injection angles below.

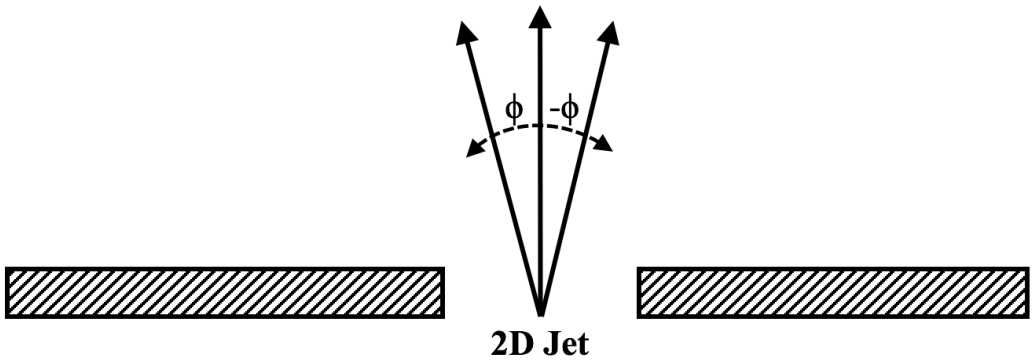

Figure 6.4: Different injection angles of the 2-D sonic jet. Flow is from left to right.

6.3.1 $\phi > 0^0$

In this subsection, we alter the injection angle from $\phi = +15^0$ to $\phi = +30^0$. In Figure 6.5(a), contours of the mean Mach number and streamtraces of the mean vortices are shown on a symmetry plane at $z/\delta = 0$. The topology of upstream and downstream bubbles, that are also observed at $\phi = 0^0$, remain almost unchanged. However, the jet penetration height is slightly lower than at $\phi = 0^0$ case. A reason behind this finding is that the direction of the jet injector is more inclined against the freestream flow in the current ϕ case.

Figure 6.5(b) shows isosurfaces of instantaneous spanwise velocity colored by itself upstream and downstream of the sonic jet. Streamwise streaks are also clearly visible similar to the $\phi = 0^0$ case. We perform the same analysis for $\phi = +30^0$ as shown by Figures 6.6 and find that the penetration height is smaller.

6.3.2 $\phi < 0^0$

Likewise, we alter the injection angle from ϕ = -15^0 to ϕ = -30^0. In Figure 6.7(a), we observe that the secondary upstream bubble appears weaker because of the direction of the jet injector. Since the primary source of the streamwise streaks observed downstream of the jet is the spanwise undulation of the secondary upstream bubbles, we do not observe the same streamwise streaks observed at $\phi = 0^0$, $+15^0$,and $+30^0$. Similar findings are also observed at ϕ = -30^0 as shown in Figures 6.8.

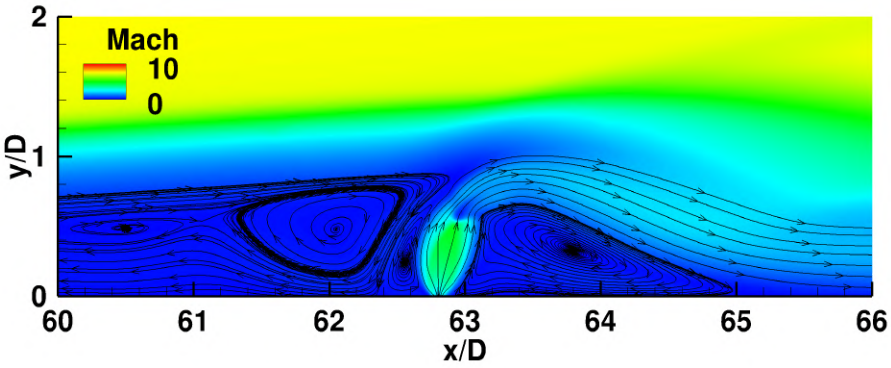

(a)

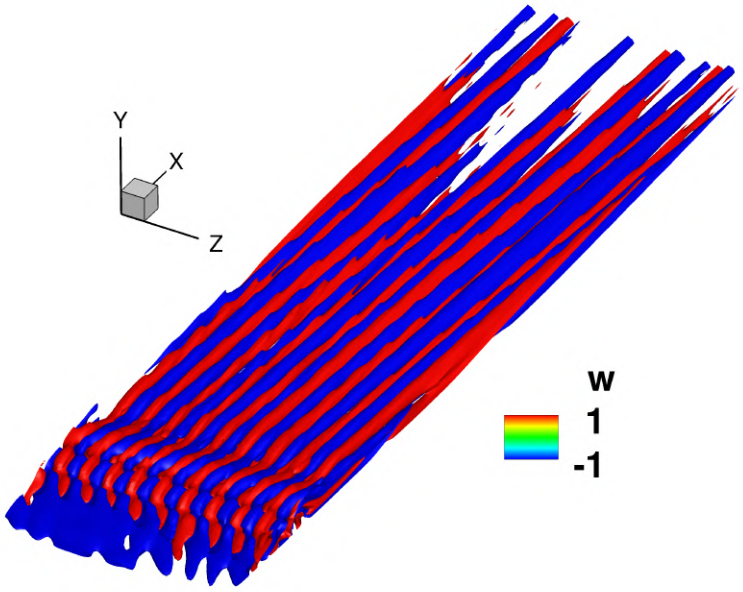

(b)

Figure 6.5: (a) Instantaneous Mach contours on a spanwise plane and (b) instantaneous isosurfaces of spanwise velocity at $PR = 25$ and $\phi = +15^0$.

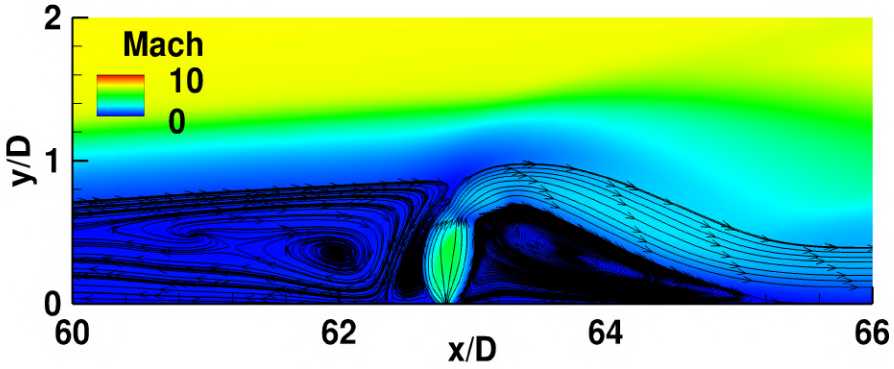

(a)

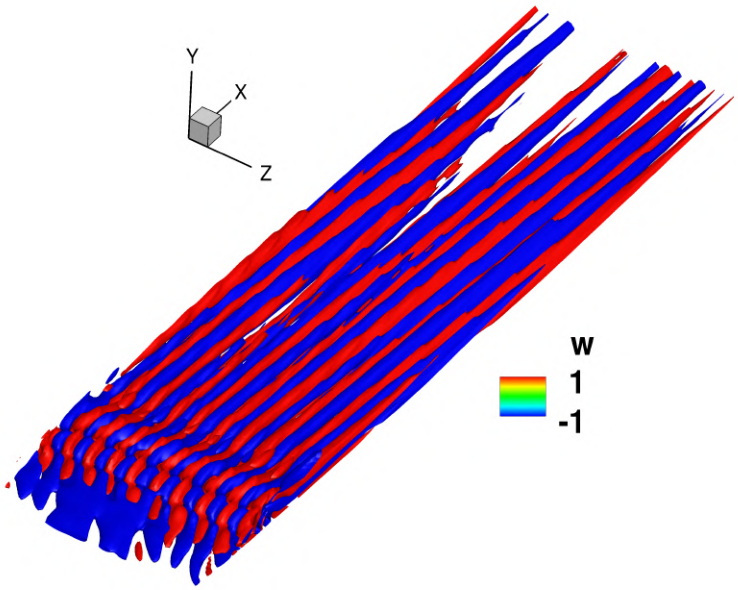

(b)

Figure 6.6: (a) Instantaneous Mach contours on a spanwise plane and (b) instantaneous isosurfaces of spanwise velocity at $PR = 25$ and $\phi = +30^0$.

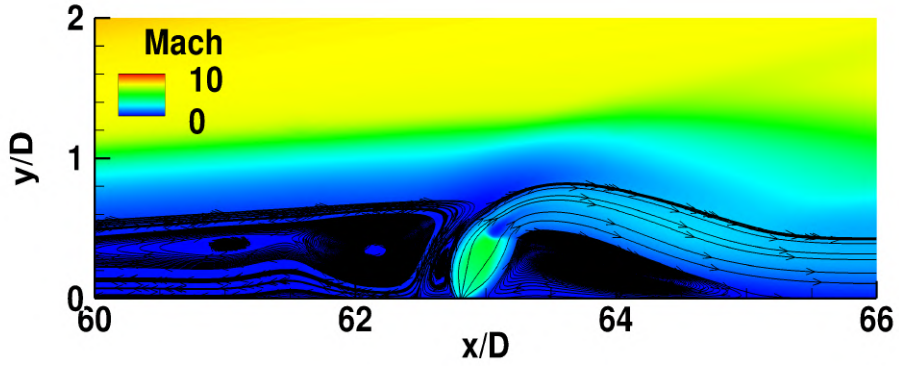

(a)

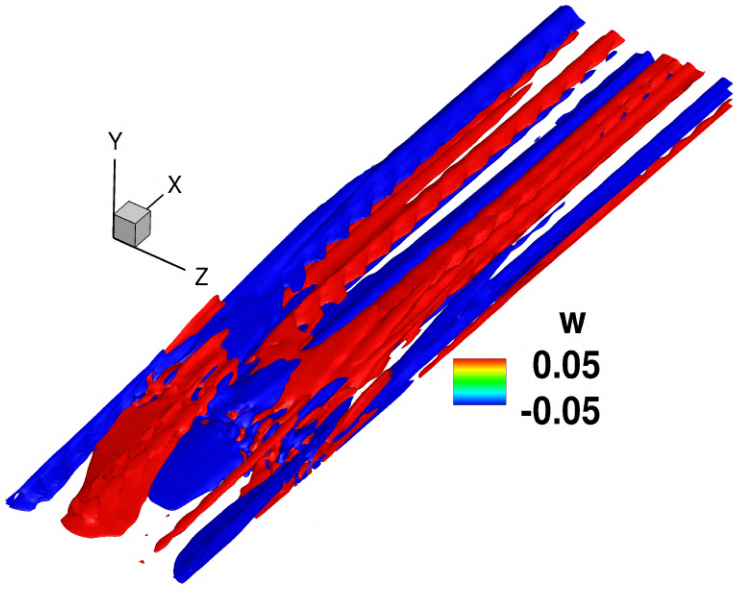

(b)

Figure 6.7: (a) Instantaneous Mach contours on a spanwise plane and (b) instantaneous isosurfaces of spanwise velocity at $PR = 25$ and $\phi = -15^0$.

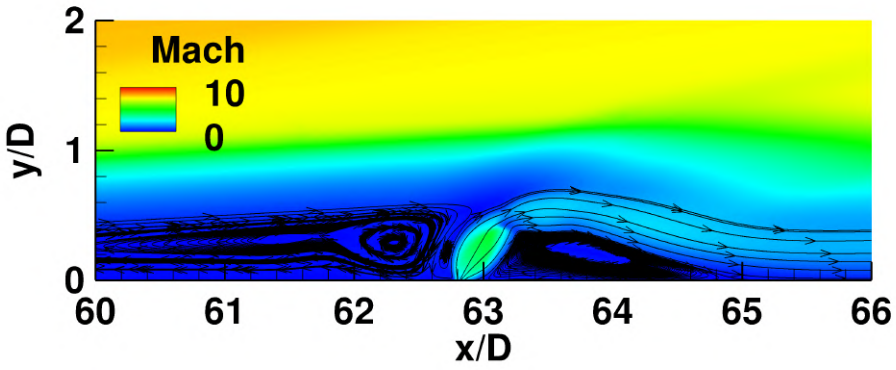

(a)

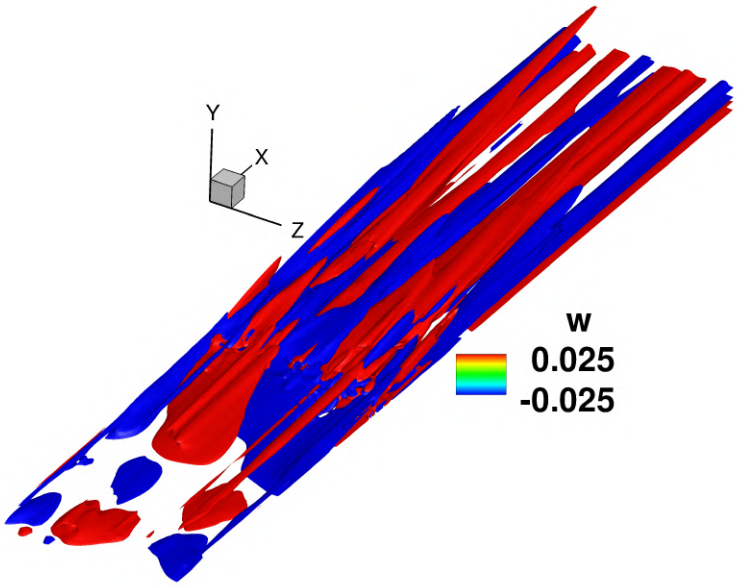

(b)

Figure 6.8: (a) Instantaneous Mach contours on a spanwise plane and (b) instantaneous isosurfaces of spanwise velocity at $PR = 25$ and $\phi = -30^0$.

6.4 Effects of injector pressures on streamwise streaks downstream

In this section, we discuss the effect of injector pressure (PR) on the streamwise streaks downstream of the 2-D sonic jet used in the present study using the isothermal wall. The PR ratios considered in the current study are 10, 15, 20, 25, 30, and 35. At $PR = 10$, 15, 20 and 22.5, we observe that the streamwise streaks observed downstream of the jet are not same (see Figures 6.9-6.10) as at $PR = 25$. However, at a higher $PR = 35$, we observe the similar streamwise streaks as at $PR = 25$ (see Figures 6.11). A possible reason can be that, at $PR = 25$ and higher, stronger undulation of the secondary upstream bubbles occurs, and therefore, more clearly visible streamwise streaks are observed downstream of the jet.

6.4.1 Dominant frequency

Here, we study the effects of wall-injector pressure ratios on dominant frequency in the isothermal case. We carry-out PSD analysis using spanwise velocity at the probe location ($x/\delta = 62.5$, $y/\delta = 0.2$, $z/\delta = 0.0$) at different PR ratios such as 10, 25, 27.5, 30, and 35. We find that a higher PR case leads to a higher peak-amplitude frequency and a higher associated amplitude as shown in Figure 6.12.

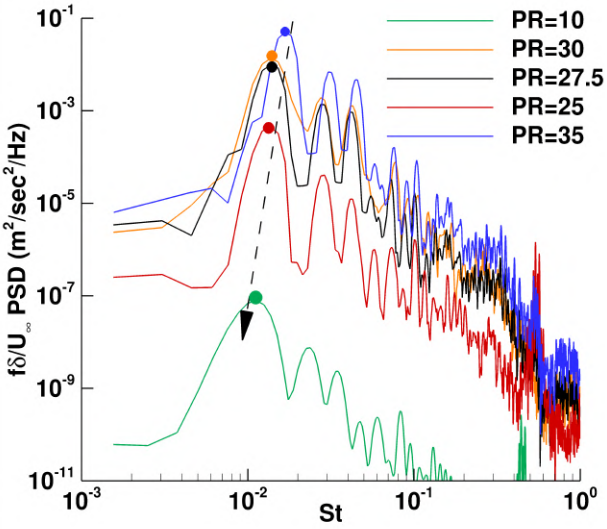

Figure 6.12: Pre-multiplied PSD of spanwise velocity at the probe locaiton ($x/\delta = 62.5$, $y/\delta = 0.2$, $z/\delta = 0.0$) at different PR ratios.

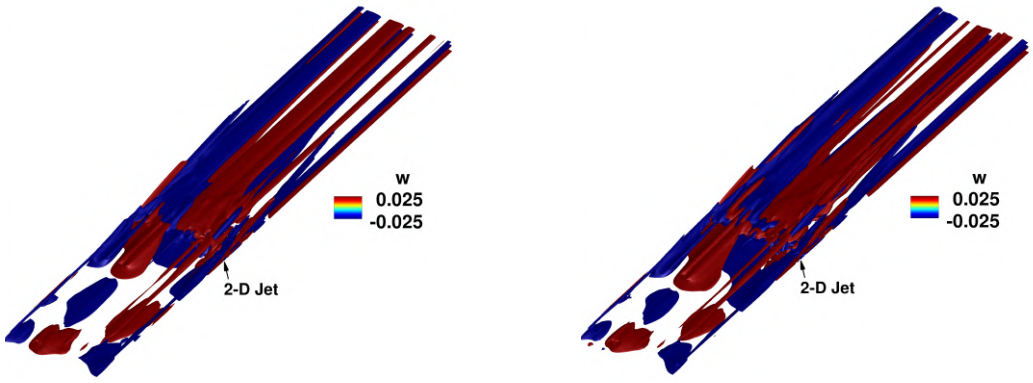

(a) (b)

Figure 6.9: Isosurfaces and contour colors of instantaneous spanwise velocity upstream and downstream of the jet injector at (a) $PR = 10$ and (b) $PR = 15$.

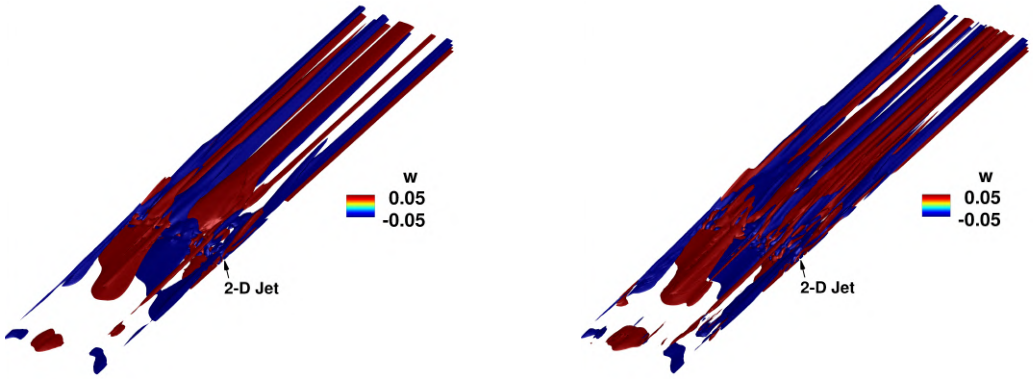

(a) (b)

Figure 6.10: Isosurfaces and contour colors of instantaneous spanwise velocity upstream and downstream of the jet injector at (a) $PR = 20$ and (b) $PR = 22.5$.

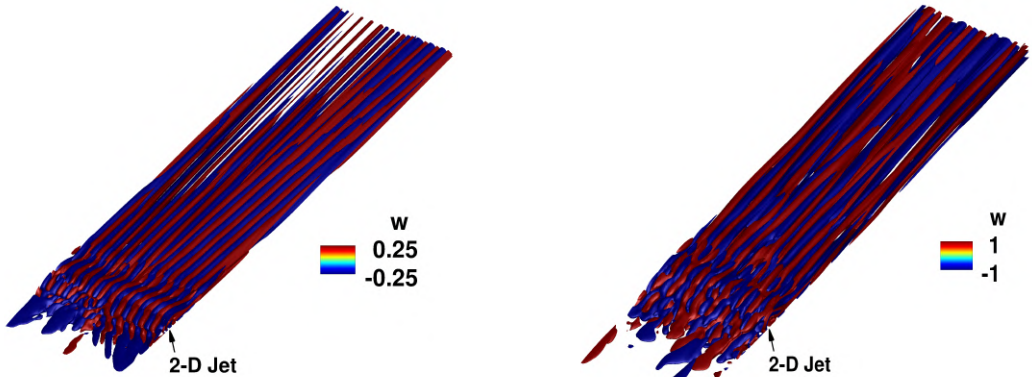

(a) (b)

Figure 6.11: Isosurfaces and contour colors of instantaneous spanwise velocity upstream and downstream of the jet injector at (a) $PR = 25$ and (b) $PR = 35$.

6.4.2 Effects of injector pressure ratios on Mach disk height and separation lengths

In this subsection, we compare an existing model, that predicts the mean Mach disk height with respect to PR ratios, with our simulations in both isothermal and adiabatic wall-boundary conditions. In the present study, the existing model is developed by Werle et al. 1972, who carried out experimental investigations to model the Mach disk heights at different PR ratios using 2D sonic jets. The modeled equation by Werle et al. is shown by 6.2.

$$\frac{h}{\delta} = \frac{A_1 A_2 \gamma_{jet} M_{jet}^2 PRb}{(1 + A_3 A_4 M_\infty)\delta} \tag{6.2}$$

The constants $A_1 = 1.36$, $A_2 = 0.7$, $A_3 = 1.3$ and $A_4 = 0.5$. The specific heat ratio of jet gas (γ_{jet}) = 1.4, wall-injector Mach number (M_{jet}: sonic) = 1.0, slot-width (b) = 2.286×10^{-4}, and $M_\infty = 10.0$

In Figures 6.13(a) and (b), we observe that the model predicts non-dimensionalized Mach-disk height (h/δ) within reasonable agreement at different PR ratios in both isothermal and adiabatic cases. Linear trends of the variation of the Mach-disk height could be due to the flow being weakly non-linear or unsteady. However, these linear trends are observed only up to PR ratio = 30. This finding could be due to the flow becoming more unsteady after the PR ratio = 30. Another interesting finding in both isothermal and adiabatic cases

is the value of the Mach-disk height tends to converge asymptotically to a certain value. Overall, the model predicts the Mack-disk height well up to the certain PR ratio after which the absolute predictability of the model diminishes. A possible reason for this discrepancy could be the experiments were not carried out at higher Mach numbers greater than 8.

In Figures 6.14(a) and(b), we analyze the mean separation length of the recirculation regions upstream and downstream of the sonic jet at different PR ratios in both isothermal and adiabatic cases. Similar to Figures 6.13(a) and (b), we observe linear trends of the variation of the mean separation lengths upstream and downstream for both cases up to the PR ratio = 30. The upstream and downstream separation lengths also tend to converge to a specified value asymptotically in both cases. It is interesting to note that the value of the upstream separation length is not greater than 0 for $PR < 4$ (isothermal) and $PR < 6$ (adiabatic). This finding is observed because no upstream recirculation zone or bubble is observed.

Wang et al. 2017 carried out numerical investigations of a sonic jet penetrating into a high-speed crossflow similar to the present study. They formulated a theoretical model to predict the upstream separation length as shown by 6.3 with respect to PR ratios.

$$X_s = X_c K C \tag{6.3}$$

where, K = a constant value of 4 for T_∞ ranging from 37.56 to 150 K, and X_c = distance between the leading edge of the plate and the jet center = 0.186 m.

$$C = (Re_c)^{-0.1}(b/X_c)^{0.65} PR^{0.77} \tag{6.4}$$

where, Re_c is Reynolds number based on ρ_∞, U_∞, X_c, and μ_∞.

It is observed that the model underpredicts the upstream separation in both isothermal and adiabatic cases as shown by Figure 6.14. A possible reason could be differences in freestream and jet conditions used in the present study and the model.

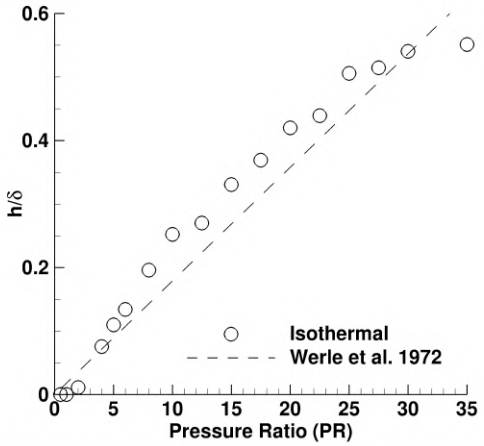

(a)

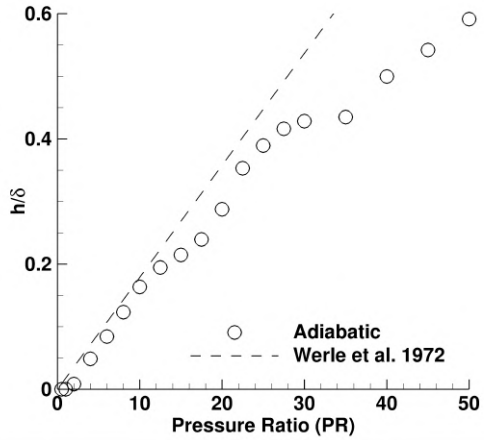

(b)

Figure 6.13: Comparison of the mean Mach disk-height with respect to PR ratios using Werle et al. model with (a) isothermal cases and (b) adiabatic cases. It is important to note that the value of δ is different for the isothermal and the adiabatic cases.

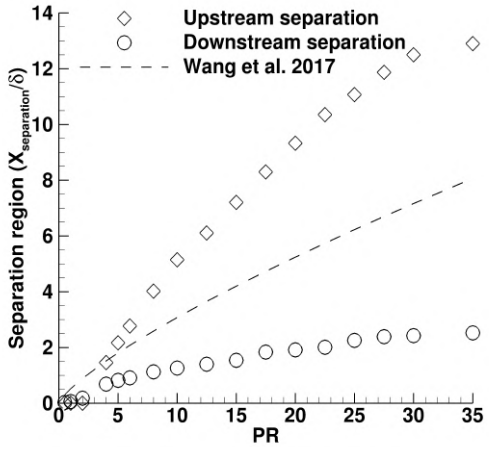

(a)

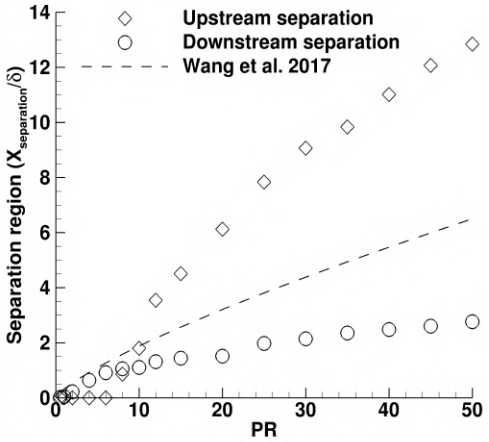

(b)

Figure 6.14: Upstream and downstream separation lengths with respect to PR ratios in (a) isothermal and (b) adiabatic cases. Dashed line: Wang et al. 2017.

Chapter 7

Conclusion

7.1 Passive trips

Direct numerical simulations are used to study laminar-turbulent transition of a hypersonic boundary layer due to an isolated diamond-shaped trip and a spanwise array of diamond-shaped trips. The current study is based on a low Reynolds number hypersonic flow experiment that was carried out at the Texas A & M University. DNS results obtained agree with the experimental data. To investigate the instability mechanisms in both trip configurations, the flow is not perturbed by freestream disturbances or any other forcing apart from the trip. Visualization of the flow shows three prominent regions of unsteadiness consistently observed in both trip configurations: (1) the upstream vortex system, (2) the shear layers/counter-rotating vortex system, and (3) the shock system. Analysis of the PSD and three-dimensional DMD of pressure indicates that the source of instability in both trip configurations is a coupled system of the shear layers from the top edges and corners of the trip, and the counter-rotating streamwise vortices from the wake. The interaction between the wall-normal shear layers (varicose mode) and the counter-rotating vortices leads to the formation of hairpin-like structures that eventually break down to turbulent flow. These findings contradict that of the isolated cylindrical trip where the upstream vortex system is the dominant mode of instability. Therefore, the trip shape plays a significant role in the source of instability, and the trip spacing does not alter the dominant mode of instability. However, the trip spacing changes dominant frequencies of the instability and the instability onset locations. The peak-amplitude frequency associated with instability is

higher in the trip array, while its instability onset location moves further upstream than the isolated diamond-shaped trip. Furthermore, flow breaks down earlier in the trip array. In both trip configurations, the peak-amplitude frequencies, which are observed downstream of the trips, also appear in the upstream vortex system and the shock system as pressure disturbances propagate upstream of the source of instability through the subsonic region.

Parametric studies using a higher freestream Reynolds number flow, intermediate trip-spacings, trip heights, and trip-shape are carried out. The source of instability does not change within a set of freestream Reynolds number investigated, while the peak-amplitude frequency and the mean turbulent kinetic energy increases with the increment of the freestream Reynolds number. The current trip array becomes an array of isolated trips when the center-center trip spacing is more than three times the spanwise trip width. When trip height is reduced, the peak-amplitude frequency decreases, and the instability-onset location is delayed. Variation of the frequency, the instability-onset location, and the upstream recirculation extension is found to be linear with trip heights. Last, the source of instability also does not change between an isolated cylindrical trip (Subbareddy et al. 2014) and an array of cylindrical trips (Williams and Smits 2017). Based on the effectiveness of the methodology used in the present study, DMD, PSD, and DNS have been observed to be useful tools to study the instability mechanism at different parameters for a safer and more efficient vehicle design.

7.2 Active trips

Similar to the passive trips, direct numerical simulations are carried out to investigate transitional hypersonic boundary layers due to a two-dimensional (2-D) sonic jet. The present study is based on an experimental campaign conducted in the 31-Inch Mach-10 wind tunnel at NASA Langley Research Center. DNS data obtained agree well with the experimental data. To understand the instability mechanism due to the sonic jet, flow is not perturbed by any freestream disturbance or any other forcing apart from the jet. Visualization of the flow shows different prominent regions of unsteadiness such as the upstream bubbles, the shock system ahead of the jet, and the downstream bubbles depending upon the injector pressure. Therefore, three successive bifurcations are observed: (1) steady 2-D bubble formation, (2) transition from 2-D steady to 3-D quasi-unsteady bubble, and (3) transition

from 3-D quasi-unsteady to 3-D unsteady bubble. This finding indicates that specific injector pressures are required to control the onset of transition in the laminar boundary layers. Analysis of the PSD shows that unsteadiness observed downstream of the jet is associated with the dominant temporal frequency and the dominant spanwise wavenumber. DMD analysis concludes that the streamwise streaks originate from the upstream bubble system mainly consisting of a primary bubble and a secondary bubble. To obtain more insights on these streaks, a mechanism is proposed. First, the secondary bubble is formed at the second bifurcation point due to high-pressure fluctuations between the primary bubble and the sonic jet. A spanwise undulation at a specific wavelength of the secondary bubble then modulates the primary bubble across span with the same spanwise wavelength. The incoming boundary layer forms two flow structures that have opposite spanwise velocities across these two bubbles. These flow structures then travel to the top of the downstream bubbles to form a streamwise streak. The spanwise wavelength of the dominant DMD mode agrees with that of the streaks observed in the DNS. Real gas effects were also considered, and no significant change in the flow system was observed.

Furthermore, the thermal nature of the wall (either isothermal or adiabatic) does not alter the source of instability, while the peak-amplitude frequency and the dominant spanwise wavenumber change. It is also observed that an angle of the jet injector can play a significant role in the formation of the streamwise streaks. If the direction of the jet is inclined along the freestream direction, the same streamwise streaks are not observed, and vice-versa. The mean Mach-disk height and the mean upstream and downstream separation lengths are compared to existing models in order to access their accuracy under the present flow and jet configurations. The current data of the mean Mach disk height and the model agree well with each other using both isothermal and adiabatic walls, while the data consisting of the mean upstream and the mean downstream separation bubbles do not.

Publications and Presentations

1. SHRESTHA, P. & CANDLER, G. V., Direct Numerical Simulation of Trip Induced Transition, AIAA, Washington D.C., 2016.

2. SHRESTHA, P., HILDEBRAND, N., DWIVEDI, A., NICHOLS, J.W., JOVANOVIĆ, M. & CANDLER, G. V., Interaction of an oblique shock with a transitional Mach 5.92 boundary layer, AIAA, Washington D.C., 2016.

3. SHRESTHA, P. & CANDLER, G.V., Study of transition mechanisms induced by an array of roughness elements, APS DFD, Portland, 2016.

4. DWIVEDI, A., SHRESTHA, P., HILDEBRAND, N., NICHOLS, J.W., JOVANOVIĆ, M. & CANDLER, G., Transition in oblique shock/boundary layer interactions at Mach 5.92, APS DFD, Portland, 2016.

5. HILDEBRAND, N., DWIVEDI, A., SHRESTHA, P., NICHOLS, J.W., JOVANOVIĆ, M. & CANDLER, G., Global stability analysis of oblique shock/boundary layer interactions at Mach 5.92, APS DFD, Portland, 2016.

6. SHRESTHA, P. & CANDLER, G.V., Direct numerical simulation of high-speed transition due to an array of roughness elements, Journal of Fluid Mechanics (under review).

7. SHRESTHA, P., NICHOLS, J.W., JOVANOVIĆ, M. & CANDLER, G.V., Study of Trip-Induced Hypersonic Boundary Layer Transition, AIAA, Denver, 2017.

8. SHRESTHA, P. & CANDLER, G.V., Study of trip-spacing in hypersonic boundary layer transition, AIAA, Florida, 2018.

9. SHRESTHA, P. & CANDLER, G.V., Effects of Freestream Reynolds number and trip-height on high-speed transition, AIAA, Atlanta, June, 2018.

10. SHRESTHA, P. & CANDLER, G.V., Study of high-speed transition due to roughness elements, an invited talk, NIA CFD Seminar, July, 2018.

11. SHRESTHA, P., BERRY, S. A., & CHOUDHARI, M. M., Study of high-speed transition due to a sonic jet, NASA LaRC, August, 2018.

12. SHRESTHA, P., BERRY, S. A., CHOUDHARI, M. M., & CANDLER, G. V., Study of high-speed transition due to a sonic jet, Journal of Fluid Mechanics (in preparation for submission).

13. SHRESTHA, P., BERRY, S. A., CHOUDHARI, M. M., & CANDLER, G. V., Study of high-speed transition due to passive and active trips, seminar talk, Argonne National Laboratory, 2018.

14. SHRESTHA, P., BERRY, S. A., CHOUDHARI, M. M., & CANDLER, G. V., Study of high-speed transition due to passive and active trips, presentation, Los Alamos National Laboratory, 2018.

15. SHRESTHA, P., BERRY, S. A., CHOUDHARI, M. M., & CANDLER, G. V., Study of high-speed transition due to passive and active trips, presentation, GE Global Research Center, 2018.

16. SHRESTHA, P., BERRY, S. A., CHOUDHARI, M. M., & CANDLER, G. V., Study of high-speed transition due to passive and active trips, seminar talk, Oak Ridge National Laboratory, 2019.

References

[1] ACARLAR, M. S. & SMITH, C. R. 1987 A study of hairpin vortices in a laminar boundary layer. Part 1. Hairpin vortices generated by a hemisphere protuberance. *J. Fluid Mech.* **175**, 1-41.

[2] ANDRE, T., DURANT, A., & FEDIOUN, I. 2017 Numerical Study of Supersonic Boundary-Layer Transition due to Sonic Wall Injection. *AIAA Journal.* **50**, No. 5.

[3] BAKER, C. J. 1979 The laminar horseshoe vortex. *J. Fluid Mech.* **95**, 347-367.

[4] BERRY, S. A., AUSLENDER, A. H., DILLEY, A. D. & CALLEJA, J. F. 2001 Hypersonic boundary layer trip development for Hyper-X. *J. Spacecraft and Rockets* **38** (6), 853-864.

[5] BERRY, S. A., NOWAK, R. J., & THOMAS H. J. 2004 Boundary Layer Control for Hypersonic Airbreathing Vehicles.34$^{\text{th}}$, *AIAA Fluid Dynamics Conference and Exhibit*, Portland, Oregon.

[6] BORG, M. P., SCHNEIDER, S. P. & JULIANO, T. J. 2008 Effect of freestream noise on roughness-induced transition for the X-51A forebody. *J. Spacecraft and Rockets* **45** (6), 1106-1116.

[7] BOYD, S. & VANDENBERGHE, L. 2004 Convex optimization. *Cambridge University Press, New York.*

[8] BRANDT, L. 2014 The lift-up effect: The linear mechanism behind transition and turbulence in shear flows. *European Journal of Mechanics B/Fluids* **47**, 80-96.

[9] BRIESCHENK, S., GEHRE, R. M., WHEATNEY, V., BOYCE, R. R., KLEINE, H. & O'BRYNE, S. 2012 Jet interaction in a hypersonic flow: A comparison between PLIF

thermometry and computational simulation. *28th International Congress of the Aeronautical Sciences.*

[10] CANDES, E. J., WAKIN, M. B. & BOYD, S. P. 2008 Enhancing sparsity by reweighted $l1$ minimization, *J. Fourier Analysis Applications* **14**, 877-905.

[11] CANDLER, G. V., JOHNSON, H. B., NOMPELIS, I., SUBBAREDDY, P. K., DRAYNA, T. W., GIDZAK, V. & BARNHARDT, M. D. 2015 Development of the US3D code for advanced compressible and reacting flow simulations, *53^{rd} AIAA Aerospace Sciences Meeting, Kissimmee, Florida.*

[12] CHOUDHARI, M., LI, F., WU, M., CHANG, C., EDWARDS, J., KEGERISE, M. & KING, R. 2010 Laminar-turbulent transition behind discrete roughness elements in a high-speed boundary layer. *48^{th} AIAA Fluid Dynamics Conference, Orlando, Florida.*

[13] CHU, B.-T. 1965 On the energy transfer to small disturbances in fluid flow (part i). *Acta Mechanica.* **1** (3), 215-234.

[14] DANEHY, P. M., BATHEL, B., IVEY, C., INMAN, J. A. & JONES, S. B. 2009 NO PLIF study of hypersonic transition over a discrete hemispherical roughness element. *47^{th} AIAA Aerospace Sciences Meeting, Orlando, Florida.*

[15] DANEHY, P. M., IVEY, C. B., INMAN, J. A., BATHEL, B. F., JONES, S. B., JIANG, N., WEBSTER, M., LEMPERT, W., MILLER, J. & MEYER, T. 2010 High-speed PLIF imaging of hypersonic transition over discrete cylindrical roughness. *48^{th} AIAA Aerospace Sciences Meeting, Orlando, Florida.*

[16] DRAYNA, T. W., HAAG, C. J. W., BARTKOWICZ, M. D., and GIDZAK, V. M., LINK3D, Software Package, Ver 0.9.0, GoHypersonic, Inc., Minneapolis, MN, 2016.

[17] DONOHO, D. L. 2006 Compressed sensing. *IEEE Transactions on Information Theory* **52** (4), 1289-1306.

[18] DUAN, Z., & XIAO, Z. 2017 Hypersonic transition induced by three isolated roughness elements on a flat plate. *Computers & Fluids* **157**, 1-13.

[19] DRAYNA, T. W., HAAG, C. J. W., BARTKOWICZ, M. D., and GIDZAK, V. M., LINK3D, Software Package, Ver 0.9.0, GoHypersonic, Inc., Minneapolis, MN, 2016.

[20] DUCROS, F., FERRAND, V., NICOUD, F., WEBER, C., DARRACQ, D., GACHERIEU, C., & POINSOT, T. 1999 Large-eddy simulation of the shock/turbulence interaction. *J. Computational Physics* **152** (2), 517-549.

[21] ERGIN, F. G. & WHITE, E. B. 2006 Unsteady and transitional flows behind roughness elements, *AIAA J.* **40** (11), 2504-2514.

[22] EVERETT, D. E. & MORRIS, M. J. 1998 Wall Pressure Measurements for a Sonic Jet Injected Transversely into a Supersonic Crossflow. *Journal of Propulsion and Power*. **14**. No. 6.

[23] GENIN, F. & MENON, S. 2010 Dynamics of sonic jet injection into supersonic crossflow. *Journal of Turbulence*, **11**.

[24] GUO LEI, W., LIWEI, C. and XIYUN, L. 2013 Effects of the injector geometry on a sonic jet into a supersonic crossflow. *Science China*, **56**. No. 2: 366377.

[25] HANIFI, A., SCHMID, P. J. & HENNINGSON, D. S. 1996 Transient growth incompressible boundary layer flow. *Phys. Fluids.* **8** (3), 826-837.

[26] HARRIS, F. J. 1978 On the use of windows for harmonic analysis with the discrete Fourier transform. *Proceedings of the IEEE* **66** (1).

[27] HUNT, J. L. & JONES, R. A. 1968 Effects of several ramp-fairing, umbilical, and pad configurations on aerodynamics heating to Apollo command module at Mach 8. *Technical Memorandum NASA-TM-X-1640*. NASA.

[28] HUNT, J. C. R., WRAY, A. A. & MOIN, P. 1988 Eddies, stream, and convergence zones in turbulent flows. *Tech. Rep. CTR-S88, Center for Turbulence Research, Stanford University.*

[29] IYER, P. S. & MAHESH, K. 2013 High-speed boundary-layer transition induced by a discrete roughness element. *J. Fluid Mech.* **729**, 524-562

[30] JOVANOVIĆ, M. R., SCHMID, P. J. & NICHOLS, J. W. 2014 Sparsity-promoting dynamic mode decomposition. *Phys. of Fluids* **26** (2), 024103-024125.

[31] KLEBANOFF, P. S. & TIDSTROM, K. D. 1972 Mechanism by which a two-dimensional roughness element induces boundary layer transition. *Phys. Fluids* **15** (7), 1173-1188.

[32] KLEBANOFF, P. S., CLEVELAND, W. G. & TIDSTROM, K. D. 1992 On the evolution of a turbulent boundary layer induced by a three-dimensional roughness element. *J. Fluid Mech.* **237**, 101-187.

[33] KING, R. A. & BREUER K. S. 2001 Acoustic receptivity and evolution of two-dimensional and oblique disturbances in a Blasius boundary layer. *Journal of Fluid Mechanics.* **432**:6990.

[34] LANDAHL, M. T. 1975 Wave breakdown and turbulence. *SIAM J. Appl. Maths* **28** (4), 735-756.

[35] LAUFER, J. 2012 Aerodynamics noise in supersonic wind tunnels. *J. Aerospace Sciences* **28** (9), 685-692.

[36] LIEPMANN, H. W. 1943 Investigations on laminar boundary-layer stability and transition on curved boundaries. *Wartime Report W-107.* NACA.

[37] LUCA, L. D., CARDONE, G., DOMINIQUE, C., & FONTENEAU, A. 1995 Viscous interaction phenomena in hypersonic wedge flow. *AIAA Journal.* **33**:22932299.

[38] MICOL, J. R. 1998 Langley Aerothermodynamic Facilities Complex: Enhancements and Testing Capabilities. *AIAA Paper* 98-0147.

[39] MILLER, C. G. 1990 Langley Hypersonic Aerodynamic/Aerothermodynamic Testing Capabilities - Present and Future. *AIAA Paper*, 90-1376.

[40] NOMPELIS, I., DRAYNA, T. W. & CANDLER, G. V. 2005 A parallel unstructured implicit solver for reacting flow simulation. *17th AIAA Computational Fluid Dynamics Conference, Ontario, Canada.*

[41] NICHOLS, J. W., LARSSON, J. & BERNARDINI, M. 2017 Stability and modal analysis of shock/boundary layer interactions. *Theor. Comput. Fluid Dyn.* **31**, 33-50.

[42] RADEZTSKY, R. H., REIBERT, M. S., & SARIC, W. S., 1999 Effect of isolated micron-sized roughness on transition in swept-wing flows. *AIAA J.*. **37**:13701377.

[43] REDFORD, J. A., SANDHAM, N. D. & ROBERTS, G. T. 2010 Compressibility effects on boundary-layer transition induced by an isolated roughness element. *AIAA J.* **48** (12), 2818-2830.

[44] RESHOTKO, E. & TUMIN, A. 2004 Role of transient growth in roughness-induced transition. *AIAA Journal.* **42**:766770.

[45] ROWLEY, C. W., MEZIC, I., BAGHERI, S., SCHLATTER, P. & HENNINGSON, D. S. 2009 Spectral analysis of nonlinear flows. *J. Fluid Mech.* **641**, 115-127.

[46] SAYADI, T. & SCHMID, P. J. 2016 Parallel data-driven decomposition algorithm for large-scale datasets: with application to transitional boundary layers. *Theor. Comput. Fluid Dyn.* **30**, 415-428.

[47] SCHMID, P. J. 2010 Dynamic mode decomposition of numerical and experimental data. *J. Fluid Mech.* **656**, 5-28.

[48] SCHNEIDER, S. P. 2008a Effects of roughness on hypersonic boundary-layer transition. *J. Spacecraft and Rockets* **45** (2), 193-209.

[49] SEMPER, M. T. & BOWERSOX, R. D. W. 2017 Tripping of a hypersonic low-Reynolds-number boundary layer. *AIAA J.* **55** (3), 808-817.

[50] SEMPER, M. T., PRUSKI, B. J. & BOWERSOX, R. D. W. 2012 Freestream turbulence measurements in a continuously variable hypersonic wind tunnel. *50^{th} AIAA Aerospace Sciences Meeting, Nashville, Tennessee.*

[51] SHRESTHA, P. & CANDLER, G. V. 2016 Direct numerical simulation of trip induced transition. *45^{th} AIAA Fluid Dynamics Conference, Washington, D. C.*

[52] SHRESTHA, P., NICHOLS, J. W., JOVANOVIĆ, M. R. & CANDLER, G. V. 2016 Dynamic mode decomposition of trip-induced hypersonic boundary layer transition. *46^{th} AIAA Fluid Dynamics Conference, Washington, D. C.*

[53] STONE, D. R. & CARY, A. M. 1972 Discrete Sonic Jets Used as Boundary-Layer Trips at Mach Numbers of 6 and 8.5. *NASA TN D-6802.*

[54] SRINIVASAN, G., DIAB, T. A., MURTHY, M. K., RAVINDRAN, R. & NARASIMHA, R. 1970 Interaction of a Two-Dimensional Sonic Jet With a Supersonic Stream. *Journal of Basic Engineering.* **92**. 901-907.

[55] STEGER, J. L. & WARMING, R. F. 1981 Flux Vector Splitting of the Inviscid Gas-Dynamics Equations with Application to Finite-Difference methods, *Journal of Computational Physics.* **40**. 263-293.

[56] SUBBAREDDY, P. K., BARTKOWICZ, M. D. & CANDLER, G. V. 2014 Direct numerical simulation of high-speed transition due to an isolated roughness element. *J. of Fluid Mech.* **748**, 848-878.

[57] SUBBAREDDY, P. K. & CANDLER, G. V. 2009 A fully discrete, kinetic energy consistent finite-volume scheme for compressible flows. *J. Computational Physics* **228** (5), 1347-1364.

[58] TANI, I. & SATO, H. 1956 Boundary-layer transition by roughness element. *J. Phys. Soc. Japan* **11** (12), 1284-1291.

[59] TOMIOKA, S., JACOBSEN, L. S. & SCHETZ, J. A. 2003 Sonic Injection from Diamond-Shaped Orifices into a Supersonic Crossflow. *Journal of Propulsion and Power.* **19**, No. 1.

[60] TULLIO, N. DE, PARADES, P., SANDHAM, N. D. & THEOFILIS, V. 2013 Laminar-turbulent transition induced by a discrete roughness element in a supersonic boundary layer, *J. Fluid Mech.* **735**, 613-646.

[61] VAN DRIEST, E. R. 1956 On turbulent flow near a wall. *J. Aeronautical Sci.* **23** (11), 1007-1011.

[62] VAN DRIEST, E. R. & BLUMER, C. B. 1962 Boundary-layer transition at supersonic speeds-three-dimensional roughness effects (spheres). *J. Aeronautical Sci.* **29** (8), 909-916.

[63] VAN DRIEST, E.R. & MACAULEY, W.D. 1960 The effect of controlled three-dimensional roughness on boundary-layer transition at supersonic speeds. *Journal of the Aeronautical Sciences.* **27**:261271.

[64] VANLERBERGHE, W. M., CUTTON, J. C., LUCHT, R. P., and SANTIAGO, J. G. 2000 Mixing of a Sonic Transverse Jet Injected into a Supersonic Flow. *AIAA Journal*. **38**:470-479.

[65] WANG, Z., JIANG C., GAO, Z. & LEE, C. 2017 Prediction for the Separation Length of Two-Dimensional Sonic Injection with High-Speed Crossflow. *AIAA Journal*. **55**. No. 3.

[66] WHEATON, B. M. & Schneider, S. P. 2012 Roughness-Induced Instabilities in a Mach-6 Laminar Boundary Layer. *Ph.D. thesis*. Purdue University.

[67] WHITEHEAD, JR., A. H. 1969 Flow-field and drag characteristics of several boundary layer tripping elements in hypersonic flow. *NASA Technical Report, Washington, D.C.*

[68] WLEZIEN, R. W. 1994 Measurement of acoustic receptivity. *AIAA Paper*.

[69] WILLIAMS, OWEN J. H. & SMITS, ALEXANDER J. 2017 Effect of tripping on hypersonic turbulent boundary-layer statistics. *AIAA J.* **55** (9), 3051-3058.

[70] WRIGHT, M. J., CANDLER, G. V. & PRAMPOLINI, M. 1996 Data parallel lower-upper relaxation method for the Navier-Stokes equations. *AIAA J.* **34** (7), 1371-1377.

[71] ZHAO, M., YE, T., CAO, C., ZHOU, T. & ZHU, M. 2016 Study of sonic injection from circular injector into a supersonic cross-flow using large eddy simulation. *International journal of hydrogen energy 4I*, 17657-17669.

Appendix A

Two-dimensional simulations

In this section, we discuss the 2-D simulations, which are carried out ahead of the 3-D simulations to maintain computational efficiency in both diamond-shaped (ACE facility) and cylindrical trips (HyperBLAF facility). The 2-D simulations are separately discussed for each facility.

A.1 Actively Controlled Expansion (ACE) facility

Figure A.1 shows contours of the mean Mach number in the 2-D domain associated with the ACE facility. The construction of the mesh for the 2-D domain is based on the inflow mesh of the 3D domain as shown in Figure A.1. Software used to construct the mesh is Pointwise. The inflow boundary condition (the curved line on the left side of the 2-D domain) is supersonic, and it is shock-aligned in order to capture the leading-edge shock accurately. More information about the boundary conditions is mentioned in Chapter 3. The extraction of 1-D wall-normal profiles of all flow variables is carried at 30 mm from the leading edge of the flat plate. No effect of upstream traveling subsonic disturbances from the outflow boundary (the right-sided boundary in Figure A.1) on the extracted profiles was found. The 1-D extracted profiles are shown in Figures A.2(a) and A.2(b) for all flow variables required as the inflow boundary conditions. Lines indicate the extracted 1-D profiles from the 2-D simulations, while symbols indicate the interpolated inflow profiles across the span of the 3-D simulations.

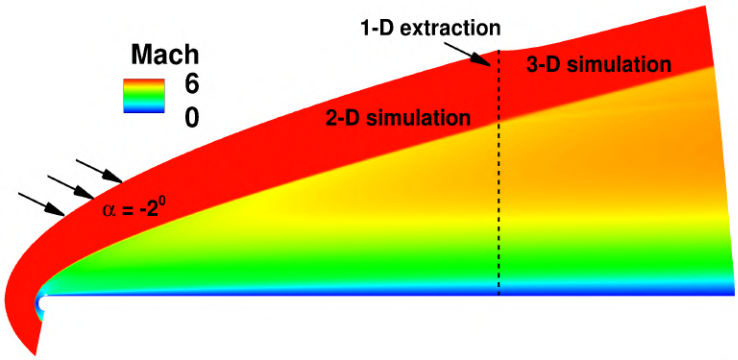

Figure A.1: The mean Mach contours of a 2-D simulation. Dashed line is at $x/D = 9.433$.

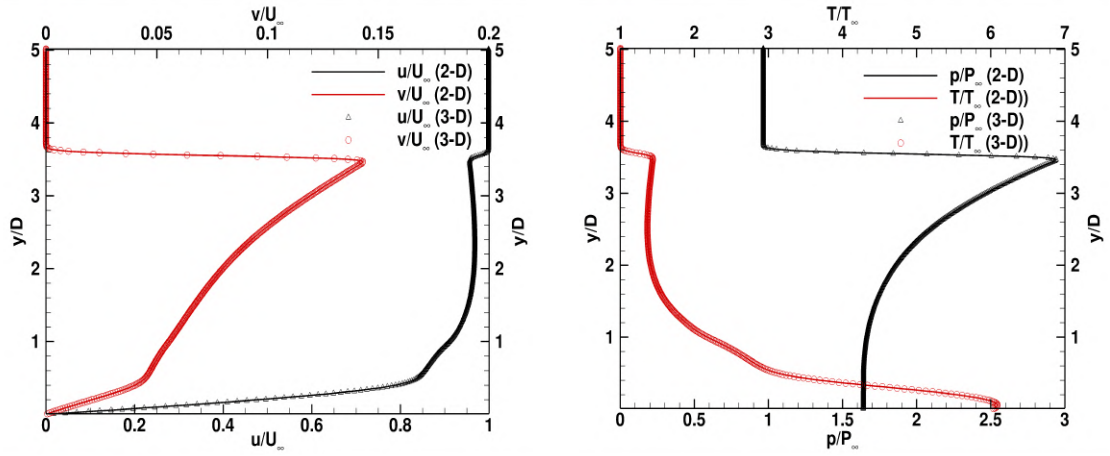

(a) (b)

Figure A.2: 2-D (lines) to 3-D (symbols) interpolations of the mean wall-normal profiles of (a) streamwise velocity and wall-normal velocity, and (b) pressure and temperature at $x/D = 9.433$. ACE Facility.

As the ACE facility is a blowdown wind tunnel, the freestream disturbances are also interpolated from the 2-D domain to the 3-D simulations for validation. Therefore, PSD of pressure at different wall-normal locations at $x/D = 9.433$ in the 2-D domain is shown in Figure A.3.

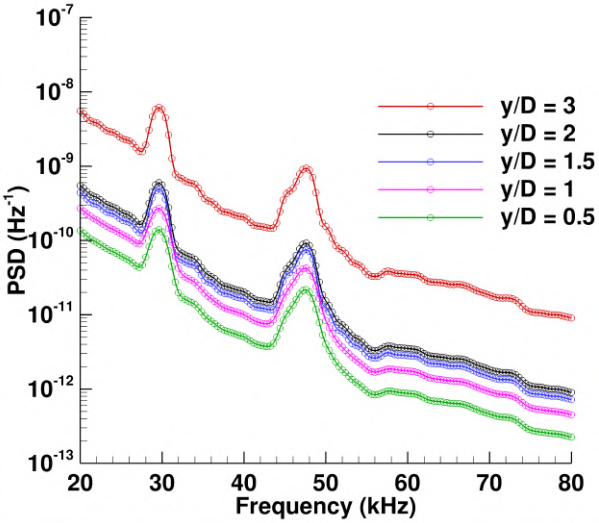

Figure A.3: PSD of pressure at $x/D = 9.433$ at different wall-normal distances of the 2-D domain in which freestream disturbances are applied.

For the higher Re_∞ case studied in the chapter 4, 2-D to 3-D interpolations are shown in Figure A.4.

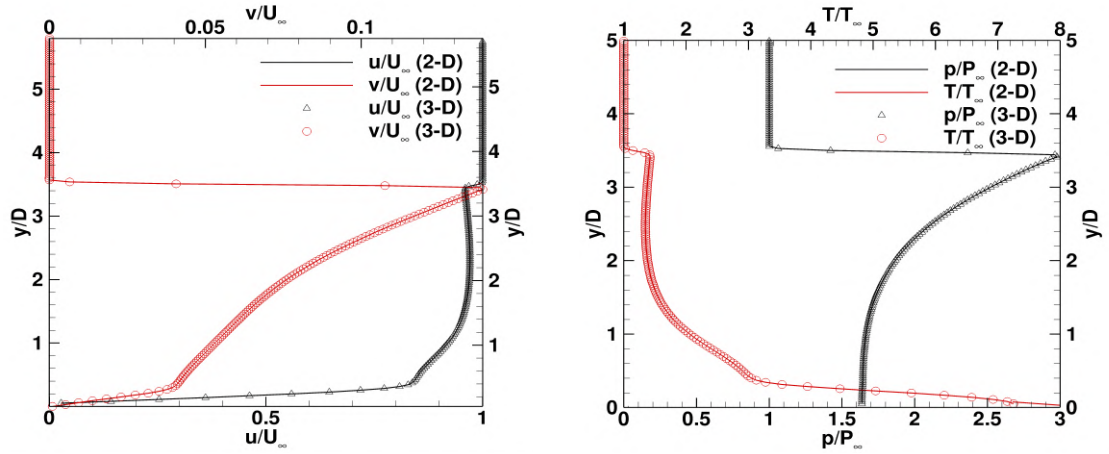

(a) (b)

Figure A.4: 2-D (lines) to 3-D (symbols) interpolations of the mean wall-normal profiles of (a) streamwise velocity and wall-normal velocity, and (b) pressure, and temperature at $x/D = 9.433$ at $3\times Re_\infty$.

A.2 Hypersonic Boundary Layer (HyperBLAF) facility

Now let us discuss details of the extracted 1-D wall-normal profiles used in the 3-D simulations in the HyperBLAF facility. The streamwise location of the 1-D profiles is at 40 mm from the leading edge of the flat plate. No freestream disturbances are imposed. Unlike the ACE facility, there is no angle of attack, and the wall boundary condition is isothermal similar to its 3-D domain, which is mentioned in chapter 4. The extracted profiles are shown in Figures A.5(a) and A.5(b) along with the interpolated inflow profiles across the span of the 3-D domain.

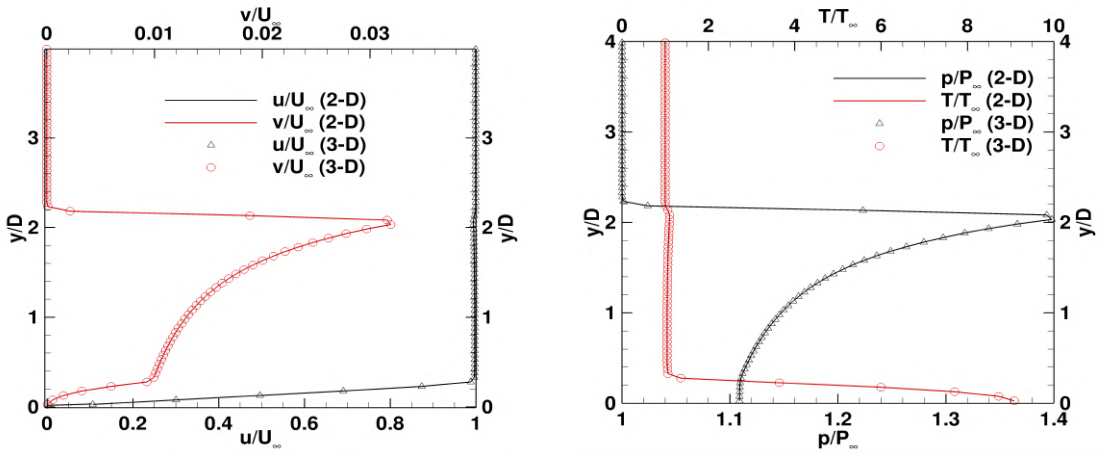

(a) (b)

Figure A.5: The mean wall-normal profiles of streamwise velocity, wall-normal velocity, pressure, and temperature at $x/D = 9.433$. HyperBLAF facility.

Appendix B

Passive trips: dynamic structures near the array of diamond-shaped trips

This chapter discusses dynamic structures in more details upstream and downstream of the trip-array of diamond-shaped trips.

B.1 Upstream vortex system

In the mean, a single-vortex system is prominent upstream of the roughness elements. We observe that the time-averaged upstream extension of the recirculation is large (compared to D) due to the high blockage ratio (50%) in the present study. The mean region (almost constant across the span) extends approximately to 10D upstream of the trips as shown in Figures B.1(a) and B.1(b).

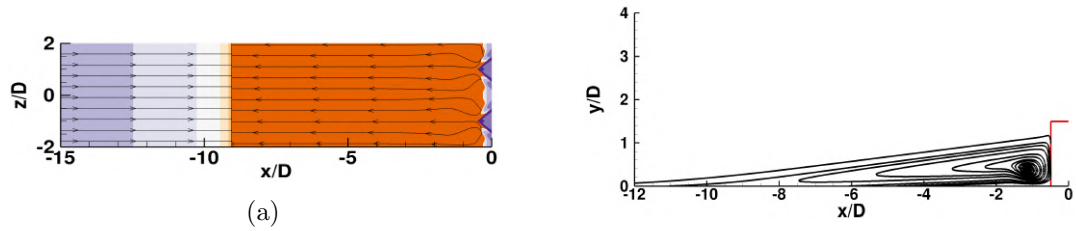

(a) (b)

Figure B.1: (a) Streamtraces of the mean wall-shear stresses colored by the mean streamwise wall-shear (orange: negative and purple: positive) and (b) the mean upstream recirculation region at $z/D = 1$ using the mean velocity streamtraces.

B.2 Shock system

Top upstream portions of the roughness elements, exposed to the post-shock supersonic flow, form a bow shock ahead of the trip. In Figure B.2, contours of the mean turbulent kinetic energy and the R.M.S. values of pressure ahead of the trip are shown on a symmetry plane at $z/D = 1$. In Figure B.2(a), strong prominence of the R.M.S. of pressure indicates strong unsteadiness across the bow shock. We will later discuss the source of this unsteadiness to compare it with the isolated diamond-shaped trip. Similar findings are shown in Figure B.2(b) using the R.M.S. of pressure, where its value is highest across the shock.

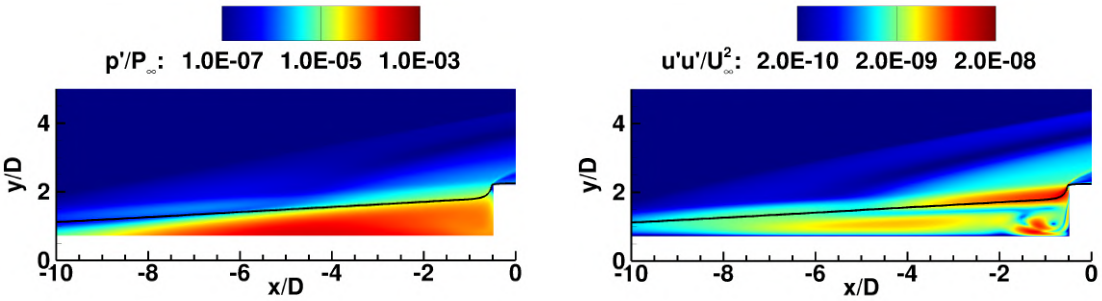

(a) (b)

Figure B.2: (a) The R.M.S. of pressure and (b) the mean turbulent kinetic energy on a symmetry plane at $z/D = 1$. Black lines indicate sonic lines.

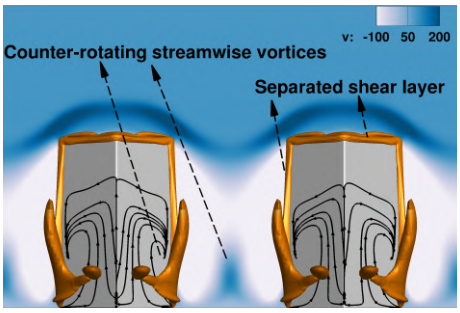

Figure B.3: Back view of instantaneous Q-criterion isosurfaces as well as streamtraces of the mean wall-shear stresses to show the counter-rotating streamwise vortex pair and the shear layers from the top sides and edges of the trip.

B.3 Shear layers and counter-rotating vortex pairs

Now let us discuss the formation of the counter-rotating vortex pair from the wake of a diamond-shaped trip considered in the present study.

In Figure B.3, we observe that the 3-D shear layer appears at the top and side edges of the trips. There exists a strong pressure gradient across the trips as shown in Figure B.4. Moreover, there is a substantial pressure gradient within their wake. These pressure gradients lead to curling up of the shear layer from the sides into a counter-rotating streamwise vortex pair. The flow trajectory near the wall is shown by streamtraces of the mean wall shear stress on the wall and the trip in Figures B.3 and B.4. The process of formation of the counter-rotating vortex pair from the wake is also same in the isolated diamond-shaped trip.

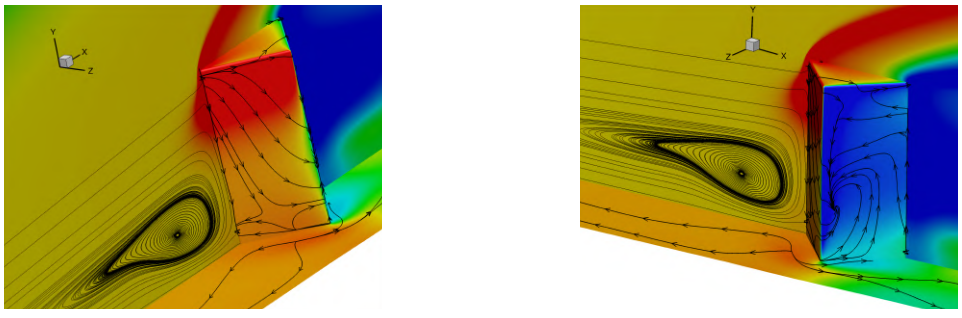

(a) (b)

Figure B.4: (a) Front and (b) back views of the mean pressure contours across the trip. Blue-minimum level and red-maximum level. Streamtraces are the mean wall-shear stress.

Appendix C

Parallel TSQR Algorithm

This chapter discusses an algorithm to perform parallel QR-decomposition of a tall and skinny snapshot matrix for DMD. First, the parallel QR-decomposition algorithm is discussed, and second, the SVD (singular value decomposition)-based data-driven decomposition techniques are presented. This algorithm also discusses to find singular values and vectors. Let us discuss these two steps below based on Sayadi and Schmid (2016).

C.1 Parallel QR-factorization

A schematic of the parallel QR-factorization is shown in Figure C.2.

The data matrix is first divided into submatrices of the same column size and is then distributed among the processors. There are no restrictions on how to assemble and split the data matrix, and a non-uniform breakup of the full data matrix is conceivable. On each processor, a QR factorization is then performed on the respective submatrices and the resulting upper-triangular matrices R_i are gathered into a single matrix, R. This gathering constitutes the only required communication step between all processors in the full algorithm. Each processor then performs an additional QR-factorization on the resulting R matrix, which results in Q_2 and R. The matrix R is the final upper-triangular matrix of the desired QR-factorization of the full data matrix. Each processor then retains its respective portion of Q_2, Q_{2i} with i = 1,..., m, where m is the number of processors. Q_{2i} is a square matrix with the size of the number of snapshots. Multiplying the resulting Q_{2i} by the original Q_{1i}'s of the submatrices yields the final Q of the full data matrix, which is

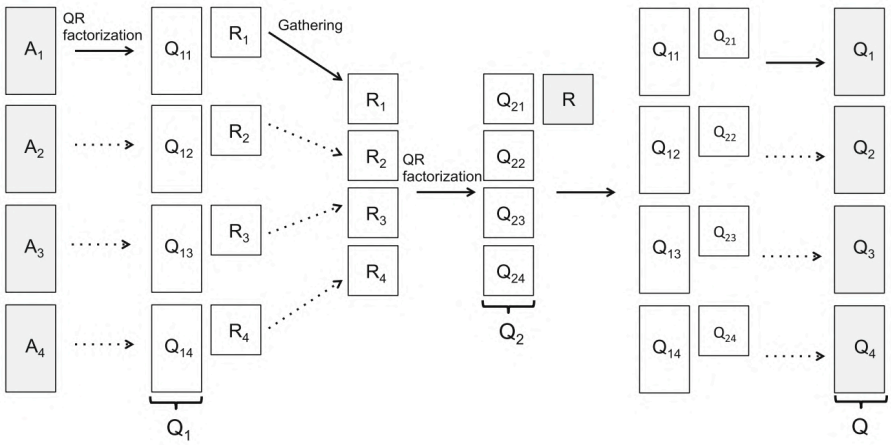

Figure C.1: A schematic of the parallel QR-factorization. Adopted from Sayadi and Schmid 2016.

already distributed among the processors.

C.2 Parallel SVD

Once the QR-factorization is performed, the singular value decomposition of the data matrix can be calculated straightforwardly by applying an additional SVD on the small matrix, R, resulting in $(U_R, \Sigma, W_t) = \text{SVD}(R)$, which is performed by all the processors. The left singular vectors U_i of the full data matrix are then computed by multiplying UR by the respective portion of the orthogonal matrix Q_i, already available on each processor, $U_i = Q_i U_R$.

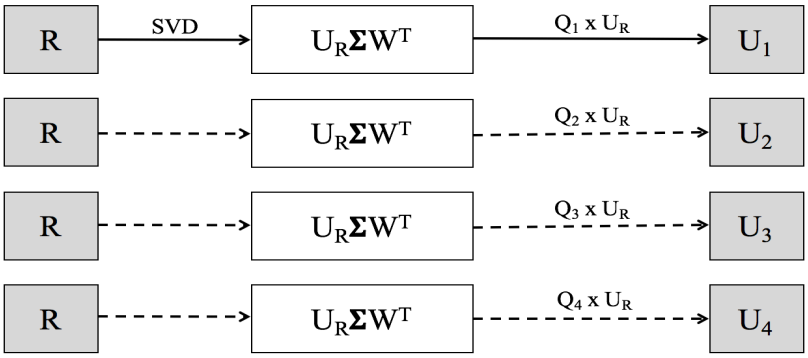

Figure C.2: A schematic of the parallel QR-factorization.

A detailed algorithm of DMD using the TSQR approach is shown in Sayadi and Schmid (2016).

Appendix D

Qualitative validation: Isolated cylindrical trip

In this chapter, we briefly perform qualitative validation of the source of instability using an isolated cylindrical trip ($k/\delta = 1.48$) under the baseline flow configuration (Semper and Bowersox 2017). Mesh generation near this isolated cylindrical trip is shown in Figure D.1(a). We carry-out a freezing operation downstream from the trip center for approximately 10 flow through times. We plot a time-series data of pressure at a probe, that is located at $x/D = 4.3$, $y/D = 2.2$, $z/D = 0.0$, as shown in Figure D.1. We observe that the freezing operation leads to the damping of pressure fluctuations, and therefore, indicates that the source of instability is the upstream vortex system similar to Subbareddy et al. (2014). Therefore, this finding qualitatively validates our simulations with the isolated cylindrical trip (Subbareddy et al. 2014) under similar flow and geometric configurations.

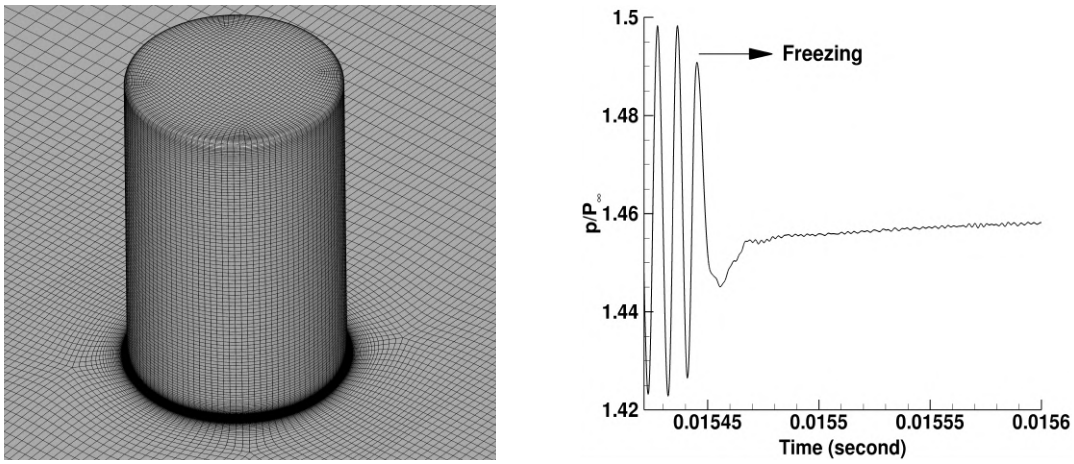

(a) (b)

Figure D.1: (a) Meshes near an isolated cylindrical trip ($k/\delta = 1.48$) and (b) time series data of pressure at ($x/D = 4.3$, $y/D = 2.2$, $z/D = 0.0$). The center of the trip is at ($x/D = 0$, $z/D = 0$)

Appendix E

Preliminary work on a three-dimensional jet-in-supersonic crossflow

It will be interesting to extend the current active trip to a 3-D isolated jet followed by an array of 3-D jets under similar flow configurations. As of now, we have verified a Mach-4.1 DNS simulation using a 3-D isolated circular sonic jet by Andre et al. (2017). For verification, let us first discuss its computational setup, and second, present the verification of our simulation with the author's numerical data, which was obtained using the implicit large eddy simulations (ILES) approach.

E.1 Computational setup

In this subsection, we discuss a computational setup to run DNS simulations using the 3-D isolated jet.

E.1.1 Boundary conditions and Mesh generation

First, we discuss boundary conditions imposed by Andre et al. (2017) in a 3-D domain.

Boundary conditions for the current DNS simulations are shown in Figure E.1. The inflow boundary is supersonic, the wall is adiabatic (isothermal can also be used), and the other boundaries are supersonic outflows.

Table E.1: Freestream conditions: 3-D isolated jet by Andre et al. 2017

SN	Flow	Mach number (M_∞)	Temperature (T_∞)	Pressure (P_∞)
1	Freestream	4.11	97 K	1590 Pa
2	Jet injector	1.00	300 K	12550 Pa (PR = 25)

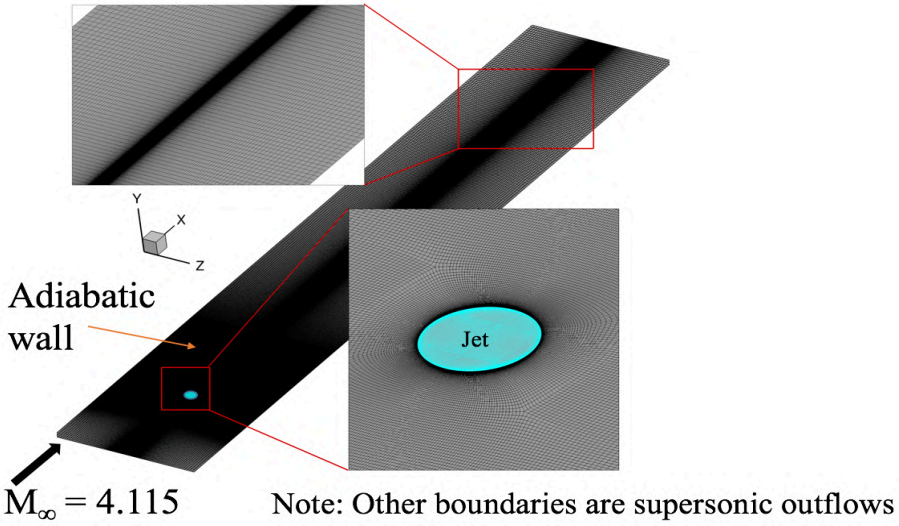

Figure E.1: Boundary conditions of the 3-D isolated jet injector. The diameter of the circular jet (δ_{jet}) is 1 mm.

The total mesh size is 100 million cells. Pointwise is used to generate grids.

E.1.2 Numerical methods

All the spatial and temporal discretization schemes are the same as in the 2-D sonic jet. Time step is 10 nanoseconds. The sampling frequency at 500 kHz and the number of samples of 200 are used to compute the mean flow quantities and DMD modes. Since the maximum data is computed at $PR = 15$ by Andre et al., we will use the same ratio for more comprehensive verification.

E.2 Verification with Andre et al. (2017)

Now let us verify our DNS simulations with Andre et al. In Figure E.2, we observe that the flow structures such as bow shock, Mach-disk, etc. of both simulations agree well with each other in terms of their spatial orientations.

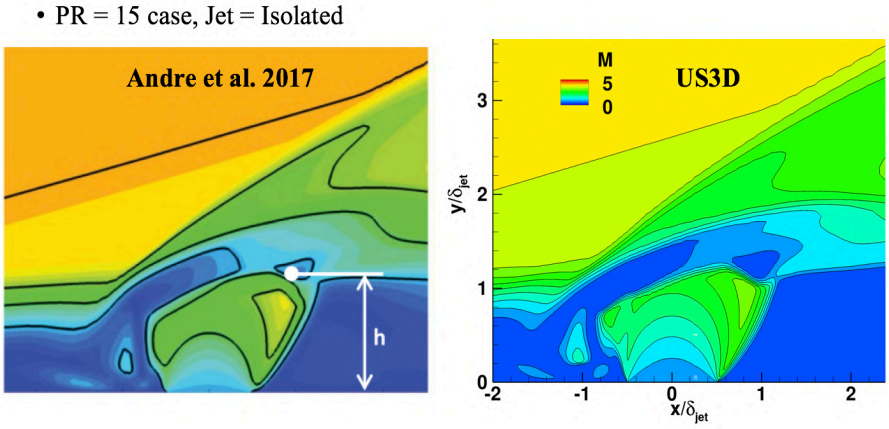

Figure E.2: Verification of the mean Mach contours on a symmetry plane in the vicinity of the 3-D jet.

Figure E.3 shows instantaneous isosurfaces of Q-criterion upstream and downstream of the 3-D jet. We observe horseshoe vortices originating from the region upstream of the jet and the counter-rotating vortex pairs from its wake. Eventually, this unsteadiness downstream causes the flow to breakdown to turbulent flows.

Likewise, we also compare the dominant DMD mode, which is obtained using the Chu disturbance energy norm, between the two simulations. As shown in Figure E.4, we obtain the dominant DMD mode at nearly the same frequency (97 kHz) as by Andre et al. (96 kHz).

We also have other data that further supports this verification. However, to keep the discussion brief, we are confident that our numerical simulations are correctly carried out.

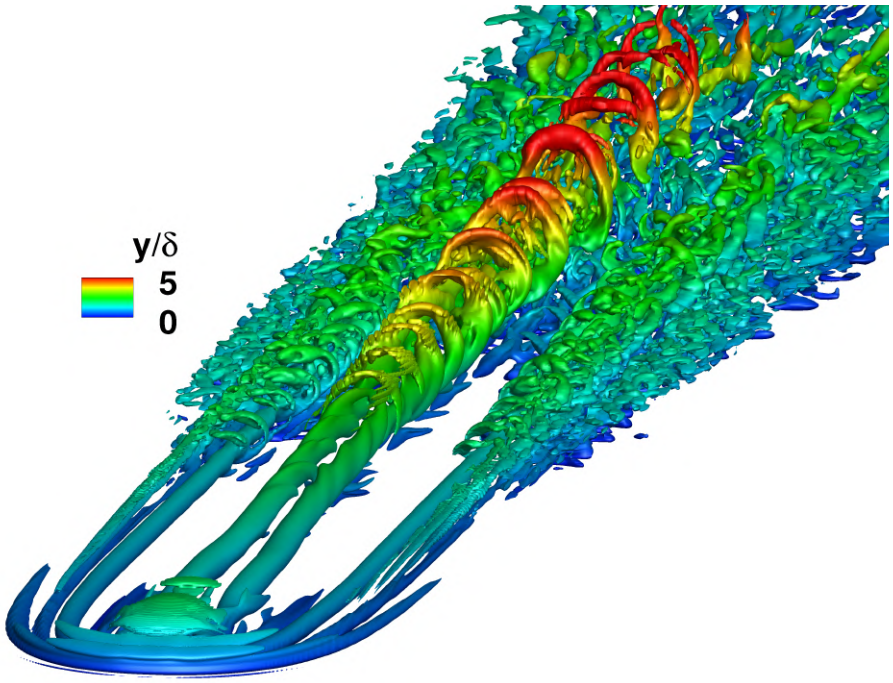

Figure E.3: Isosurfaces of Q-criterion colored by non-dimensionalized wall-normal distance (y/D) in the vicinty of the sonic jet.

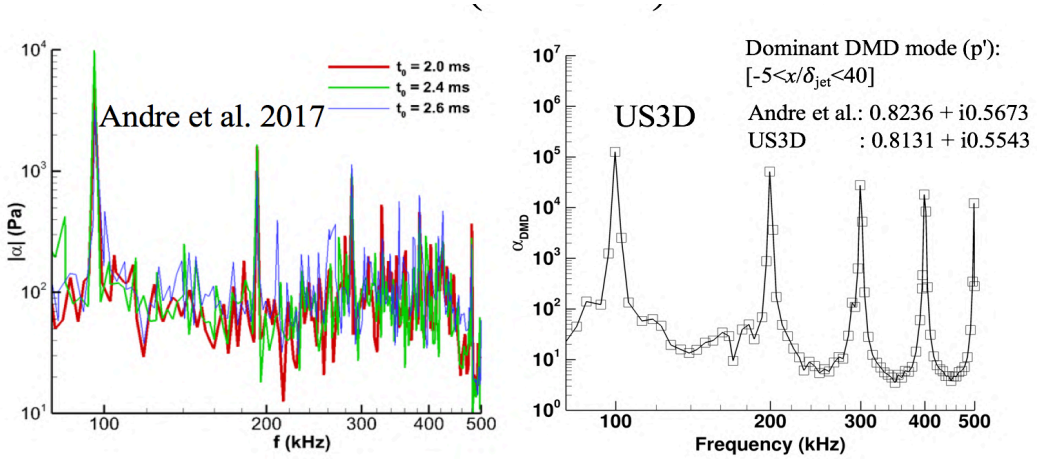

Figure E.4: Verification of the DMD spectrum.

E.3 Future work

If an array of the same 3-D jets is used under the same jet and flow configurations, what different changes in terms of flow unsteadiness will be observed? What will be its optimal jet spacing to cause the earliest transition-onset? It will be interesting to know the answers to these questions in the future.